Mechanistic Investigation of the Effect of S-based Poisons on Pd-Catalyzed Cross-Coupling Reactions

by

Nadini Thushara Pitipana Achchige

Bachelor of Science (Chemistry special), University of Sri Jayewardenepura, 2018

Master of Philosophy in Chemistry, University of Sri Jayewardenepura, 2022

A thesis submitted in partial fulfillment of the
requirements for the degree of

MASTER OF SCIENCE

in the Department of Chemistry

Mechanistic Investigation of the Effect of S-based Poisons on Pd-Catalyzed Cross-Coupling Reactions

by

Nadini Thushara Pitipana Achchige

Bachelor of Science (Chemistry special), University of Sri Jayewardenepura, 2018

Master of Philosophy in Chemistry, University of Sri Jayewardenepura, 2022

Supervisory Committee

Dr. J. Scott McIndoe, Supervisor
Department of Chemistry

Dr. Jon Husson, Supervisory Committee Member
Department of Earth and Ocean Sciences

Abstract

Catalyst poisons are unwanted components in a reaction mixture that lead to the partial or total deactivation of a catalyst. Most previous work on homogeneous catalyst poisoning has focused on identifying the poisons in a catalytic cycle and their effects on catalyst performance, therefore, chemists can take measures to avoid or exclude these types of poison from the system. The chemical behavior of catalyst poisons and how the poisons bind to the catalyst are under-explored areas. Hence, an improved understanding of homogeneous catalyst poisoning is crucial because it can be applied to the systems where the reaction needs to be terminated at a certain point in a catalytic cycle, by deliberately introducing the poison into the reaction mixture. Furthermore, such studies will give molecular insight into the poisoning in homogeneous catalysts, providing the necessary understanding of the catalyst poisoning behavior.

In this work, pressurized sample infusion - electrospray ionization - mass spectrometry (PSI-ESI-MS) was used to introduce a poison into a reaction flask containing a Pd cross-coupling reaction solution, which was monitored in real-time. The combination of mass-to-charge ratio (*m/z*), isotope pattern, and fragmentation behavior was used to characterize the newly formed Pd-poisoned species. Tetrakistriphenylphosphine palladium(0) was used as the catalyst, and three S-based poisons: 1,2-benzenedithiol, thiourea, and *N*-acetylcysteine were used in this analysis. Poisoning experiments were conducted on the precatalyst Pd(0) solution and on the complexes generated after oxidative addition of an aryl halide to make Pd(II) complexes. All three of the poisons reacted rapidly with Pd(0), all via oxidation of the Pd to Pd(II) and deprotonation of the poisons, revealing significant changes in the Pd complexes. Newly formed Pd-poisoned species were identified using tandem mass spectrometry (MS/MS).

Mass spectrometry quantification of these poisoned species was a significant challenge during these studies, since MS quantification is complex due to the frequent occurrence of non-linear responses with increasing analyte concentrations. Therefore, a key part of these investigations was ensuring the instrument used was always well-calibrated.

Developing calibration curves for quantification is a time-intensive task. A novel project designed to make calibration faster and easier: A one-experiment approach to calibration, details real-time continuous calibration method was the subject of Chapter 3. The same PSI-ESI-MS technique was used in this collaboration project to construct a highly accurate and precise continuous calibration curve for achieving high-quality analytical results in both mass spectrometry and UV-Vis spectroscopy. The results were sufficiently encouraging that this method has wide scope for any analytical method that allows continuous monitoring of a solution.

Overall, this work provides the molecular insight into the field of catalyst poisoning, as well as providing a novel continuous calibration method for future use in analytical chemistry.

Table of Contents

List of Schemes

List of Figures

List of Abbreviations

APCI	Atmospheric Pressure Chemical Ionization
ATR	Attenuated total reflectance
CI	Chemical Ionization
CID	Collision induced dissociation
CE	Collision energy
DC	Direct-current
FDI	Field Desorption Ionization
ESI	Electrospray Ionization
GC	Gas Chromatography
HPLC	High-performance liquid chromatography
IR	Infrared
MALDI	Matrix-Assisted Laser Desorption Ionization
MeCN	Acetonitrile
MS	Mass spectrometry
PPN	Bis(triphenylphosphine)iminium
Ph	Phenyl
PEEK	Polyetheretherketone
PSI	Pressurized sample infusion
RF	Radio frequency
MS/MS	Tandem mass spectrometry scans
NMR	Nuclear Magnetic Resonance
THF	Tetrahydrofuran
TLC	Thin layer chromatograph

TOF	Time of flight
TPPMS	Triphenylphosphinomonosulfonate
TQD	Triple quadrupole
UV-Vis	UV-Visible

Acknowledgements

First and foremost, I would like to convey my deepest gratitude and respect for my research supervisor, Prof. Scott McIndoe, Department of Chemistry, University of Victoria, for his invaluable guidance and precious encouragement throughout the research, for his patience, motivation, enthusiasm, and immense knowledge. Without his guidance and constant feedback this MSc would not have been achievable.

I am indebted to the University of Victoria, BC, Canada, the University Research Grant for its financial support. My sincere thank goes Prof. Alexandre Brolo (Chair of the Department of Chemistry, University of Victoria) for the support given in many ways throughout these years.

I would like to thank my committee for their assistance in completing this program and for giving me guidance and helping me learn throughout the years.

I would like to thank my colleagues Ian Chagunda, Charlie Killeen, Jack Smart and Dr. Peter Williams for their support throughout these years. They worked exceptionally hard for me, and it was a pleasure to work alongside them.

I am forever indebted to my family members for giving me the opportunities and experiences that have made me who I am. Last but not the least, I owe thanks to my husband who went through hard times together, cheered me on, and celebrated each accomplishment and for his unfailing love, support, understanding and for all the sacrifices that made on my behalf.

DEDICATION

To the amazing MEN in my life

- Mr. Ramyapala Pitipana Achchige

For being the best father in the world, and for being my hero who has shown me that strength isn't all about muscles. His blessings from heaven continue to guide and inspire me every day.

- Priyantha Kumara

For being the best husband in the world, for continuously supporting me throughout these years, and for his unwavering love and care.

- Mikael Nehas

For filling my life with boundless love and happiness, for letting me experience the joy of motherhood, and for his endless warmth and affection that light up my life.

- Prabhath Meegamage

For being my best friend with whom I can share every bit of my life without being judged, for standing by me through all of life's ups and downs, and for being a pillar of strength in my life.

- Ramesh Viduranga

For being the best brother in the world, and for holding my hand through thick and thin.

- Mr. David Singho

For being the best grandpa in the world, and for his continuous encouragement throughout my life.

Chapter 1

Literature Review

1.1 Reaction Monitoring Methods

In the field of chemistry, reaction monitoring is important to optimize reaction conditions and to elucidate mechanisms. Therefore, understanding the progress and dynamics of a chemical reaction is crucial in this context. Consequently, several methods have been developed to monitor reactions, each with its own benefits and drawbacks. Among these, spectroscopic and chromatographic techniques are widely used due to their versatility and reliability.

Ultraviolet-Visible (UV-Vis) spectroscopy is a straightforward technique used to monitor reactions.[1] This technique is based on the interaction between light and matter, especially for those involving conjugated systems or chromophores.[2] It works by measuring the absorption of UV or visible light by the reaction mixture (**Figure 1.1**). First, the instrument uses a light source that emits light across the UV and visible spectrum (typically 200-800 nm), then the light passes through a monochromator, which disperses the light into its component wavelengths, and allows a specific wavelength to be selected. Subsequently, the selected wavelength of light then passes through the sample which is usually in a cuvette (a small, transparent container). In the next step, the light reaches a detector, and the detector measures the intensity of the light that passes through the sample. Afterwards, the instrument compares the intensity of the light before and after it passes through the sample and the resulting intensity difference is used to calculate the absorbance (A) of the sample at that specific

wavelength. Finally, absorbance at each wavelength is recorded by scanning across a range of wavelengths to generate a spectrum. This spectrum is a plot of absorbance versus wavelength.

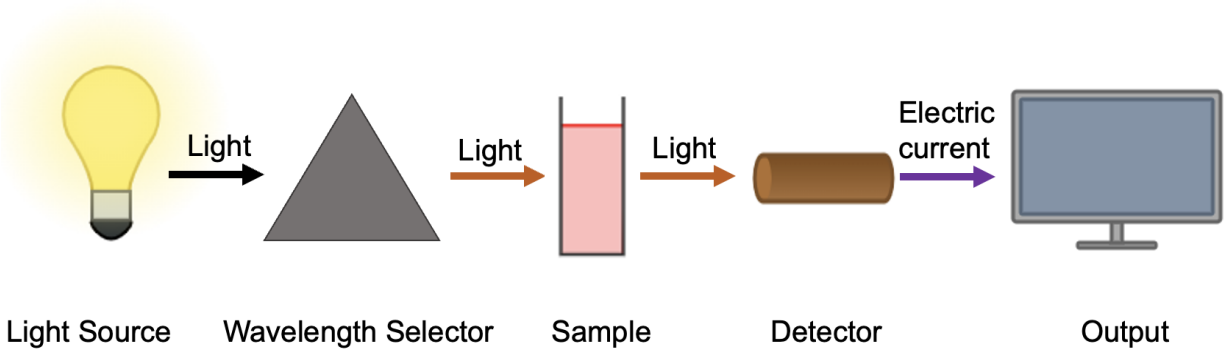

Figure 1.1. A simplified diagram showing the components in a UV-Vis spectrophotometer.

Even though, it is useful in reaction monitoring, UV-Vis has several limitations: (1) in complex mixtures, the absorption bands of different components may overlap, making it difficult to distinguish between them and accurately quantify each species; (2) identifying a new species solely based on its UV/Vis spectrum is not usually possible, so other methods must be deployed.

Nuclear Magnetic Resonance (NMR) spectroscopy is one of the most widely used methods for reaction monitoring. NMR techniques (^{1}H, ^{13}C, ^{19}F and others) provide detailed information about the molecular structure, dynamics, and electronic environment of the species in the reaction mixture. Products can be analyzed by the chemical shifts, coupling constants, and relaxation times of the corresponding NMR spectra. Both offline and online monitoring setups can make use of NMR spectroscopy.[3] Despite these advantages, NMR spectroscopy has some limitations. For

example, because of the overlapping signals, NMR spectra can be very complicated in complex mixtures. In NMR, it generally requires relatively high concentrations of the sample to obtain a good signal-to-noise ratio. Detecting a low-concentration species can be challenging even with significant (and time-consuming) signal averaging.

Infrared (IR) spectroscopy is also used for monitoring reactions that involve changes in functional groups.[4] Infrared spectroscopy provides information about the vibrational modes of the molecules. Changes in vibrational frequencies allows the identification of functional groups and tracking of their transformations during the reaction. Fourier-transform infrared (FTIR) spectroscopy is commonly used for this purpose because of its high sensitivity and resolution.[5] Besides its benefits, IR spectroscopy has several drawbacks such as less effectiveness for quantitative analysis, overlapping of IR absorption bands corresponding to different components and it leads to complicating the interpretation of spectra. A popular approach in reaction monitoring is Attenuated Total Reflectance (ATR) IR spectroscopy, in which the analysis is conducted at the diamond tip of a fiber optic probe. This method has the great advantage of being able to be conducted in-situ in the reaction flask itself, thus reflecting the real reaction conditions accurately.[6]

Chromatographic techniques, such as Thin Layer Chromatography (TLC) is a rapid and cost-effective method for reaction monitoring.[7] It is a primary qualitative method which indicates the presence or absence of the compounds. It is not reliable for precise quantification without additional calibration and densitometry techniques.[8] The reaction progress can be quickly accessed by comparing the Rf values of the reactants and products by spotting small aliquots of the reaction mixture onto a TLC plate and developing it in an appropriate solvent system. TLC is a valuable tool for preliminary

assessments and optimization, but it is less precise than HPLC or GC.

Other chromatographic techniques, such as High-Performance Liquid Chromatography (HPLC) and Gas Chromatography (GC), are important techniques in separating and quantifying the components of a reaction mixture. HPLC is particularly useful for monitoring reactions in a solution. It allows for the separation of compounds based on their polarity, and interaction with the stationary phase. Drawbacks of these chromatographic techniques in reaction monitoring are; labor-intensive, and time consuming, though recent developments in automation are making these approaches more accessible.[9]

Furthermore, methods like Raman spectroscopy,[10] fluorescence spectroscopy,[11] and electrochemical techniques[12] have unique advantages for specific types of reactions. Fluorescence spectroscopy is highly sensitive and useful for reactions involving fluorescent species or probes. Electrochemical methods can monitor redox reactions by measuring current or potential changes.

Other advanced methods such as mass spectrometry (MS) provide real-time analysis of the reaction mixture by ionizing molecules and separating ions according to their mass-to-charge ratios. MS is particularly powerful when coupled with chromatographic techniques (e.g., LC-MS or GC-MS), enabling both separation and identification of the reaction components.

1.2 Reaction Monitoring Using Mass Spectrometry

Mass spectrometry (MS) is a powerful analytical technique in chemistry, biochemistry, pharmacy, medicine, and many other fields due to its low detection limit, high

sensitivity, high accuracy as well as demanding a minimal analyte amount/quantity.[13] The first device for separating ions based on their mass-to-charge ratio was built by Joseph John Thomson.[13] This invention led to the creation of the basis of MS. A mass spectrometer includes an ion source, a mass analyzer, and a detector (**Figure 1.2**). Operating mechanism of the mass spectrometer is that it first converts the introduced analyte into gas phase ions using various ionization techniques, and then separates the ions according to their mass-to-charge ratio (*m/z*) by applying a magnetic or/and electric field, finally fragments/ions are detected at the detector. A spectrum of ion intensity versus *m/z* ratio, and the chromatogram can then be obtained from these detections. Each peak indicates the presence of an ion at that particular *m/z*.

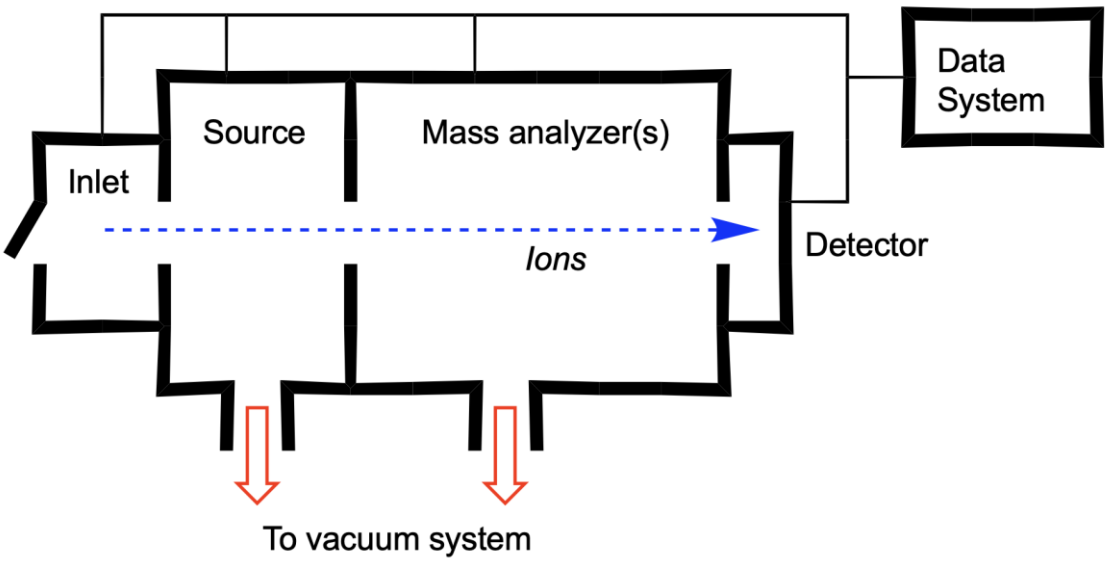

Figure 1.2. Illustration of the components in a mass spectrometer. Adapted with permission from Mass Spectrometry of Inorganic and Organometallic Compounds: Tools - Techniques - Tips, J. Scott McIndoe, William Henderson, ISBN: 978-0-470-85016-9, 2005.

The analyte/sample of interest must be charged for it to be manipulated and detected. Charged ions are produced in the ionization chamber using different methods based on the operation technique. The oldest and most common ionization technique is the electron ionization (EI) formerly known as electron impact ionization, developed by Dempster in 1918.[14] In this approach, the ion source is a beam of energetic electrons (~70 eV). The gas phase analyte molecules are brought into the electron beams in this ionization process which leads to the production of molecular ion $[M]^{\cdot+}$. Since this ionization process imparts a lot of energy, the resulting mass spectrum contains mainly fragments of the parent ion. Therefore, this is generally known as a "hard ionization" (high fragmentation) method.

Over the time, "soft ionization" methods such as Chemical Ionization (CI),[15] Field Desorption Ionization (FDI)[16] and Atmospheric Pressure Chemical Ionization (APCI)[17] were developed to preserve the molecular ion, since hard ionization methods give very complicated spectra when applied to mixtures and sometimes the molecular ion is not detected at all. In CI, reagent gas molecules such as methane are first ionized by an electron beam to produce reagent ions such as CH_5^+, which are extremely acidic and hence protonate adjacent analyte molecules in gas phase. In this process, less fragments are produced compared to EI, since the energy transfer is not directly between the high energy electron beam and the analyte molecules. This method is limited by sample volatility and hence is restricted to detecting small molecules.

Among the other ionization techniques, Electrospray Ionization (ESI)[18] and Matrix-Assisted Laser Desorption Ionization (MALDI)[19] are worth emphasizing due to their importance and uses. In MALDI, the analyte is blended with a suitable matrix material and deposited onto a metal plate. The sample is energized with a pulsed UV-laser resulting in ablation and desorption of both sample and matrix. Finally, the analyte molecules become ionized through protonation or deprotonation. MALDI finds wide range of applications including detection of protein complexes,[20] detection and identification of parasites,[21] determination of molar mass distribution of polymers[22] and even in organometallic catalysis reaction research.[23]

For use in this thesis, electrospray ionization was used as a soft ionization method in order to evaluate the mechanism of solution phase reactions, as its characteristics of softness and application to the solution phase makes it ideal for probing homogeneous reactions in real time.

1.3 Electrospray Ionization (ESI)

Electrospray ionization (ESI) was first developed by Malcolm Dole[24] in 1968 and improved by John Fenn in the 1980s.[25] Dr. Fenn received a share of the Nobel Prize in Chemistry in 2002 for his contributions to electrospray ionization mass spectrometry.

Electrospray ionization (ESI) utilizes a high electrical potential to facilitate the transfer of ions from a solution into the gas phase before being introduced to the mass analyzer.[26] Analyte is introduced as a solution in a polar solvent through a charged capillary which has a high voltage (between 2 to 5 kV). This results in the formation of a Taylor cone at the end of the capillary tip due to the high electric field, and the tip of

the cone is unstable and breaks apart into a cloud of fine droplets (**Figure 1.3**). The charged droplets are desolvated by a nebulizing stream of warm nitrogen gas, causing them to shrink. The increase in charge density causes ions on the surface of the droplet to be ejected into the gas phase and drawn in towards the mass analyzer.

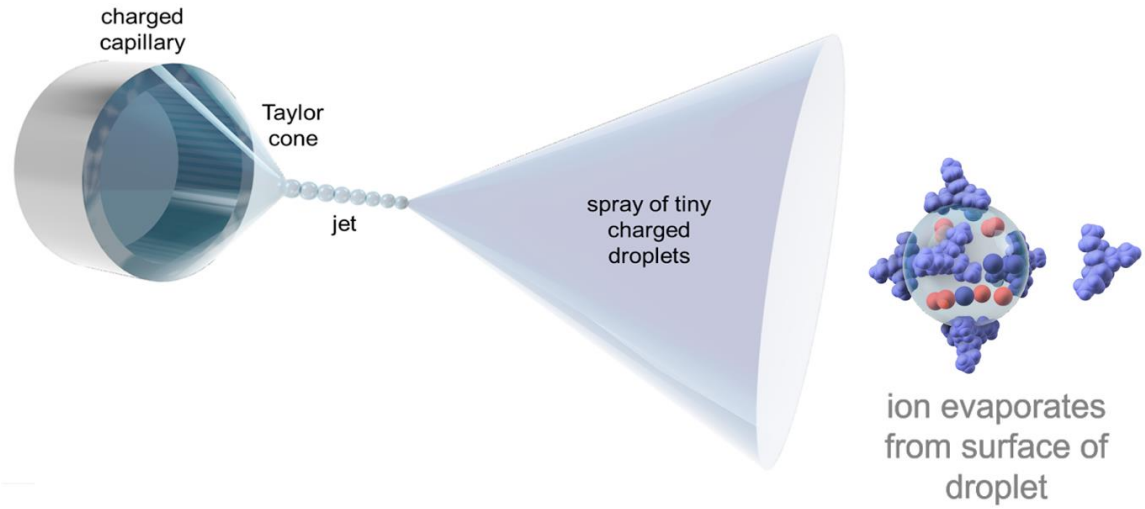

Figure 1.3. Illustration of the electrospray ionization ion evaporation process.

According to the literature, there are two models to explain ionization mechanisms in ESI: the ion evaporation model (IEM) and the charged residue model (CRM).[13] The IEM explains the ionization process for low molecular weight ions, proposing that the high electric field causes charged ions to be expelled from the droplet surface. In contrast, the CRM applies for large ions such as biological macromolecules, where desolvation leaves behind a multiply-charged ion that can be characterized as $[M + nH]^{n+}$ ions.

ESI-MS is a fast technique, suitable for polar compounds of all sizes. It allows studying products and reactants as well as intermediates, resting states, and decomposition

materials.[27] It can analyze complex mixtures with high resolution distinguishing between different species based on their mass-to-charge ratios. It also has high sensitivity and therefore enables the detection of transients, and hence low concentration catalytic intermediates which are difficult to detect using other less sensitive techniques. A combination of *m/z*, isotope pattern, and fragmentation behavior can be used to characterize new species.[28]

ESI-MS is particularly well suited for transition metal complexes as it is a 'soft ionization' method which minimizes analyte fragmentation by minimizing the internal energy transmitted to analytes, in contrast to 'hard ionization' techniques.[29] This technique is important because transition metal complexes are generally considered as quite weak complexes hence especially benefit from softer techniques. Therefore, ESI maximizes the chance of observing transition metal complexes in the complex mixtures that form during cross-coupling reactions. For examples, ESI-MS finds applications across various catalytic reaction analysis such as olefin polymerization,[30] hydroformylation,[31] decarboxylation,[32] esterification,[33] and palladium-catalyzed cross-coupling.[34]

1.4 Mass Analyzers used in MS

The ionized gaseous analyte molecules enter the mass analyzer to be separated and analyzed based on their *m/z* ratio. There are several types of mass analyzers including sector, ion trap, quadrupole, triple-quadrupole, time-of-flight (TOF) and orbitrap.[35] These various mass analyzers have different resolutions, mass ranges, and capabilities. Generally, very high resolution requires a very long mean free path length, and hence a very expensive vacuum system. Cheaper instruments have much lower requirements

in this regard.

1.4.1 Quadrupole Mass Analyzer

A quadrupole mass analyzer is a small, cheap, robust system which has four symmetrical cylindrical hyperbolic rods (5-15 mm diameter, 50-250 mm long) parallel to each other (**Figure 1.4**) charged with direct current (DC) and superimposed radio frequency alternating current (RF-AC).[35] Each pair of parallel electrodes is subjected to the same voltage magnitude but with opposite signs (+/-). As ions enter the quadrupole field from the ion source, they travel along the z-axis through the center of the electrodes. The voltages on the electrode pairs alternate periodically, causing positive ions to be attracted to the negative electrodes and then repelled when the voltage polarity switches, directing them toward the opposite electrodes, while the reverse occurs for negative ions. A quadrupole acts as a mass filter because ions with a particular *m/z* ratio can successfully pass through the quadrupole and reach the detector to produce a signal; all other ions will collide with the electrodes, discharge and never reach the detector.

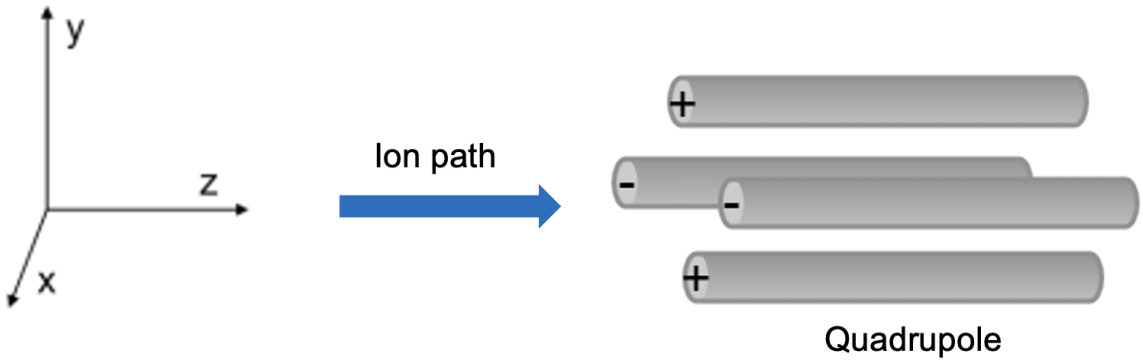

Figure 1.4. A simplified diagram of a single quadrupole mass analyzer with voltages displayed on the charged electrodes of the quadrupole.

The quadrupole mass analyzer performs two functions: (1) full scan mode i.e. it can scan a specific *m/z* range (for instance, from *m/z* 50 to 2000), (2) selection mode, where it remains fixed on a particular *m/z* value. The latter is useful in MS/MS analysis, where the selected ion is fragmented in a proceeding collision cell.

1.4.2 Time of Flight (TOF) Mass Analyzer

In a TOF mass analyzer, when ions reach a device called the pulser, they are propelled down a flight tube in a perpendicular direction.[35] However, the same *m/z* ratio ions within each group have a range of kinetic energies and their moving directions are also different as their formation conditions were not identical. The ions spread out after acceleration, and early TOF instruments suffered from low resolution as a result. This situation was dramatically improved by the invention of the reflectron, an ion mirror that reversed the direction of the ions at the far end of the flight tube. The fastest moving ions penetrate the reflectron field further than do the slowest moving ions. The reflectron repels ions back down the flight tube and performs two tasks: (1) it doubles the length of the flight tube and (2) increases the resolution by allowing higher kinetic energy ions to penetrate deeper and take longer paths, thus aligning their arrival times at the detector with those of slower ions (**Figure 1.5**).

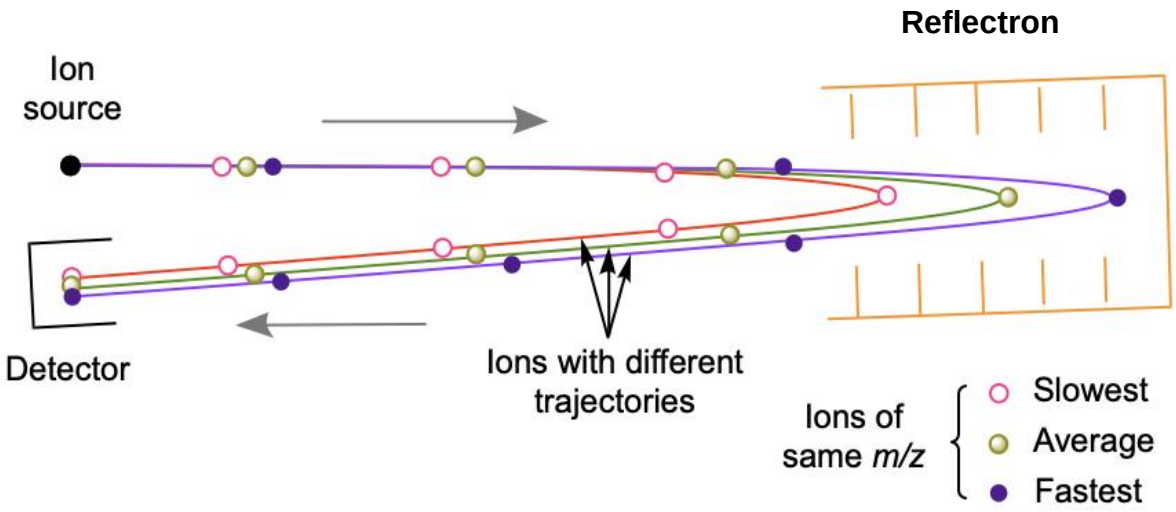

Figure 1.3. A simplified illustration of Time-of-Flight analyzer including essential components. Adapted with permission from Mass Spectrometry of Inorganic and Organometallic Compounds: Tools - Techniques - Tips, J. Scott McIndoe, William Henderson, ISBN: 978-0-470-85016-9, 2005.

This time-focusing mechanism ensures that ions of the same *m/z* reach the detector simultaneously, resulting in sharper and more resolved peaks in the mass spectrum. TOF requires a good vacuum as the mean free path length of ions must be in excess of the length of the flight tube.

The detector is the final destination for the ions. Detectors in mass spectrometry convert ions into measurable electrical signals. Ideally, detectors should possess a wide dynamic range and should give a linear response. Dynamic range refers to the range of signal intensities or quantities that a detector can accurately measure, and linear response means that the detector's output signal is directly proportional to the input signal over a specified range. Detectors typically consist of electron or photomultiplier tubes. An electron multiplier can amplify the ion signal by causing each ion to generate a cascade of electrons through a series of dynodes. This amplification process results in a stronger electrical signal. Microchannel plates (MCPs) are commonly used

detectors in TOF-MS, amplifying the ion signal through secondary electron emission.[36] This amplification allows for the detection of even low-abundance ions, ensuring high sensitivity and accurate mass analysis. These MCPs contain thousands of electron multipliers, the strength of the current depends on the number of ions that arrive at MCP and are used in orthogonal TOF systems because the ions do not all arrive at the same point in space (the pulser dispatches a section of the ion beam emerging from the collision cell).

1.5 Tandem Mass Spectrometry and Collision-Induced Dissociation (CID)

Tandem mass spectrometry is a synonym for mass spectrometry/mass spectrometry (MS/MS).[13] This process involves two stages: first, precursor ions are analyzed, and then these ions undergo fragmentation. This fragmentation produces a product ion and a neutral fragment, each with different masses. The resulting ions are then displayed on the mass spectrum, showing their distinct mass-to-charge ratios (the neutrals are not observed, they are pumped away by the vacuum system). There are various ways to perform MS/MS analysis, and among them, Collision-induced dissociation (CID) is the most commonly employed method.[37] In CID, fast travelling intact molecular ions are accelerated into a collision cell by an applied voltage where they collide with gas (usually an inert monoatomic gas, e.g. argon or xenon) at (relatively) high pressure in the collision cell (typically a hexapole for good ion confinement). Collision induced dissociation happens in this cell. In MS mode, this gas cell works as a hexapole RF lens

to facilitate ions to pass through to the analyzer. In contrast, the ions start generating fragments in MS/MS mode as the ions hit the collision gas and break apart because of the higher collision voltage resulting in the accumulation of internal energy, which is relieved by unimolecular decomposition. These fragmented ions are then detected by the second mass analyzer. The fragmentation pattern of the product ion is acquired in the mass spectrum and will provide important structural information of the parent ion. Collision-induced dissociation is important to detect information about the bond types inside a molecule. Particularly, bond strength information can be detected by CID according to the required collision energy to break down a molecule to fragments.[38] The MS^n is used to describe the number of times of ions that have been through the mass analysis/ selection process.[38]

Several modes of analysis exist in MS/MS, together with product ion scans, precursor ion scans, and neutral loss scans (most of these require a triple quadrupole mass analyzer). Among these available modes, product ion scans (**Figure 1.6**) are most frequently used to identify unknowns, and this type of scan is available for triple quadrupoles and hybrid instruments alike.

In product ion scans, a specific *m/z* value is selected then the fragmentation occurs and finally all resulting *m/z* values are detected and recorded. This reveals all fragments of a specific *m/z* ion and facilitates the analysis of its composition.

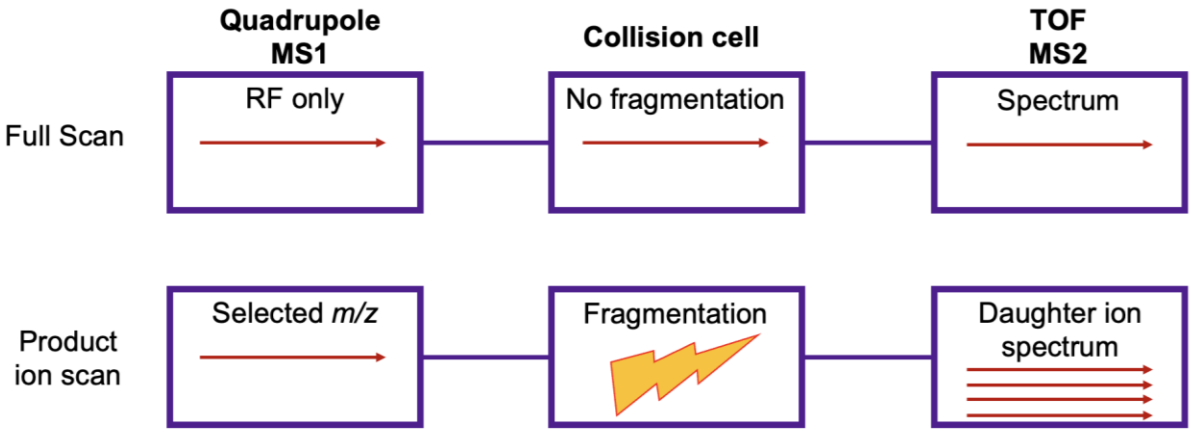

Figure 1.6. Tandem mass spectrometric scan modes on Quadrupole-TOF mass analyzers showing full scan mode and product ion scan mode.

1.6 Pressurized Sample Infusion (PSI)

Pressurize Sample Infusion (PSI) is a method for introducing samples into a MS that enables the direct injection of a reaction mixture for real-time experimental data collection.[39] The setup is shown in **Figure 1.7**.

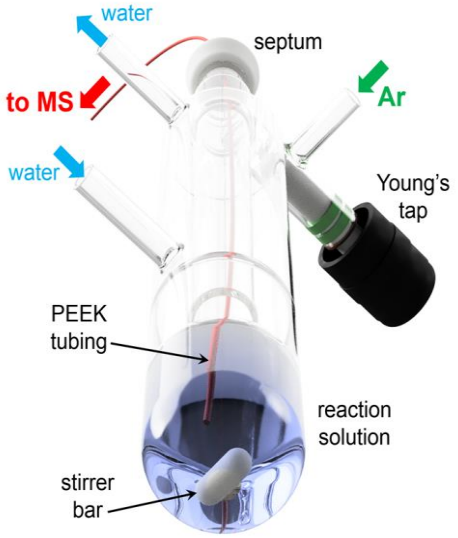

Figure 1.7. Pressurized-sample infusion with a customized Schlenk flask set.

This method is essentially a cannula transfer with a very slow flow rate[39]. The Hagen-Poiseuille equation can approximate the flow rate using the overpressure, the length and inner diameter of the capillary tubing, and the viscosity of the solvent.[40] This technique is straightforward to integrate with ESI-MS. The setup involves a Schenk flask containing the reaction mixture, which is sealed with a rubber septum and connected to an inert gas source, generally nitrogen or argon. A chromatography capillary tubing, such as polyether ether ketone (PEEK), is inserted through the septum and submerged in the reaction mixture. The pressure inside the flask (1-5 psi) forces the solution through the capillary tubing and into the ESI inlet at a flow rate of approximately 5-10 μL/min.[41]

The PSI setup is suitable for analyzing air or/and water sensitive reactions since the Schlenk flask is sealed and purged with inert gas. This setup can be easily transferred into a glovebox for preparing reaction starting materials prior to an ESI-MS experiment. Additionally, solvents and reagents can be added to the flask via a syringe through the rubber septum. Modifications can also be made to the Schlenk flask, such as adding an integrated condenser to enable reflux conditions.[42]

1.7 Continuous Reaction Monitoring using PSI-ESI-MS

All the analytical techniques covered in section 1.1 are suitable for monitoring the entire reaction process. However, ESI-MS offers distinct advantages over all the other instruments in the context of organometallic catalytic reactions. Most catalytic reactions are complex mixtures in a dynamic environment which changes in every second containing starting materials, catalysts/pre-catalysts which present in very low

concentration, intermediates, products, by-products, and decomposing compounds making the analysis complicated. All these individual species in the reaction flask (provided they carry a charge) can be detected, identified, and analyzed in real time by PSI-ESI-MS. More importantly, this technique is highly effective for monitoring air- and moisture-sensitive reactions, providing inert environmental conditions as described in section 1.6.

The main difference between the traditional offline reaction monitoring and the online reaction monitoring is that the offline monitoring provides data as a "snapshot" of the sample composition, whereas the continuous monitoring of a reaction in online mode gives the "temporal profile" of species in the reaction mixture, from which kinetic and dynamic data can be directly obtained. Therefore, this real-time reaction monitoring using PSI-ESI-MS allows data collection while the reaction is in progress and is of great significance in elucidating short-lived reaction intermediates.[43, 44, 45] This technique was used to study alkyl exchange in methylalumoxane, a very dynamic, fast, and difficult system to study.[43] The continuous monitoring of ring closing metathesis reactions using the real-time PSI-ESI-MS analysis has shown the complexity of speciation, the dynamic behavior of the various off-cycle intermediates and by-products formed.[47] Furthermore, understanding the polymerization catalysis is complex because the catalyst's identity changes with each monomer addition. This challenge has been successfully overcome using multiple reaction monitoring (MRM) combined with PSI-ESI-MS, effectively tracking all stages of reactions like Suzuki polycondensation in real time, offering exceptional sensitivity and low signal-to-noise ratios.[48] The experimentally unexplored mechanism of Pd-catalyzed cross coupling between N-tosylhydrazones and aryl halides has been investigated using real-time PSI-ESI-MS,

exploring the catalytic intermediates as well as the kinetic profile of the reaction.[43]

Overall, the reasons for using combined PSI-ESI-MS for real-time reaction monitoring can be highlighted as the speed, robust sample delivery system, ability to cope with complex mixtures, and extremely high sensitivity of MS.

1.8 Objectives

The main goal of this thesis was to use the PSI-ESI-MS technique to investigate the effects of sulfur-based poisons on palladium-catalyzed cross-coupling reactions. This investigation gives molecular insight to the field of poisoning of homogeneous catalysts. This improved understanding of homogeneous catalyst poisoning can be applied to systems where the reaction needs to be terminated at a certain point of a catalytic cycle by deliberately introducing the poison into the reaction mixture.

Constructing calibration curves for quantification (for example, poisoning quantification) is a timely need since MS quantification is non-linear and complex. A one-experiment for calibration which can be applied to various instruments has developed to make calibration faster and easier. This project is described in chapter 3 of this thesis, along with the combination of programming tools and innovative experimental design.

Chapter 2

Effect of Sulfur-based poisons on palladium-catalyzed cross coupling: A real-time analysis

Abstract

Catalyst poisoning is the partial or total chemical deactivation of a catalyst, and understanding this catalyst poisoning process is crucial because it helps to optimize the industrial chemical reactions as well as it gives the molecular insight to the field of poisoning of homogeneous catalysts. The aim of this study was to understand catalyst poisoning behavior by introducing a poison into a reaction flask containing a Pd cross-coupling reaction solution and then monitoring the reaction in real-time using PSI-ESI-MS. In this context, three sulfur-based poisons: 1,2-benzenedithiol, thiourea, and *N*-acetylcysteine were examined on a Pd(0) precatalyst, and on the product of the initial step in most cross-coupling reactions, the Pd(II)(Ph)X oxidative addition product. All three poisons reacted rapidly with Pd(0), all via the oxidation of the Pd to Pd(II) and deprotonation of the poisons, revealing significant changes in the Pd complexes.

2.2 Introduction

2.2.1 Catalyst Poisoning

Catalyst poisons are unwanted additives in a reaction mixture, often contaminants in the solvent or reactants.[49] Partial or total chemical deactivation of a catalyst is known as catalyst poisoning.[50] This catalyst poisoning process involves the destruction of catalyst performance via the introduction of an unwanted additive. The normal course of action is irreversible binding of the additive to the catalyst, preventing the catalyst from performing its usual tasks. The poison itself may be a contaminant in the reactants

or solvent or it may be something that intrudes on the catalyst system adventitiously, such as water or oxygen.

The mechanism of catalyst poisoning involves the binding of the poison to the catalyst, resulted in weakened activity.[51] It can occur for both homogeneous catalysts (same phase as the substrate, and/or single active site = homotopic) and for heterogeneous catalysts (different phase as the substrate, and/or multiple active sites = heterotopic).[52,53,54] Organic functional groups, inorganic anions, small molecules (such as halides, sulfides, sulfites, phosphates, phosphites, nitro compounds), and nitrogen-containing heterocycles are all common catalyst poisons.[55]

Even though catalyst poisoning is nearly always undesirable because of the reduced catalyst activity, corresponding wasting of metal complexes, and the replacement of inactive catalysts which significantly contributes to the expenses incurred in technical processes, improved catalyst selectivity can be achieved by introducing suitable poisons into catalytic systems. Pb-poisoned Pd catalyst (Lindlar catalyst) is the most famous example of a beneficial use of the modulation of catalyst poisons.[56] Similarly, thiols have been used to poison palladium catalysts to improve their selectivity towards the semi hydrogenation of internal alkynes.[57] Thiols have also been used to tether palladium catalysts inside a metal-organic framework without completely poisoning the catalyst.[58] Thiol-functionalized silica types have been used as a means of removing residual palladium from the products of cross-coupling reactions.[59] A selective example of a homogeneous catalyst poison is dibenzo[a,e]cyclooctatetraene, which has the ability to completely poison homogeneous catalysts, such as $RhCl(PPh_3)_3$, while having little to no effect on heterogeneous catalysts.[60]

Concerted efforts to understand the chemistry of poisoning are not common in the homogeneous catalysis literature yet (it is the subject of a huge body of research in the heterogeneous catalysis literature).[56,61,62] It is often enough to know that a molecule has a deleterious effect on catalyst performance and, therefore, should be carefully excluded from the operating system (perhaps by the additional purification of reactants or solvents, or attention to the exclusion of air and moisture). Exactly how a poison acts on the catalyst is probably considered to be of secondary importance.

2.2.2 Sulfur-based catalyst poisons

Sulfur acts as a critical contaminant in catalytic combustion and oxidation reactions in the exhaust of lean-burn natural gas engines.[63] Thiourea, $(NH_2)_2CS$, was found to be an effective poison for active soluble palladium species in Heck reactions to differentiate the active palladium from Pd/C and from a polyurea encapsulated Pd-$(OAc)_2$.[64] Homogeneous catalysts poisons, such as silica-bound thiol scavengers have the ability to remove residual Pd from the Heck reaction solution.[65] *N*-acetylcysteine is used as a poison to coordinate palladium to keep it in the solution when a product is being crystallized out.[66] It also acts as a ligand in a solvent to selectively extract palladium out of other solutions.[67] Thiols can poison the Suzuki-Miyaura reaction, forming disulfide products instead of the desired cross-coupling product,[68] necessitating the use of protective groups.[69] Thiols can themselves be used as coupling partners in cross-coupling reactions in the presence of a strong base, and this transformation was first discovered by Migita[70] that has since been greatly developed.[71]

According to the literature, the purpose of most of previous work was to identify

poisons on a catalytic cycle and their catalyst performance, and hence to take measures to avoid or exclude these types of poison from the investigated operating system.[72]

For example, additional purification of solvents can be performed to remove solvent contaminants as well as air and moisture from the reaction mixture, if the reaction is sensitive to these issues. However, in the context of homogeneous catalyst poisoning, the chemical behavior of catalyst poisons and how the poisons bind to the catalyst are under-explored areas. Therefore, the improved understanding of homogeneous catalyst poisoning is crucial because it can be applied to systems where the reaction needs to be terminated at a certain point of a catalytic cycle by deliberately introducing the poison into the reaction mixture. This concept is important in the pharmaceutical industry because synthetic intermediates and products need to be rigorously analyzed for residual catalyst-derived compounds. Further, specific poisons can be introduced into the catalyst systems to modulate their reactivity, improve regioselectivity, and expand functional group tolerance. Homogeneous catalyst poisoning may also be used to ensure process safety, such as to control reaction exotherms by deactivating the catalyst at specific time. Moreover, catalyst poisoning is useful for side reaction suppression. For example, intermediates can undergo unwanted side reactions, which leads to decreased yield and the formation of impurities. This issue can be overcome by introducing suitable catalyst poison thereby selectively suppressing side reactions. Overall, this chapter will give molecular insight into the field of the homogeneous catalyst poisoning of Pd-catalyzed cross-coupling reactions.

2.2.3 Research Motivation

The aim of this study was to understand catalyst poisoning behavior by introducing the poison into a reaction flask containing a cross-coupling reaction solution then monitoring the reaction in real-time using PSI-ESI-MS. The principal catalytic system chosen was Pd catalyst, then monitoring the effect of the poison on catalyst activation and oxidative addition steps, where Pd is in the Pd(0) and Pd(II) oxidation states. The main reason to choose this system was that Pd is used as a catalyst in most cross-coupling reactions, including Suzuki-Miyaura cross coupling, Heck reaction, Sonogashira coupling, Negishi coupling, Stille cross-coupling, Hiyama coupling, Buchwald-Hartwig amination reaction, Fukuyama coupling, and cross dehydrogenative coupling, etc.[73] The first two steps (catalyst activation and oxidative addition, **Scheme 2.1**) are common to most cross-coupling reactions.

Many cross-coupling reactions have oxidative addition as the turnover-limiting step, which means that Pd(0) complexes are typically the resting state. Therefore, the results of our studies are applicable to a wide range of reactions without having to include the many possible transmetallating agents. There are many potential poisons, so we started with a subset of molecules used intentionally as poisons: a small selection containing sulfur donors.

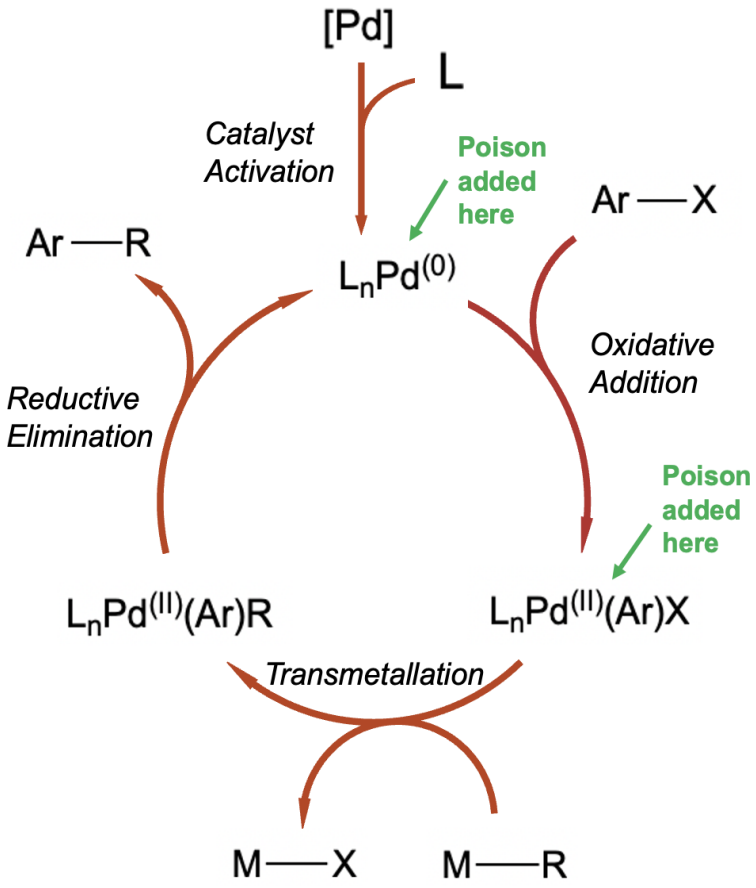

Scheme 2.1. A generic Pd-catalyzed cross-coupling catalytic cycle. Poisons were introduced to the system at the two points shown.

2.3 Results and Discussion

Tetrakis(triphenylphosphine)palladium(0), $Pd(PPh_3)_4$ was used as the Pd precatalyst, and mono-sulfonated triphenylphosphine $[PPh_2(m\text{-}C_6H_4SO_3)]^-$ (TPPMS, **1**) was used as the charge-tagged ligand in conjunction with the PPN counterion $[(Ph_3P)_2N]^+$.[74] We examined three sulfur-based poisons: 1,2-benzenedithiol (**2**), thiourea (**3**), and *N*-acetylcysteine (**4**).

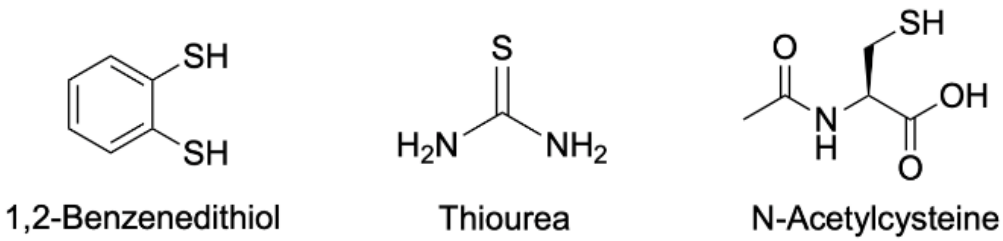

Figure 2.1. Selected S-based poisons for this study

2.3.1 Poison: 1,2-benzenedithiol

2.3.1.1 Poisoning of Pd(0)

The addition of $Pd(PPh_3)_4$ to $[\mathbf{1}]^-$ resulted in rapid equilibration within a minute to a mixture of $[Pd(PPh_3)_n(\mathbf{1})]^-$ (n = 0-2). Such a mixture is typical in ESI-MS analysis because these ligands readily dissociate in the source of the instrument,[75] so in all traces we have combined these species together. The addition of benzenedithiol resulted in rapid disappearance of all of these ions with a half-life of 1.4 seconds (see **Figure A1** with the detailed description for half-life determination). **Figure 2.2** shows the traces and **Figure 2.3** shows the poisoned products with isotope pattern overlays.

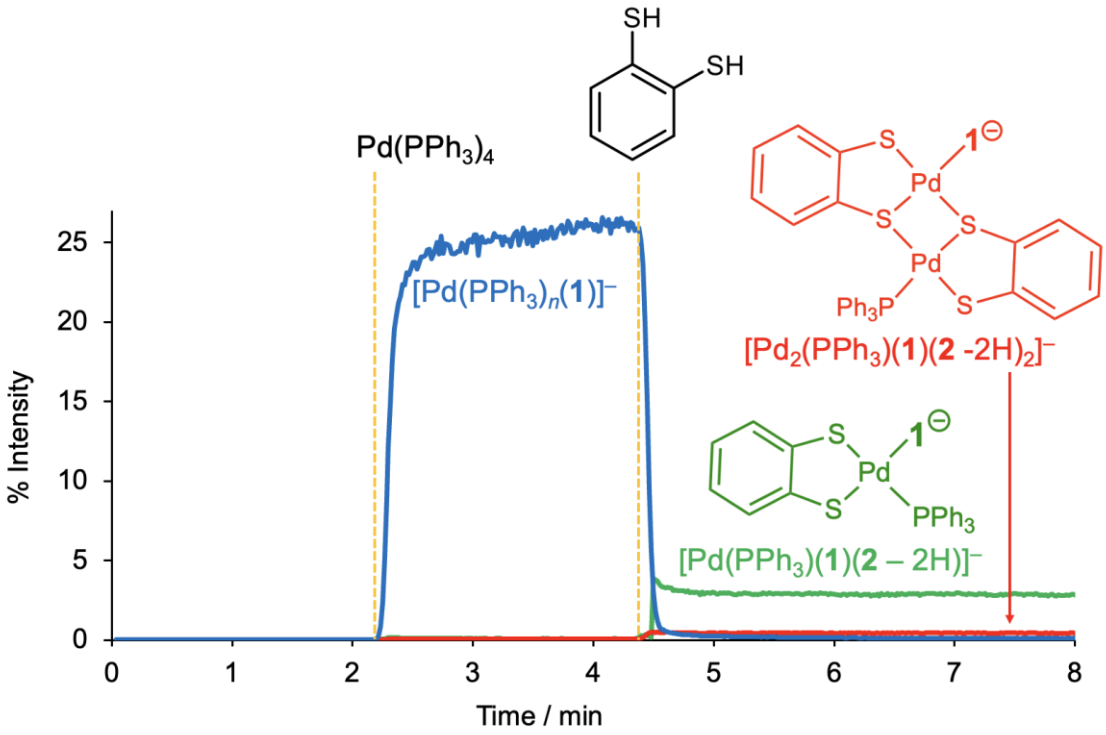

Figure 2.2. PSI-ESI-MS reaction monitoring in negative ion mode showing the effect of poison: 1,2-benzenedithiol addition on catalyst activation. A drop in the relative abundance of $[Pd(PPh_3)_n(\mathbf{1})]^-$, where n = 1-2, is observed upon the addition of the poison and formation of Pd poisoned products are shown in red and green color traces.

Given that the time taken for the solution to reach the MS is of the order of about 20 seconds, this estimate is an upper bound for the half-life and the reaction may in fact be much faster. The Pd(0) species are replaced by two Pd-containing compounds, both Pd(II): $[Pd(PPh_3)(\mathbf{1})(2\text{-}2H)]^-$ and $[Pd_2(PPh_3)(\mathbf{1})(\mathbf{2}\text{-}2H)_2]^-$. We also observed trace amounts of an ion corresponding to $[Pd(PPh_3)(\mathbf{1})(\mathbf{2}\text{-}2H)_2]^-$ (see **Figure A14** in appendix), but was insufficient to conduct MS/MS studies.

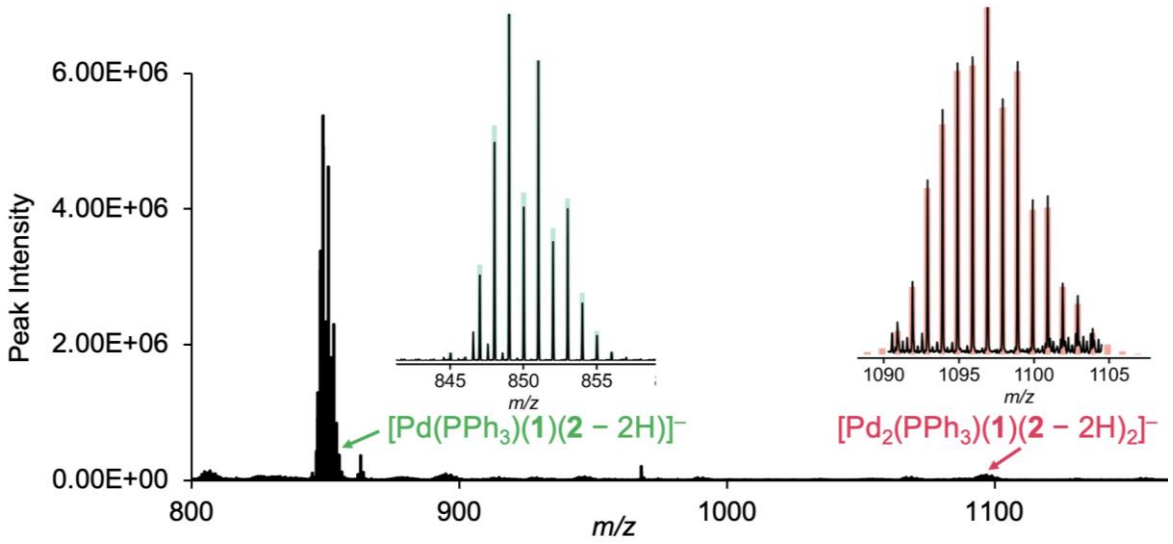

Figure 2.3. PSI-ESI-MS scan on $(PPh_3)_4$ added to $[\mathbf{1}]^-$ in negative ion mode showing two Pd-poisoned product peaks. Insets show the predicted isotope pattern (bars) overlaid on the experimental isotope pattern (lines).

The identity of the Pd-poisoned products were determined using a combination of MS/MS fragmentation data, chemical intuition, and literature precedent. Both species fragmented by the loss of PPh_3 or **1**, a typical pathway for coordination complexes with a mixture of L- and X-type ligands.[28] As such, it seemed clear that the loss of H must be from the benzene dithiol ligand rather than the C-H activation (orthometallation) of the phosphine ligands. There is literature precedent for both $Pd(PR_3)_2$(**2**-2H) and $Pd_2(PR_3)_2$(**2**-2H)$_2$ type complexes.[76]

The mass balance in this transformation is off (apparently more reactants than products), which in the context of ESI-MS can mean one of three things: (a) the ESI-MS response factor for the products is lower than that of the reactants;[77] (b) the charged tag has a lower affinity for the products; or (c) some charge neutralization process is contributing to the reduced prominence of the products. For (a), variations in response

factor arise through differences in surface activity (i.e., the propensity for an ion to be found on the surface of the droplet rather than solvated and ion paired in the interior of the droplet). These differences can be accounted for if the individual species can be isolated and combined in known concentrations; however, in this case, we are looking at a dynamic equilibrium. In the case of (b), the competition between PPh_3 and $[\mathbf{1}]^-$ is complicated by the fact that the Pd:phosphine ratio changes between reactant and products. It is 3:1 for $[Pd(PPh_3)_2(\mathbf{1})]^-$, 2:1 for $[Pd(PPh_3)(\mathbf{1})(\mathbf{2}\text{-}2H)]^-$, and 1:1 for $[Pd_2(PPh_3)(\mathbf{1})(\mathbf{2}\text{-}2H)_2]^-$. That translates to a lower chance for the phosphine to be $[\mathbf{1}]^-$ rather than PPh_3; therefore, there will be more free $[\mathbf{1}]^-$ for the latter complexes. Finally, the possibility of charge neutralization, (c) can be examined by following the reaction in the other ion mode in the absence of a charged tag. This strategy works because whatever process that would lead to charge neutralization in the negative ion mode will instead lead to the formation of a cation in the positive ion mode.

The addition of $Pd(PPh_3)_4$ to the infusing solution in the positive ion mode in the absence of a charged tag results in the immediate appearance of $[Pd(PPh_3)_n]^{\cdot+}$ radical cations (**Figure 2.4**). This observation is consistent with other investigations,[78] in which Pd(0) complex is very electron-rich and oxidation is facile, so the electric field applied in the ESI-MS source is more than sufficient to remove an electron from the complex. The addition of 1,2-benzenedithiol causes the disappearance of nearly all of those radical cations, and the only new Pd-containing species to appear is $[Pd(PPh_3)_2(\mathbf{2}\text{-}H)]^+$, the protonated analogue of the $[Pd(\mathbf{1})(PPh_3)(\mathbf{2}\text{-}2H)]^-$ observed in the negative ion mode. The charge balance problem can be accounted for by differences in response factors.

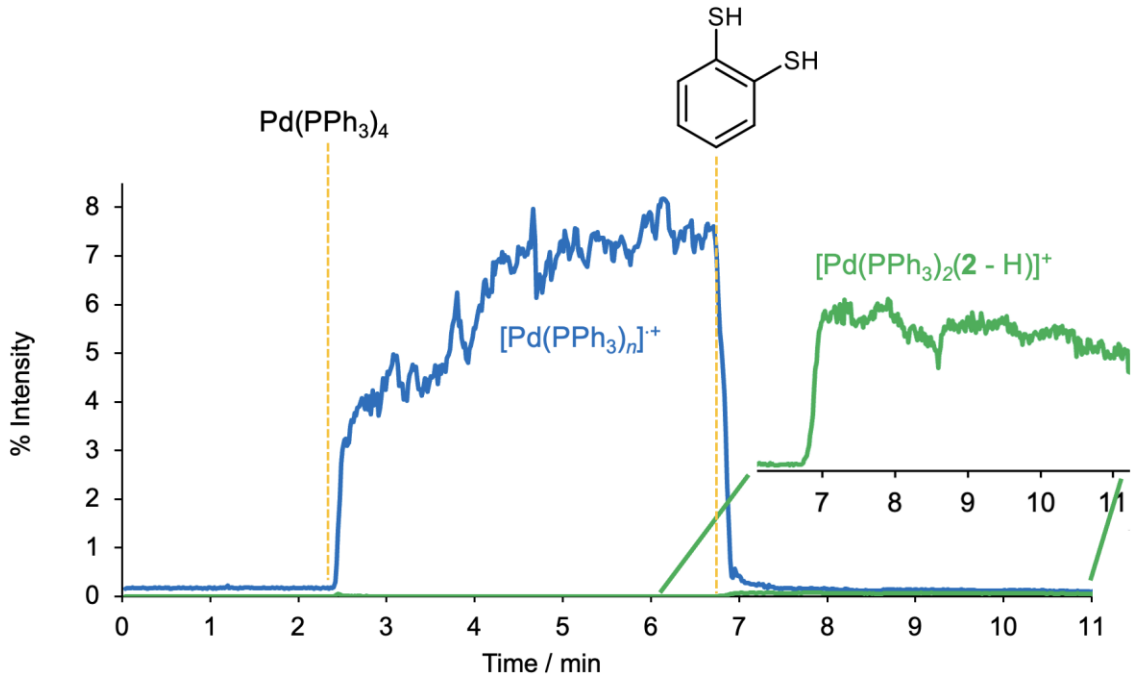

Figure 2.4. PSI-ESI-MS reaction monitoring in positive ion mode showing the effect of poison: 1,2-benzenedithiol addition on catalyst activation. A drop in the relative abundance of $[Pd(PPh_3)_n]^{\cdot+}$, where n = 1-2, is observed upon the addition of the poison and formation of the Pd poisoned product is shown in green (scale exaggerated by a factor of 20).

2.3.1.2 Poisoning of Pd(II)

Pd(0) species react with aryl halides to form Pd(II) oxidative addition products. We used PhI, because aryl iodides react most quickly out of the aryl halides.[79] We observed $[Pd(PPh_3)_n(\mathbf{1})]^-$ to convert to $[Pd(PPh_3)(\mathbf{1})(Ph)(I)]^-$ on the timescale of seconds, and left the system to equilibrate for a few more minutes before adding the benzenedithiol. We saw the $[Pd(PPh_3)(\mathbf{1})(Ph)(I)]^-$ quickly disappear, to be replaced by $[Pd(PPh_3)(\mathbf{1})(\mathbf{2}\text{-}2H)]^-$. However, the abundance of this species was very low, and grew in quite slowly, suggesting that it does not form immediately as a result of the addition of benzenedithiol (**Figure 2.5**).

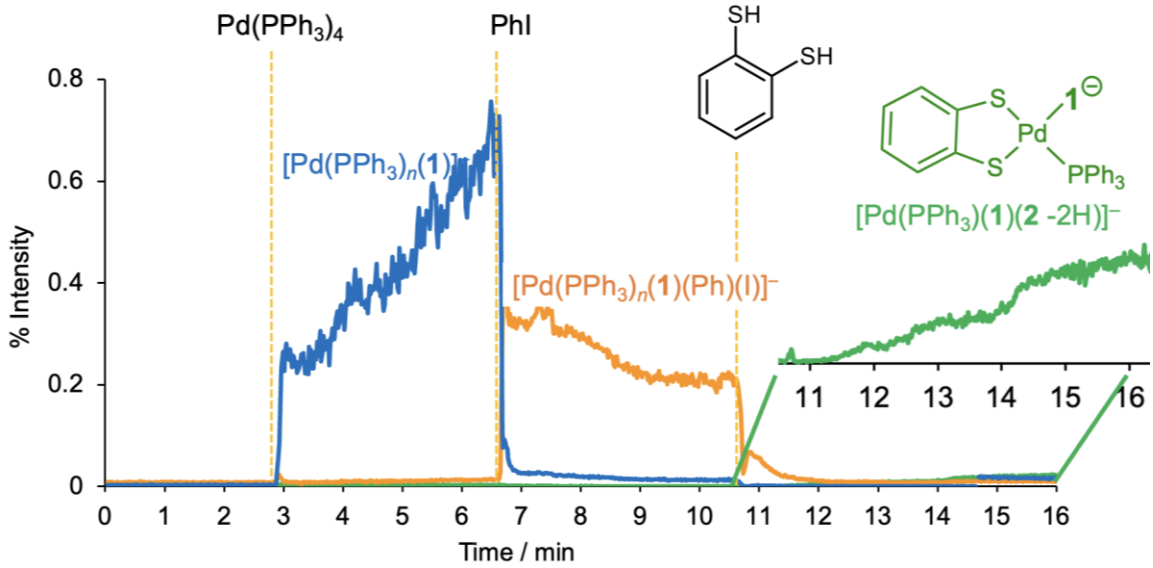

Figure 2.5. PSI-ESI-MS reaction monitoring in negative ion mode showing the effect of poison: 1,2-benzenedithiol addition on oxidative addition. A drop in relative abundance of $[Pd(PPh_3)_n(\mathbf{1})]^-$ (blue trace), where n = 1-2, is observed upon addition of the aryl halide: PhI and the resulting oxidatively added products: $[Pd(PPh_3)_n(\mathbf{1})(Ph)(I)]^-$ (n = 0-1) disappear and the formation of Pd poisoned product is shown in green color trace.

Again, we went to the positive ion mode without the charged tag to try to understand the transformations that were going on in the solution. The disappearance of $[Pd(PPh_3)(\mathbf{1})(Ph)(I)]^-$ suggested that the benzene dithiol was acting as an L-type (neutral) ligand by replacing an X-type (anionic) ligand to produce a cationic complex, which, in conjunction with the negatively charged tag $[\mathbf{1}]^-$, would form an invisible zwitterionic complex, $Pd^{II}(PPh_3)(\mathbf{1})(Ph)(\mathbf{2})$. Metal halide complexes readily lose X^- to form $[M–X]^+$ complexes in ESI-MS studies,[5] and any remaining L-type ligands can occupy the vacant coordination site.

Thiolates react with $L_2Pd(Ar)X$ complexes to form $L_2Pd(Ar)(SR)$ complexes, which can reductively eliminate ArSR to generate L_2Pd.[80] Thiols can react similarly under slightly basic conditions.[81,82] As previously detailed, Pd(0) complexes react directly and quickly with dithiols to form the same complex observed as the final product here. The most likely pathway for the reaction is via the disulfide, as disulfides are known to oxidatively add to Pd(0) complexes to form bisthiolate complexes.[83,84] Palladium is also known to catalyze thiol-disulfide exchange, though under rather more forcing conditions than used here.[85]

In the positive ion mode, we would expect to see $[Pd^{II}(PPh_3)_2(Ph)(\mathbf{2})]^+$ if conducting the experiment without the charged tag $[\mathbf{1}]^-$. However, that is not what we saw; we observed the rapid disappearance of both $[Pd(PPh_3)_n]^{\cdot+}$ (n = 1-3) and $[Pd(PPh_3)_n(Ph)]^+$ (n = 1 or 2), and slow appearance of a peculiar species that corresponded to $[Pd(PPh_3)_2(Ph)(\mathbf{2}\text{-}2H)_2]^+$ (**Figure 2.6**).

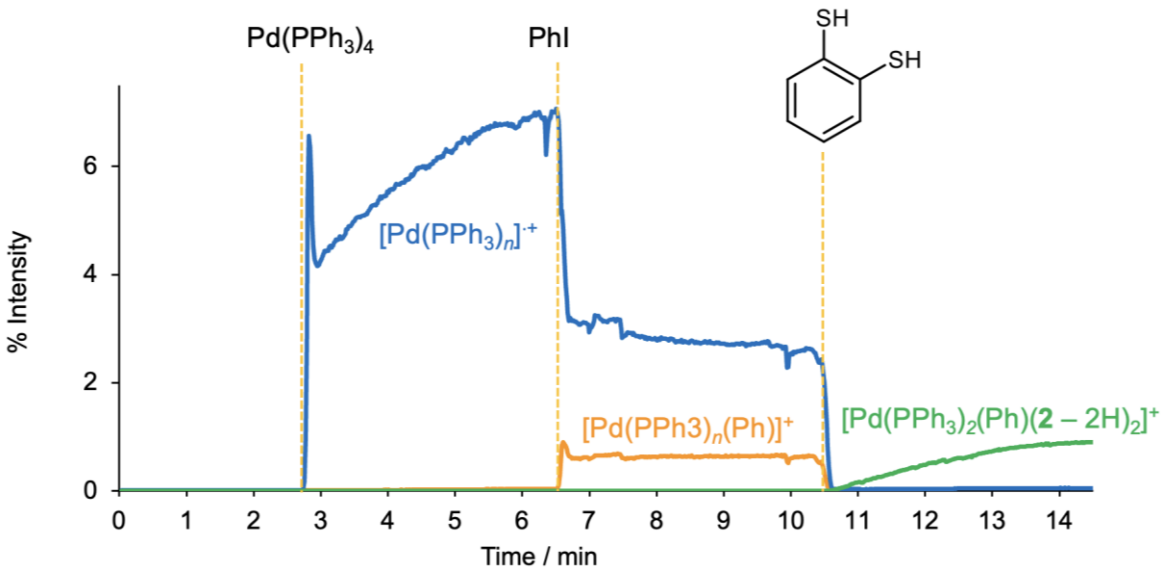

Figure 2.6. PSI-ESI-MS reaction monitoring in positive ion mode showing the effect of poison: 1,2-benzenedithiol addition on oxidative addition. A drop in the relative abundance of $[Pd(PPh_3)_n]^{\cdot+}$ (blue trace), where n = 1-2, is observed upon the addition of the aryl halide: PhI and the resulting oxidatively added product: $[Pd(PPh_3)_n(Ph)]^+$ disappeared and the formation of Pd poisoned product is shown in green trace.

This observation was puzzling since the structure of such an ion is not immediately obvious. The product ion MS/MS spectrum (**Figure 2.7**) confirmed the presence of various components. The first fragmentation pathways were the loss of PPh_3 and (competitive) loss of benzene. The PPh_3 loss was a simple ligand dissociation. Benzene loss is presumably attributed to the combination of the phenyl ligand with a nearby H. The ion that lost a PPh_3, $[Pd(PPh_3)(Ph)(\mathbf{2}\text{-}2H)]^+$, subsequently experienced a neutral loss equivalent to $C_6H_4S_2$ (likely 3,5-cyclohexadiene-1,2-dithione, given the 1,2-benzenedithiol precursor), followed by the loss of $Pd(C_6H_4S_2)$ to form $[PPh_4]^+$. However, putting these component ligands together in a sensible way is challenging

because Pd(II) is typically square planar and 2 × PPh_3, 1 Ph and 2 × $C_6H_4S_2$ (**2**-2H) give 7 possible binding sites.

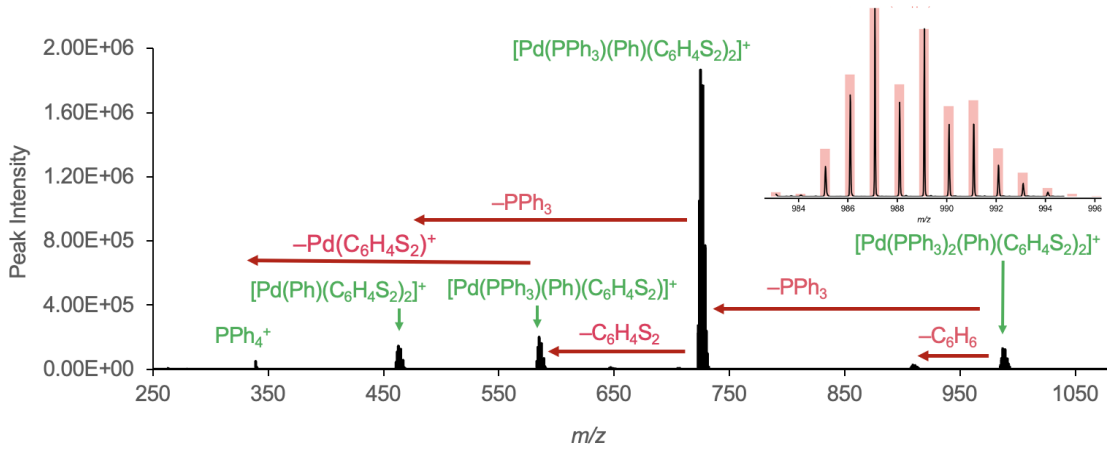

Figure 2.7. The product ion mass spectrum of $[Pd(PPh_3)_2(Ph)(C_6H_4S_2)_2]^+$ obtained on a Synapt G2Si mass spectrometer. Inset shows the predicted isotope pattern (bars) overlaid on the experimental isotope pattern (lines) of $[Pd(PPh_3)_2(Ph)(C_6H_4S_2)_2]^+$.

Benzenedithiol reacts quickly with $L_2Pd(Ph)I$ and can remove it from the solution within a couple of minutes, but the reactivity is complex. The initial products are silent to ESI-MS in both negative ion mode (with charged tag) and in positive ion mode (no charged tag), an unusual scenario that suggests that the reactivity does not involve species that carry a charge. We suspect that the benzenedithiol is better at displacing the phosphines than the phenyl and/or iodide ligand, as any complex without (**1)** in the negative ion mode, or that is a neutral Pd(II) complex in the positive ion mode, will be invisible to ESI-MS.

2.3.2 Poison: Thiourea

2.3.2.1 Poisoning of Pd(0)

The addition of thiourea to a solution of $[Pd(PPh_3)_n(\mathbf{1})]^-$ ions resulted in a rapid reaction with the formation of two main products: $[Pd(PPh_3)(\mathbf{1})(\mathbf{3}\text{-}2H)]^-$ and $[Pd(\mathbf{1})(\mathbf{3}\text{-}H)_2]^-$ (**Figure 2.8**). Note that, in the former case, the thiourea had been doubly deprotonated and, in the latter, each thiourea has been singly deprotonated. We saw no sign of the thiourea acting as a simple L-type ligand, and the reaction though fast did not go to completion, with an appreciable amount of $[Pd(PPh_3)_n(\mathbf{1})]^-$ ions in the equilibrium product mixture.

We can speculate on the likely geometry of these complexes: CID experiments using MS/MS showed that fragmentation proceeds exclusively by phosphine dissociation.

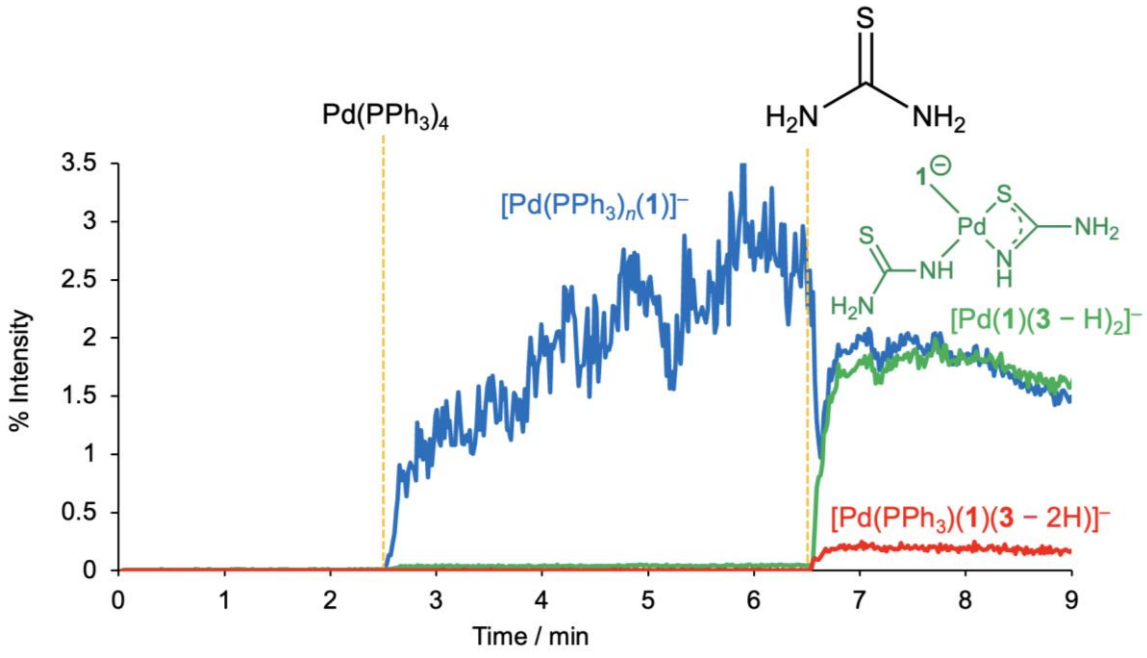

Figure 2.8. PSI-ESI-MS reaction monitoring in negative ion mode showing the effect of poison: thiourea addition on catalyst activation. A drop in the relative abundance of $[Pd(PPh_3)_n(\mathbf{1})]^-$, where n = 1-2, is observed upon the addition of the poison and formation of Pd poisoned products are shown in green and red color traces.

These observations suggest that the thiourea-derived ligands are likely X-type ligands and/or bidentate, and that the complexes that form are not simply thiourea acting as an L-type ligand to displace some of the phosphine ligands. Instead, the palladium is oxidized to Pd(II) to form complexes of the type shown below (**Figure 2.9**).

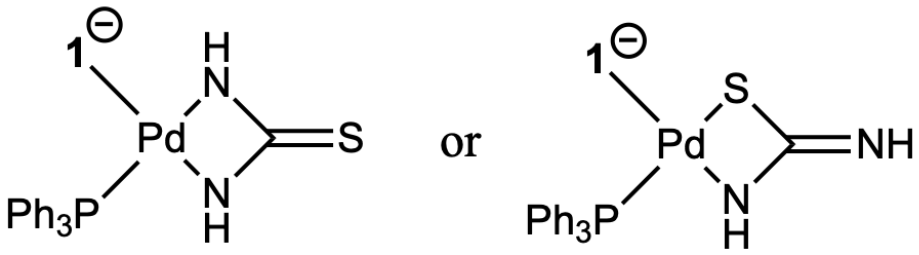

Figure 2.9. Possible structures for $[Pd(PPh_3)(\mathbf{1})(\mathbf{3}\text{-}2H)]^-$ species.

The positive ion mode without charged tag proved to be simpler, where the radical cationic ions $[Pd^0(PPh_3)_n]^{\cdot+}$ were rapidly replaced by $[Pd^{II}(PPh_3)_n(\mathbf{3}\text{-}H)]^+$ (**Figure 2.10**).

We did not see any analogue of the doubly deprotonated ligand, but this observation is unsurprising because that complex is neutral and does not have a good pathway to ionization (X_2-type ligands do not dissociate under CID conditions). Loss of a monodentate X-type ligand is a common ionization pathway, however.

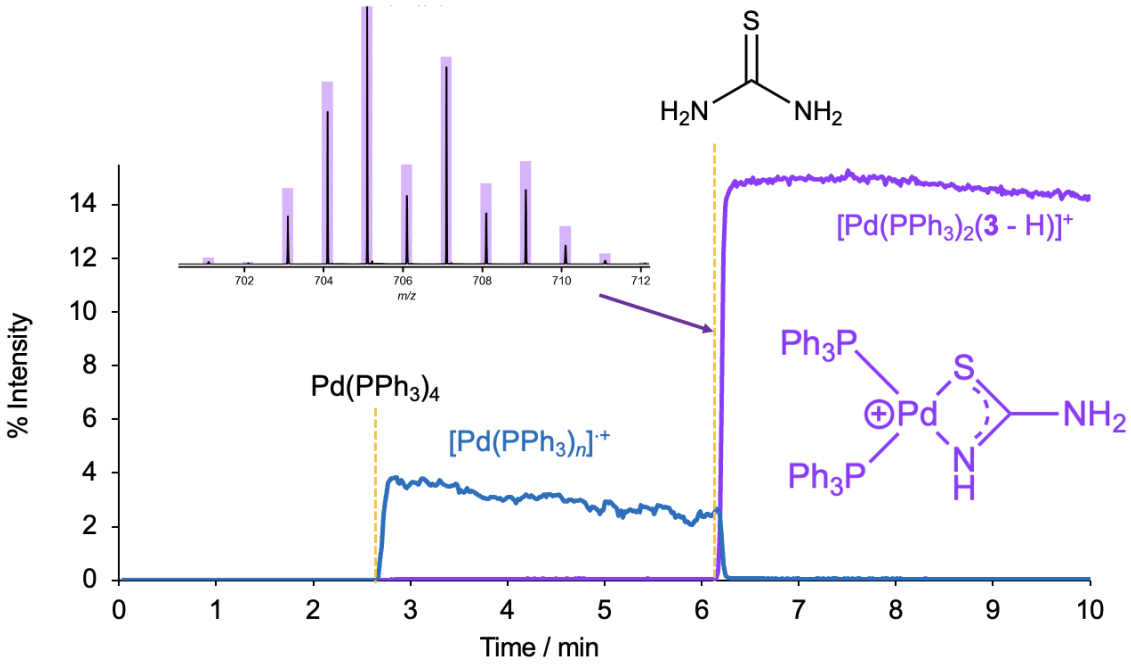

Figure 2.10. PSI-ESI-MS reaction monitoring in positive ion mode showing the effect of poison: thiourea addition on catalyst activation. A drop in the relative abundance of $[Pd(PPh_3)_n]^{\cdot+}$, where n = 1-2, is observed upon the addition of the poison and formation of Pd poisoned products $[Pd(PPh_3)_2(\mathbf{3}\text{-H})]^+$, where n = 1-2, is shown in purple color trace. Inset shows the predicted isotope pattern (bars) overlaid on the experimental isotope pattern (lines).

2.3.2.2 Poisoning of Pd(II)

Adding thiourea to a solution containing $[Pd(\mathbf{1})(PPh_3)(Ph)(I)]^-$ resulted in a fast perturbation of the relative abundance of the species present (see **Figure 2.11**). The drop in the oxidative addition product we attribute to the formation of the zwitterionic species $Pd(\mathbf{1})(PPh_3)(\mathbf{3}\text{-H})$.

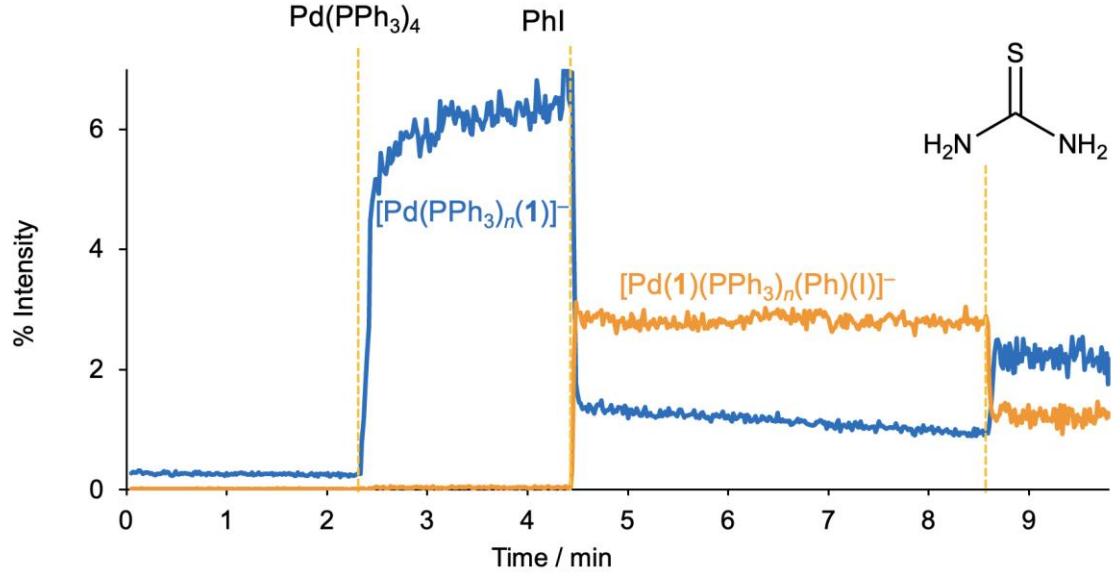

Figure 2.11. PSI-ESI-MS reaction monitoring in negative ion mode showing the effect of poison: thiourea addition on oxidative addition. A drop in the relative abundance of $[Pd(PPh_3)_n(\mathbf{1})]^-$ (blue trace), where n = 1-2, is observed upon addition of the aryl halide: PhI and the resulting oxidatively added product: $[Pd(\mathbf{1})(PPh_3)_n(Ph)(I)]^-$ (n = 0-1), disappeared.

In the positive ion mode, we observed only one new palladium-containing species after the addition of thiourea to a solution containing $[Pd(PPh_3)_n(Ph]^{\cdot+}$, and that was $[Pd(PPh_3)_2(\mathbf{3}\text{-H})]^+$ (see **Figure A11** in appendix). Note that the negative ion mode analogue to this species would be invisible due to its zwitterionic nature (in the presence of the charged tag $[\mathbf{1}]^-$). Hence, we concluded that the observed drop in the abundance of $[Pd(\mathbf{1})(PPh_3)(Ph)(I)]^-$ was due to the formation of $Pd(\mathbf{1})(PPh_3)(\mathbf{3}\text{-H})$.

2.3.3 Poison: *N*-acetylcysteine

2.3.3.1 Poisoning of Pd(0)

N-acetylcysteine is often used as a quench for Pd-catalyzed reactions.[86, 67] Interestingly, in our investigations, *N*-acetylcysteine was a relatively sluggish poison that did not completely react with the catalytically-relevant Pd species observed. The addition of *N*-

acetylcysteine to a solution of $[Pd(PPh_3)_n(\mathbf{1})]^-$ ions resulted in a drop in the abundance of these species and the appearance of the Pd(II) species $[Pd(PPh_3)(\mathbf{1})(\mathbf{4}\text{-}2H)]^-$, where the *N*-acetylcysteine has been doubly deprotonated. The reaction was relatively slow compared to the other poisons, with a half-life of ~10 seconds, and more of the Pd(0) species remained than the Pd(II) species that were produced (**Figure 2.12**).

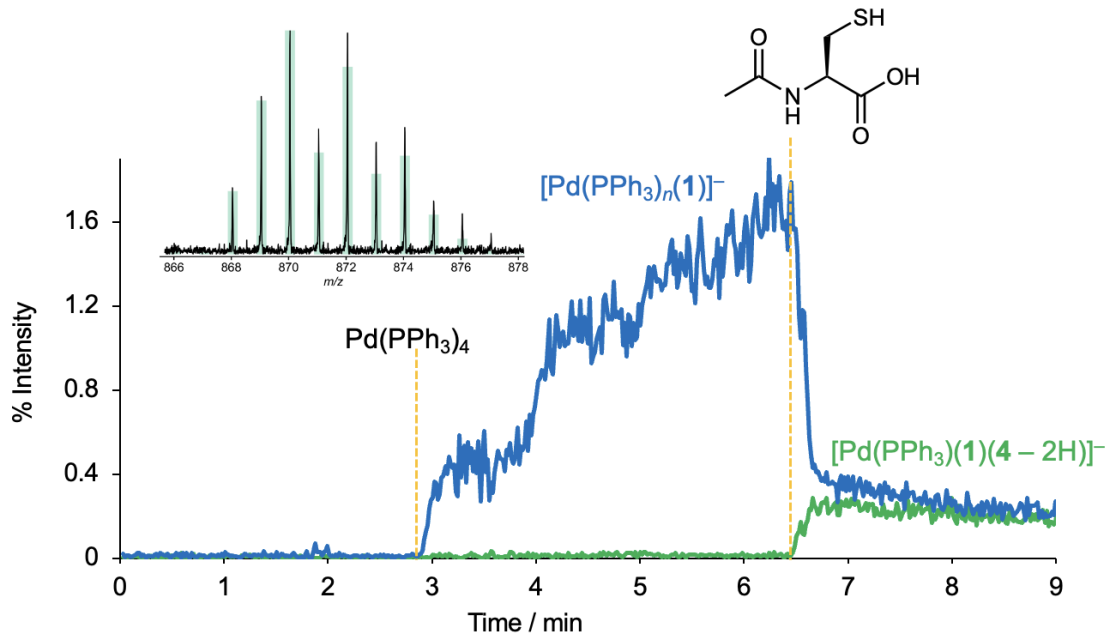

Figure 2.12. PSI-ESI-MS reaction monitoring in negative ion mode showing the effect of poison: *N*-acetylcysteine addition on catalyst activation. A drop in the relative abundance of $[Pd(PPh_3)_n(\mathbf{1})]^-$, where n = 1-2, is observed upon addition of the poison and the formation of Pd-poisoned product is shown in green color trace. The inset shows the predicted isotope pattern (bars) overlaid on the experimental isotope pattern (lines).

N-acetylcysteine-derived ligands are known, including the singly-deprotonated version in $Pb^{II}(4\text{-}H)_2$[84] and $Pd^{II}(\mathbf{4}\text{-}H)_2$, where the binding is through N and S.[88] The doubly-deprotonated version has been observed for platinum in $Pt^{II}(C_5H_7NO_3S)_2$.[89] In that case, the binding mode is via O and S, and the same is true for the osmium complexes of the ligand.[90,91] A dimeric platinum complex is known, $Pt_2(bipyridine)_2(C_5H_8NO_3S)_2$, where

a bipyridine ligand chelates to each Pt atom, and the thiolate ligand is bridging between the two metals.[92] Another Pt^{II} dimeric complex also exhibits bonding exclusively through S.[93] Nevertheless, mass spectrometric analysis is not able to distinguish between the various possibilities (O/S, O/N, N/S).

The summed isotope pattern (inset, **Figure 2.12**) for $[Pd(PPh_3)(\mathbf{1})(\mathbf{4}\text{-}2H)]^-$ is interesting in that it shows signs of overlap with another Pd-containing species higher in *m/z* by two, strongly implicating $[Pd(PPh_3)(\mathbf{1})(\mathbf{4})]^-$.

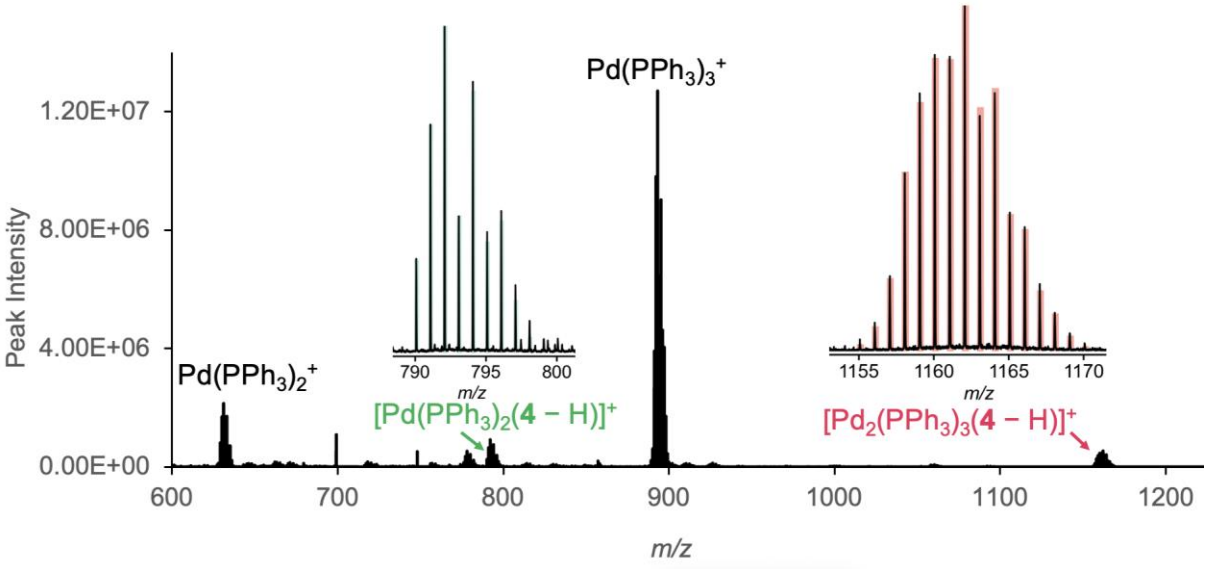

Figure 2.13. PSI-ESI-MS scan on poison: N-acetylcysteine added to $(PPh_3)_4$ in the positive ion mode showing two Pd-poisoned product peaks. The insets show the predicted isotope pattern (bars) overlaid on the experimental mass spectrum (lines).

This species has disappeared after two minutes and is completely subsumed by $[Pd(PPh_3)(\mathbf{1})(\mathbf{4}\text{-}2H)]^-$. What appears to happen is the initial coordination of **4** to Pd(0), followed by the loss of 2H and oxidation to Pd(II). We do not have insight into the mechanism of this transformation, but the coordination of **4** to Pd(0) suggests that the

transformation is mediated somehow by the palladium.

In the positive ion mode, we see corroborating evidence for the partial oxidation of Pd(0). We also see low levels of $[Pd^{II}(PPh_3)_2(\mathbf{4}\text{-}2H) + H]^+$ and trace levels of the dinuclear complex $[Pd_2^{I}(PPh_3)_3(\mathbf{4}\text{-}2H)+H]+$ (**Figure 2.14**), where we expect the deprotonated *N*-acetylcysteine ligand is bridging between the two Pd centers. As was observed in the negative ion mode with the charged tag (**1**), substantial Pd(0) species remain in the solution, even in the presence of excess *N*-acetylcysteine.

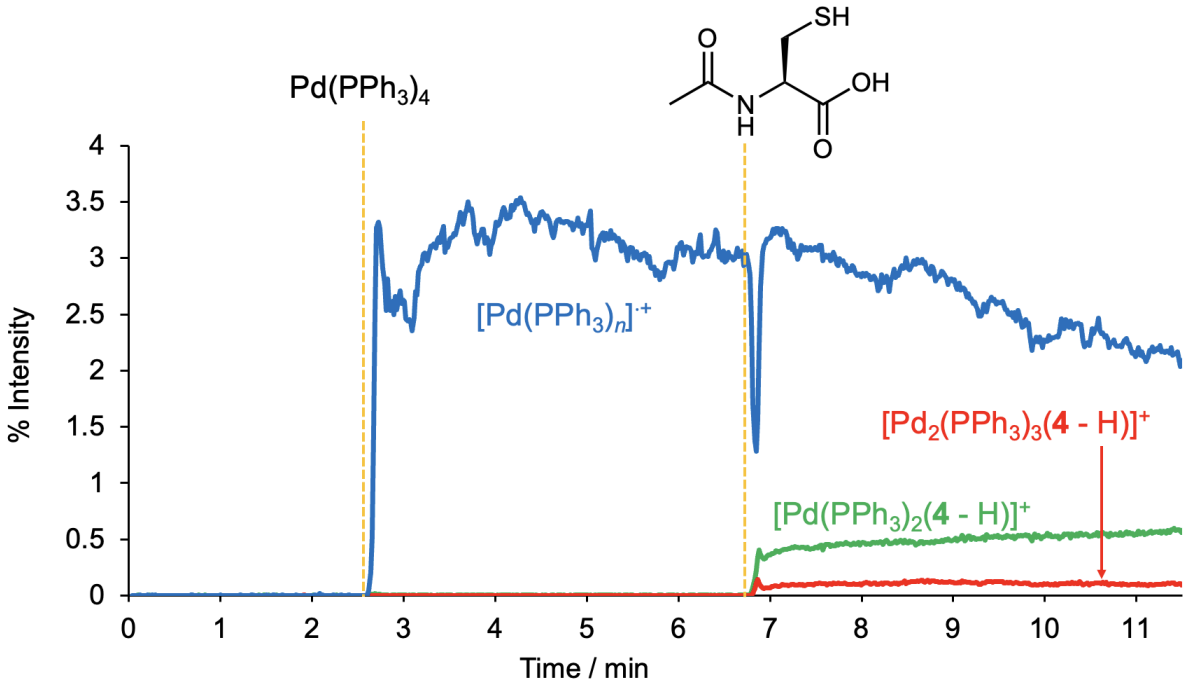

Figure 2.14. PSI-ESI-MS reaction monitoring in positive ion mode showing the effect of poison: *N*-acetylcysteine addition on catalyst activation. A drop in the relative abundance of $[Pd(PPh_3)_n]^{\cdot+}$, where n = 1-2, is observed upon the addition of the poison and the formation of Pd-poisoned products are shown in red and green color traces.

2.3.3.2 Poisoning of Pd(II)

Adding *N*-acetylcysteine to $[Pd(PPh_3)_n(\mathbf{1})(Ph)(I)]^-$ resulted in a large change in the apparent relative abundance of $[Pd(PPh_3)_n(\mathbf{1})(Ph)(I)]^-$ with respect to $[Pd(PPh_3)_n(\mathbf{1})]^-$ (**Figure 2.15**). Before addition, the solution was mostly the former; immediately afterwards, the situation was reversed before a slow return to an equilibrium position where both were of similar abundance. Our best guess was that the neutral cysteine displaces the iodide to form $Pd(PPh_3)(\mathbf{1})(Ph)(C_5H_9NO_3S)$, but this zwitterionic assignment was not backed up by examining the positive ion mode without the charged tag, where we did not see the corresponding cation $[Pd(PPh_3)_2(Ph)(\mathbf{4})]^+$ (**Figure A10** in appendix).

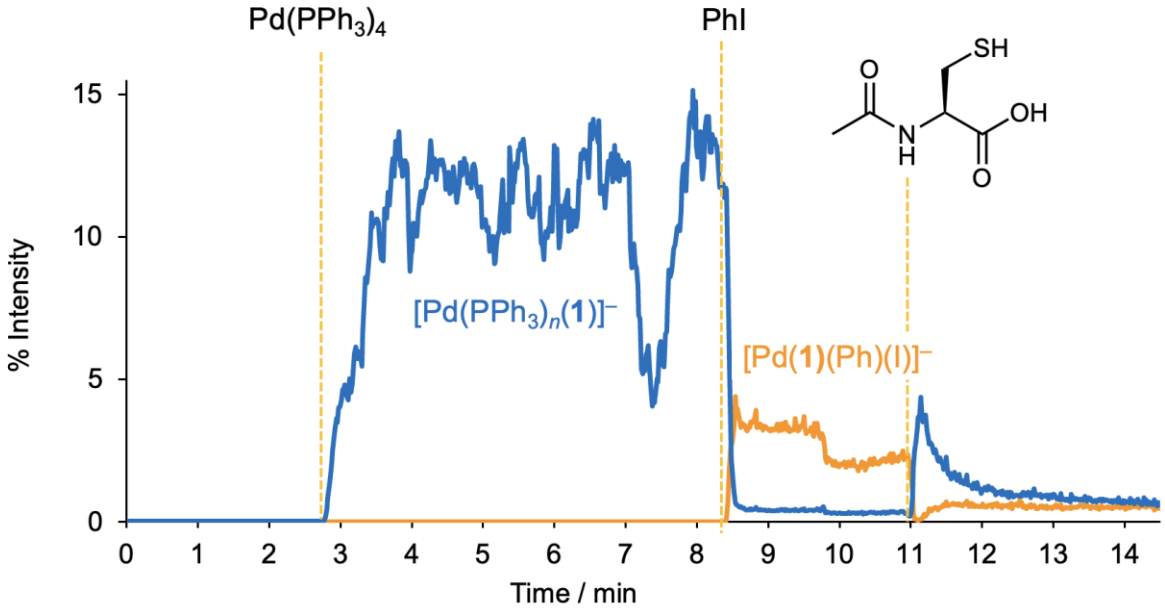

Figure 2.15. PSI-ESI-MS reaction monitoring in negative ion mode showing the effect of poison: *N*-acetylcysteine addition on oxidative addition. A drop in the relative abundance of $[Pd(PPh_3)_n(\mathbf{1})]^-$ (blue trace), where n = 1-2, is observed upon the addition of the aryl halide: PhI and the resulting oxidatively added product: $[Pd(\mathbf{1})(Ph)(I)]^-$ is disappeared. No indication for the Pd poisoned products upon the addition of the *N*-acetylcysteine.

2.4 Conclusions

Examination of the effect of a small collection of sulfur-containing molecules on a Pd(0) precatalyst and on the product of the initial step in most cross-coupling reactions, the Pd(II)(Ph)X oxidative addition product, revealed some consistent behavior as well as some significant differences. All three poisons reacted rapidly with Pd(0), all via the oxidation of the Pd(0) to Pd(II) and deprotonation of the poisons. Thiols are more often thought of as reducing agents, since they are readily oxidized through reaction with another thiol, which results in the formation of a disulfide and H_2. We think that this transformation is likely mediated by Pd(0), and the resulting disulfide can oxidatively add to Pd(0) to form Pd(II)$(SR)_2$.

2.5 Experimental

2.5.1 Materials and chemicals

All solvents were purchased from Fisher Scientific and used without further purification, unless otherwise specified. Tetrakis(triphenylphosphine)palladium(0) (99%), methanol (HPLC grade, freeze pump thawed), 1,2-benzenedithiol (96%), thiourea (99%), and *N*-acetylcysteine were purchased from Sigma Aldrich. Iodobenzene (PhI 98%) was purchased from Sigma-Aldrich and purified by washing 3 times with 10% HCl, followed by freeze-pump-thaw degassing. Gases were purchased from Airgas (Calgary, Canada) and used without further purification.

2.5.2 Synthesis of Bis(triphenylphosphine)iminium triphenylphosphine monosulfonate $[PPN]^+[P(Ph)_2(m\text{-}C_6H_4SO_3)]^-$: [PPN](1)

Bis(triphenylphosphine)iminium triphenylphosphine monosulfonate $[PPN]^+[P(Ph)_2(m\text{-}C_6H_4SO_3)]^-$, [PPN](**1**), was synthesized as reported previously.[94]

2.5.3 Preparation of stock solutions

All reagent stock solutions were prepared under an inert nitrogen atmosphere in a glovebox or on a Schlenk line. The tetrakis(triphenylphosphine)palladium(0) stock solution was prepared by dissolving 0.0116 g $Pd(PPh_3)_4$ into 5.0 mL of distilled THF (2.0 mM Pd). The charge-tagged phosphine (**1**) stock solution was prepared by dissolving 0.0088 g of [PPN][**1**] into 10.0 mL of degassed HPLC-grade methanol (1.0 mM). Iodobenzene stock solution was prepared by serial dilution into 10.0 mL of degassed HPLC-grade methanol (4.0 mM PhI). Poison:Pd ratio was maintained as 5:1 for all the experiments.

2.5.4 Instrument conditions and parameters

Mass spectra were collected by a Waters (Milford, USA) Synapt G2-Si mass spectrometer and analyzed using Waters MassLynx V4.2. The Synapt G2-Si was operated in the positive ion resolution mode and negative ion resolution mode separately. The capillary voltage was held at 2.5 kV, with the desolvation settings optimized with a source temperature of 80°C, desolvation temperature of 200°C, desolvation gas flow rate of 50 Lh^{-1}, and cone gas flow rate of 400 Lh^{-1}. The mass range was set to *m/z* 100-2000 with scan durations of 1 s.

2.5.5 Experimental procedures for PSI-ESI-MS reaction monitoring

The solvent and a charged ligand are added to a Schlenk flask equipped with a rubber septum. A length of PEEK chromatography tubing is passed through the septum into the solution, and the other end is attached to the atmospheric pressure source of an ESI-MS instrument (**Figure 2.16**). An overpressure of ~5 psi argon is applied to the flask, which drives the solution continuously into the MS in a process akin to a cannula transfer. The flow rate is of the order of 10 $uLmin^{-1}$, in the ideal range for conventional ESI-MS analysis. The signal of the charged ligand is allowed to stabilize before adding the precatalyst, $Pd(PPh_3)_4$. The charged monosulfonated triphenylphosphine ligand, $[PPh_2C_6H_4SO_3]^-$, $[\mathbf{1}]^-$, rapidly exchanges with the neutral PPh_3 ligand to "light up" the palladium(0) complexes as $[Pd(PPh_3)_n(\mathbf{1})]^-$ (n = 0-2). Note that we do this experiment with a negatively charged tag because in the positive ion mode, the ESI source oxidizes and will convert Pd(0) species into Pd(I), which complicates the analysis. Once the signal stabilizes as the mixture reaches equilibrium, an excess of the poison was added through the septum via a syringe. It was possible to observe in real time the changes in speciation that occur.

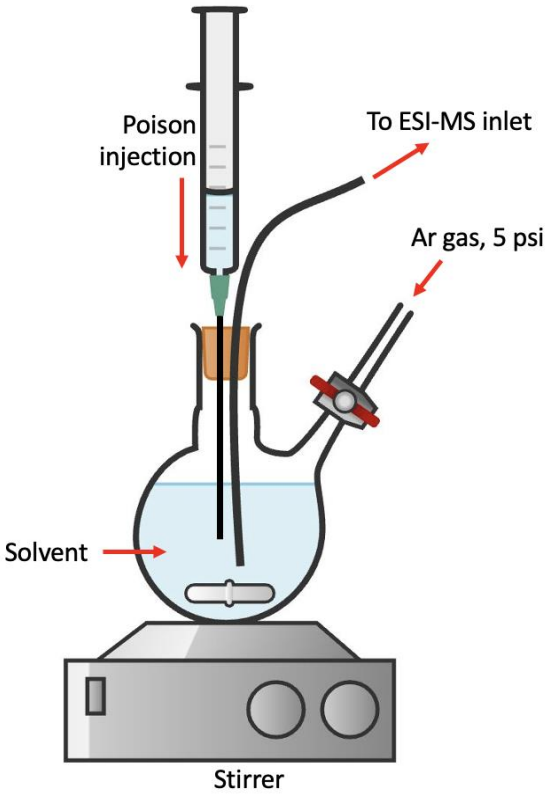

Figure 2.16. Experimental set-up for PSI-ESI-MS reaction monitoring for poisoning experiments.

Chapter 3

A one-experiment approach to calibration

Abstract

A novel one-experiment approach to the calibration of analytical instrumentation is introduced using UV-Vis spectroscopy and ESI-MS as a testing ground. The detailed experimental setup and the instrumental condition optimization for both analytical techniques are described. The analyte solution concentration was steadily increased over time using an automated syringe pump while continuously monitoring the intensity of the analyte, which resulted in the collection of numerous data points that can be converted into an intensity versus concentration plot using a custom Python script. The benefits of this method can be highlighted as providing a stable and reliable calibration state throughout the analysis, reducing the chances of data inconsistencies, and ensuring the calibration process is efficient and accurate. Compared to discrete calibration methods, the higher accuracy, precision and speed offered by this continuous calibration method make it a superior approach for achieving high-quality analytical results.

3.1 Research motivation

A significant challenge encountered during catalyst poisoning investigations was the quantification of species. Mass spectrometry quantification presented complexities due to the frequent occurrence of non-linear responses with increasing analyte concentrations. This non-linearity complicated the construction of accurate calibration curves necessary for converting MS intensity to concentration. To enhance the precision of catalyst poisoning quantification, it was deemed highly advantageous to

develop a rapid and data-rich calibration method. Consequently, the potential of continuously collecting calibration data utilizing an innovative technique was explored as a collaborative project with Dr. Peter Williams. Dr Williams did all of the programming; I collected all of the experimental data and used the program output to generate the fitted figures in this chapter.

3.2 Introduction

Calibration curves are fundamental tools in quantitative analysis, playing a crucial role across various scientific disciplines such as chemistry, biology, and materials science. These calibration curves are used routinely in analytical chemistry.[95] Calibration curves help to determine the accuracy and quality of measurements reported using an instrument. Since there is a tendency for the calibration to drift over time, maintaining the calibration of the instrument is an ongoing need in order for results to be reliable, confident, accurate, and reproducible.[96] Therefore, calibration is important to ensure the accuracy, minimize measurement uncertainty, and quantify and control errors to an acceptable level.

Calibration curves graphically represent the relationship between known concentrations of an analyte and the corresponding instrument response to give an accurate, reliable, and reproducible determination of an unknown sample concentration.[97] The construction of a calibration curve starts with the preparation of a series of standard solutions with known analyte concentrations, measuring instrument response, followed by the formal analysis, and finally plotting the calibration curve (**Figure 3.1**). Importantly, the concentration of unknown samples should lie within the range of the

calibration curve to enable the determination of the unknown's concentration.

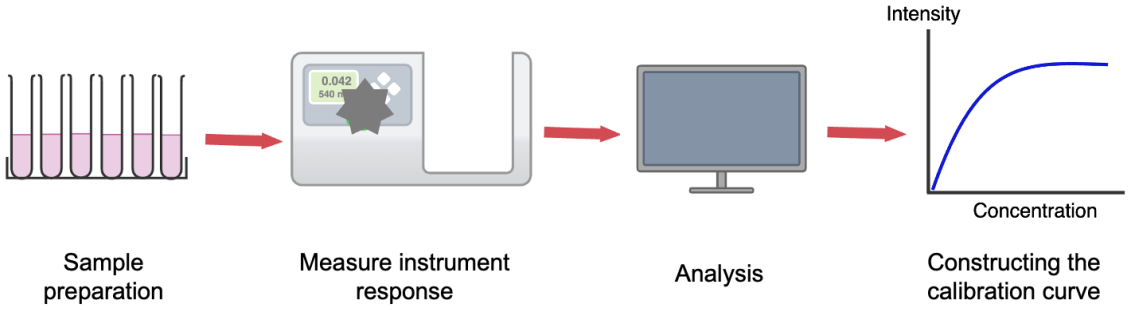

Figure 3.1. Standard experimental procedure for constructing a calibration curve.

Instrument response is measured for each standard solution under consistent and controlled conditions. Instrument responses can be absorbance in spectrophotometry, peak area in chromatography, signal intensity in mass spectrometry, etc. These responses are plotted against the known concentrations to create a graph, with concentration on the x-axis and response on the y-axis.[97] A suitable mathematical model is fitted to the data points to find out the functional relationship between concentration and response. More complex models and programming tools are used if the relationship is non-linear or if there is a combination of linear and non-linear regions. Calibration curves are useful for precise quantification of analyte concentrations in unknown samples by interpolating within the constructed calibration range. Calibration curves are essential for accurately measuring substances in routine laboratory analysis, in developing methods, and in checking quality.[98] They help with advancements in scientific research and technological innovations. Therefore, calibration curves are crucial for ensuring analytical results are reliable and precise in many different fields.

The linear region of a calibration curve is the portion of the calibration curve where the analyte concentration is directly proportional to the instrument response.[98] In this region, a straight line best describes the data points, indicating that changes in concentration result in proportional changes in response.[97] The calibration curve usually deviates from linearity after a certain concentration, and beyond this limit, the concentration is no longer proportional to the instrument response.[99] This is known as the 'limit of linearity'.[100] Basically, the limit of linearity marks the boundary between the linear region and the beginning of the plateauing area. The plateau is the region of the calibration curve where increases in analyte concentration no longer result in proportional increases in instrument response due to saturation of the detector. The straight line that best matches the data points is the linear fit. **Figure 3.2** shows a hypothetical graph of instrument response vs. concentration with the linear fit and limit of linearity.

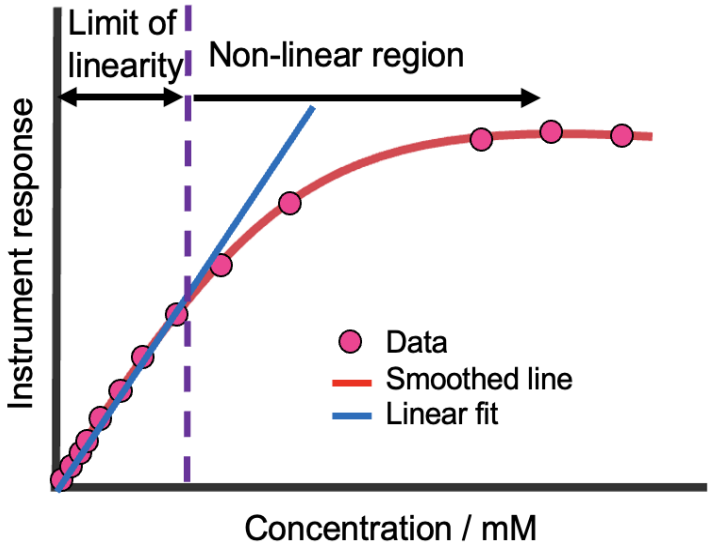

Figure 3.2. A standard graph of instrument response versus concentration showing the linear fit, limit of linearity and non-linear region.

Identifying the limit of linearity is crucial because it determines the highest concentration that can be accurately quantified using the linear calibration model.[101] By identifying the linear range, scientists can adjust sample preparation protocols and instrument settings to ensure that most samples fall within this range, thereby maximizing the accuracy of measurements.[102]

According to the literature, different calibration methodologies can be identified: direct (or absolute) calibration and indirect (or relative) calibration.[103] Indirect calibration is most widely used in chemical analysis[103] because the objective of the calibration is to construct a response curve from several known concentrations versus corresponding signal. There are other traditional approaches available according to the number of standards employed in the calibration (single-point calibration, double-point calibration, and multiple-point calibration) (**Figure 3.3**) and considering the different uses of the reference materials (external standard calibration-EC, matrix-matched calibration-MC, standard-added calibration-AC, etc.).[103]

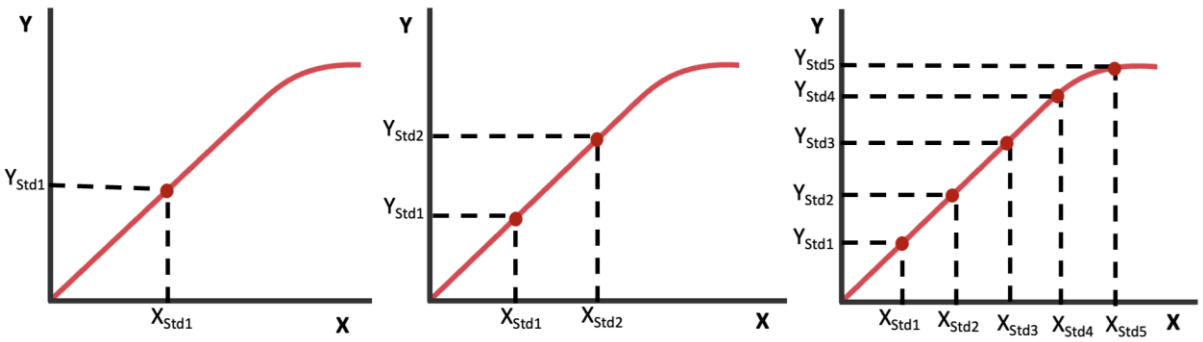

Figure 3.3. Types of calibration based on the number of standards employed. (a) Single-point calibration, (b) Double-point calibration and (c) Multiple-point calibration.

The main problems with these traditional discrete calibration methods are that the calibration standards are prepared and measured individually at specific time intervals, they do not capture the changes in instrumental response continuously, and the data points are produced separately so that the linearity of the calibration curve depends on the trendline of the individual data points.

Our group has recently had success with continuous addition as a means of simplifying the kinetic analysis of catalytic reactions.[104] We looked at other problems that could be improved by a similar approach, and decided that calibration was a good target. The traditional methods are time-consuming and hence avoided more than they should be, therefore, a more expedient, convenient method is desirable. The main idea is to ramp the concentration over time while monitoring the intensity of the analyte in real-time, which results in the collection of numerous data points continuously over a period of time. Because the process is easily automated, the collection of the many data points involves little more work than a single experiment: instead of adding the aliquot via syringe, a syringe pump is set up to introduce the aliquots to the flask.

3.3 Results and Discussion

3.3.1 UV-Vis spectroscopy

This technique was first applied to UV-Vis spectroscopy before being applied to other analytical methods. UV-Vis spectroscopy calibration is simple; it gives a linear response over a considerable concentration range; there is minimal interference from matrix effects; and the infrastructure is ubiquitous and inexpensive. UV/Vis analyses are a staple of undergraduate lab experiments, including experiments that demonstrate Beer's Law[105] (and the point at which it breaks down).[106]

3.3.1.1 Initial instrument test

I first performed an initial instrument test to find an appropriate concentration range of $KMnO_4$ to run UV-Vis calibration curves at the λ_{max}. The UV-Vis spectrum was obtained in this concentration range to ensure suitability, and optimal instrument parameters in UV-Vis such as, exposure 100, Boxcar 10, scans 10, path length 1 cm, wavelength range 420-610 nm were found to be appropriate. The optimal concentration was 0.008 M at a λ_{max} of 525 nm.

3.3.1.2 Optimal experimental conditions

To identify the optimal experimental conditions, different experiments were run by changing each and every parameter. Optimal experimental conditions were then determined according to the obtained results (stirring rate: 200 rpm, solvent: 5 mL H_2O, medium sized magnet, addition rate: 100 µL of 0.008 M $KMnO_4$ at 20 seconds intervals). The rate of diffusion in the system was tested using $KMnO_4$ as the analyte (**Figure 3.4**) and we found that the system responded to changes in concentration in less than 5 seconds (the time taken for a single scan).

All the intensity vs time graphs were obtained by integrating the maximum absorbance region of the corresponding calibrant.

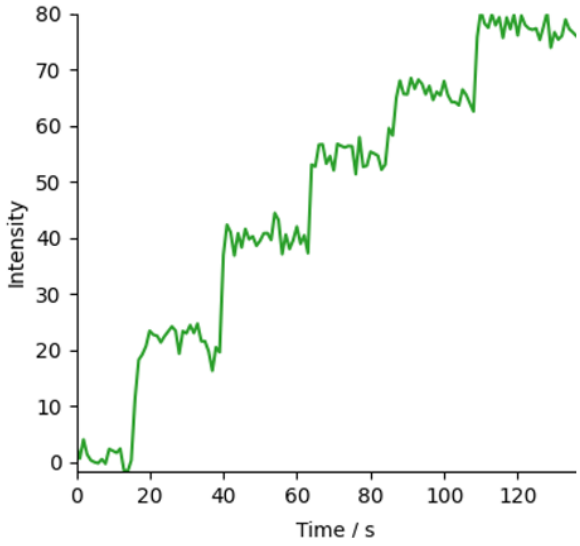

Figure 3.4. Intensity vs time graph for addition of 100 µL, 0.008 M $KMnO_4$ to 5 mL H_2O (solvent) at 20 second intervals to identify the diffusion rate.

3.3.1.3 Discrete calibration

A conventional calibration curve was plotted by making up 10 solutions of $KMnO_4$ at concentrations of 0.1 mM, 0.2 mM, 0.3 mM, 0.4 mM, 0.5 mM, 0.6 mM, 0.8 mM, 1 mM, 1.2 mM and 1.4 mM and measuring the absorbances (triplicated) individually (**Figure 3.5**).

The graph of intensity versus concentration displayed a linear response up to a concentration of approximately 0.3 mM. Even though this discrete calibration method is a less complex setup and involves fewer data points, making the analysis easier, there are various disadvantages in this method compared to the continuous calibration

method. For instance, this method is less accurate and can lead to interpolation errors when the system exhibits non-linear behavior between discrete points (for example, according to Figure 3.5, it shows non-linear behavior above 0.3 mM concentration).

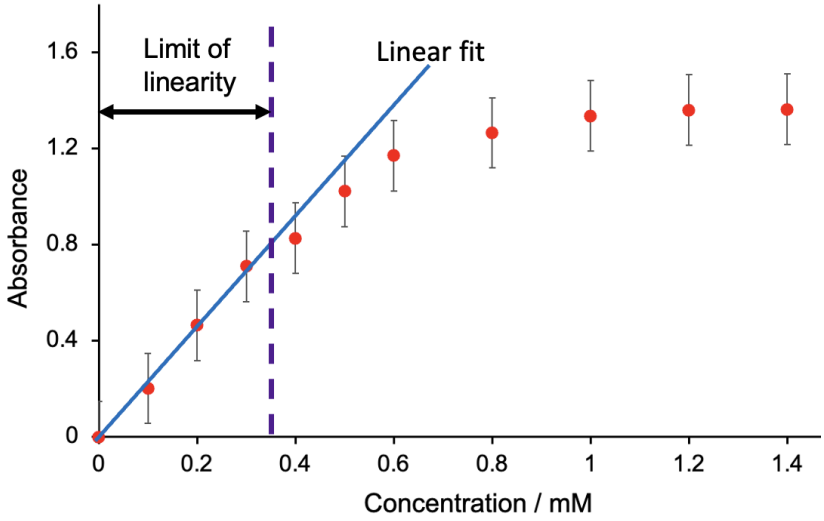

Figure 3.5. The absorbance versus concentration graph for 10 different concentrations obtained using UV-Vis spectroscopy.

3.3.1.4 Semi-continuous calibration

A second experiment was performed where the addition of 50 µL aliquots of 0.008 M $KMnO_4$ to 5mL H_2O (solvent) at 1-minute time intervals for 20 minutes (**Figure 3.6**). This approach is considered a semi-continuous calibration method. **Figure 3.6 (a)** shows the original data for intensity versus time graph and **Figure 3.6 (b)** demonstrates the intensity versus concentration graph.

This experiment was conducted to demonstrate that our curve-fitting approach can be used even if a syringe pump for continuous infusion is not available. It duplicates the sort of results that might be obtained if someone performed the additions manually or with a liquid-handling robot.

According to results obtained for this semi-continuous calibration, the limit of linearity is 0.3 mM concentration, which suggests that the results for both discrete calibration and this semi-continuous calibration are align with each other.

This shows a way of collecting a discrete calibration much more rapidly and using the program to calculate and fit a curve. The other uses are to demonstrate fast diffusion and have additional concentration versus absorbance values to demonstrate that continuous flow is reliable. Compared to the above-mentioned discrete calibration method, this semi-continuous method offers a balance between accuracy and complexity, but it generates less data compared to continuous calibration and is likely to be more time-consuming to conduct.

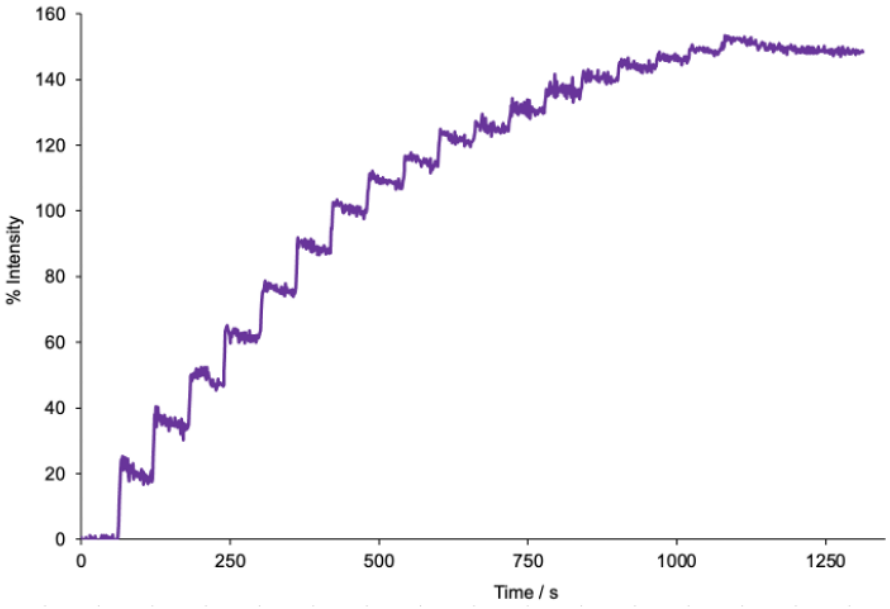

(a)

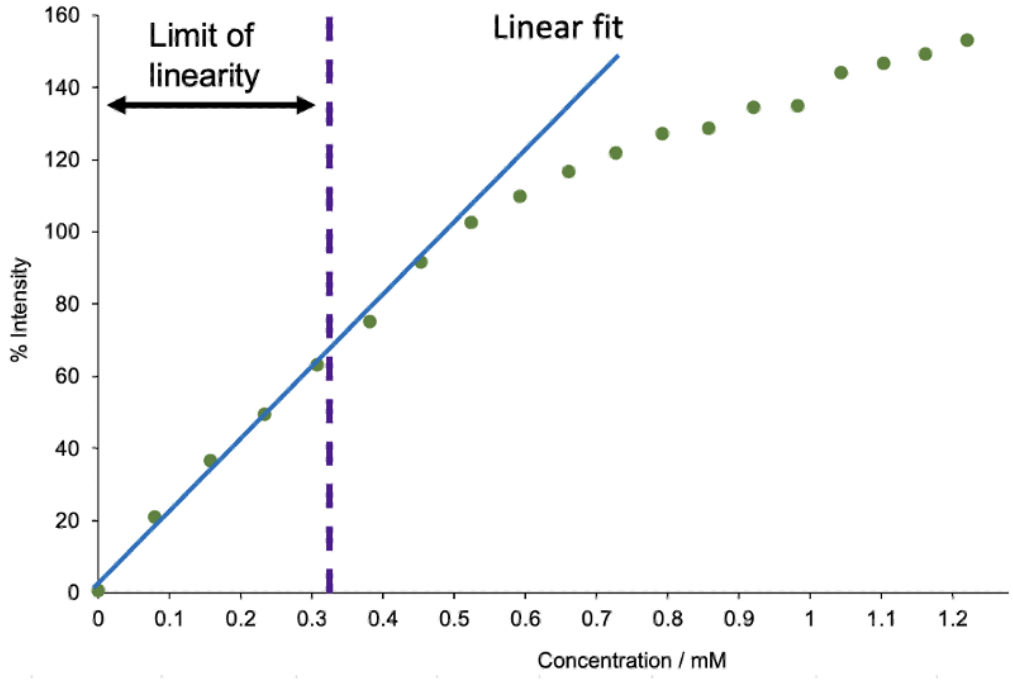

(b)

Figure 3.6. The top figure **(a)** shows the intensity versus time graph for addition of 50 µL aliquots of 0.008 M $KMnO_4$ to 5 mL H_2O (solvent) at 1-min time intervals, and the bottom figure **(a)** shows the corresponding intensity versus concentration graph.

3.3.1.5 Continuous calibration

Finally, we conducted continuous experiments, where the calibrant solution was infused at 50 uL/min via a syringe pump. Experiments were performed over a period of 20 minutes, to ensure the collection of plenty of data points. The composite figure below (**Figure 3.7**) shows the original intensity versus time data for the triplicates.

The corresponding extrapolated and fitted data with the UV-Vis setup is shown in **Figure 3.8.** The curve of intensity versus time (**Figure 3.8 a**) illustrates a clear, visual representation of trend over time, and the curve is initially linear before starting to curve as the instrument saturates. More importantly, this graph demonstrates a smoother presentation of data and high accuracy over discrete calibration methods. The corresponding extrapolated graph (**Figure 3.8 c**) was used to identify the linear region. Concentrations below 0.34 mM were fitted into the linear region, and linearity decreased after that point.

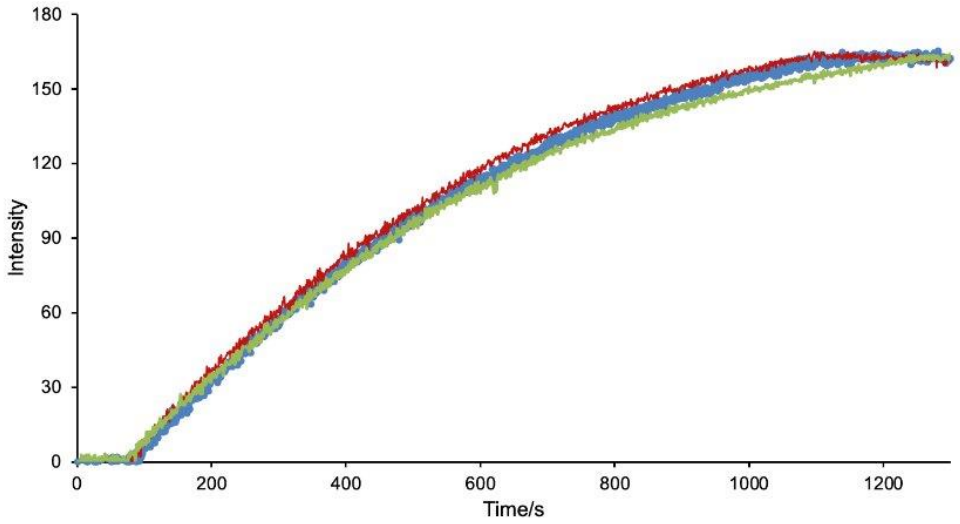

Figure 3.7. Intensity vs. time graphs for original data (Triplicated - continuous addition of 1.0 mL of standard 0.008 M $KMnO_4$ solution to the solvent: 5 mL H_2O with the addition rate of 50 µL/min).

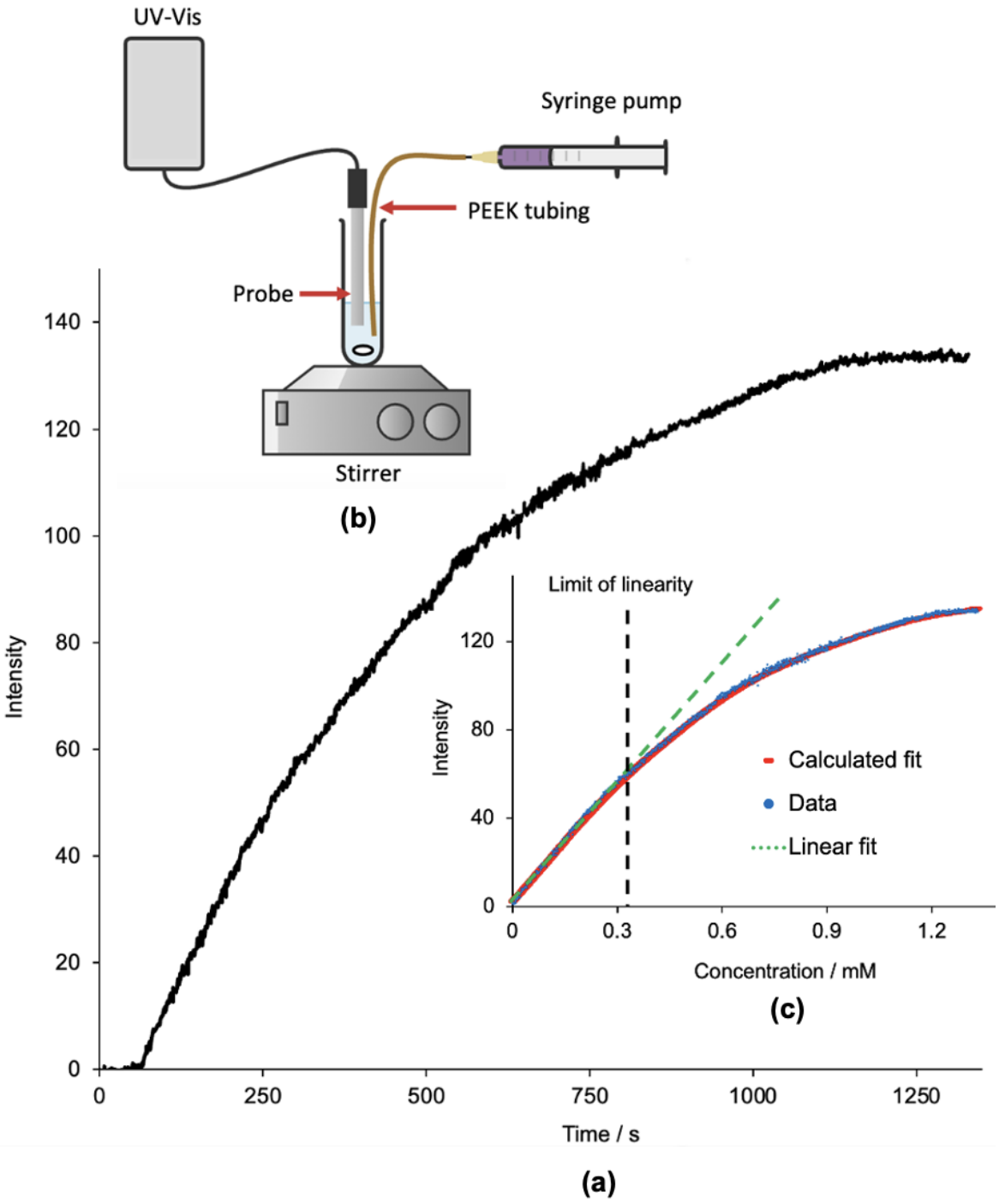

Figure 3.8. Intensity vs. time graph (**a**) for original data for one of the triplicates (continuous addition of 1.0 mL of standard 0.008 M $KMnO_4$ solution to the solvent: 5 mL H_2O with the addition rate of 50 µL/min). Top inset (**b**) shows the UV-Vis spectroscopy experimental set up for continuous addition of calibrant and bottom inset (**c**) shows the Intensity vs. concentration graph for smoothed and fitted data, complete with limit of linearity.

These results suggest that interpolation is easier and more precise than the discrete calibration technique because this method allows more precise estimations of intensity at specific time points. This is particularly useful in real-time monitoring of data. Finding the limit of linearity is important because it defines the validity of calibration, which is the range that gives direct proportionality between the instrument response and the analyte intensity, and the quantitative accuracy. The linear range has a consistent and predictable relationship between analyte intensity and concentration.

3.3.6 Assessing the cost-benefit of the continuous calibration analysis

The advantages of continuous calibration arise not so much via the total time of analysis, because at least for UV/Vis spectroscopy, individual measurements can be made quickly and easily. The advantages are centered around the great increase in the number of data points taken (often hundreds rather than just a handful), which provides more convincing data and a better estimate of the saturation limit. It also saves a lot of time in terms of making up standard solutions: continuous calibration requires the preparation of a single solution rather than as many as the number of data points required for individual analyses. Because the analysis is automated, we also expect that process to be accelerated as the operator can simply feed in the raw data accompanied by three numbers: the starting solvent volume, the concentration of the calibrant solution, and the rate of addition of the calibrant solution. The program will rapidly provide all the relevant metrics in response. Based on the success of this initial investigation, I proceeded to try different analytical techniques, starting with ESI-MS.

3.3.2 Mass Spectrometry

Continuous calibration in MS was performed, covering both linear and non-linear quantitative calibration ranges. Tetra-*n*-hexylammonium chloride $[N(n\text{-}C_6H_{13})_4]Cl$ in 1:1 MeCN:H_2O was used as the calibrant for MS analysis. This calibrant was added to 20 mL of the starting solvent (1:1 MeCN:H_2O, where MeCN = acetonitrile) at the outflow rate (to the spectrometer) of 20 uLmin-1 to achieve a good homogenous solution. The experiments were repeated by diluting the tetrahexyl ammonium chloride stock solution to get a good calibration curve. **Figure 3.9** shows the intensity vs. time graph for original data (continuous addition of 6.25 µM $[N(n\text{-}C_6H_{13})_4]Cl$ solution to the solvent: 20 mL with the addition rate of 20 $\mu Lmin^{-1}$) with converted intensity vs. concentration graph and MS experimental set up. The $[N(n\text{-}C_6H_{13})_4]^+$ ion was observed in the positive ion mode.

The intensity versus time graph (Figure 3.8a) shows that the curve is initially linear before starting to curve as the instrument saturates. The intensity vs. concentration graph (Figure 3.8c) was used to identify the linear region. The results show that the linear region is limited to below 0.183 µM concentration of $[N(n\text{-}C_6H_{13})_4]Cl$.

According to the results of this continuous calibration in MS, it demonstrates that this method offers numerous benefits that significantly enhance the accuracy, precision, and reliability of analytical measurements. More apparently, continuous calibration ensures the mass spectrometer remains accurately calibrated throughout the analysis, thereby minimizing interpolation errors and leading to precise measurements.

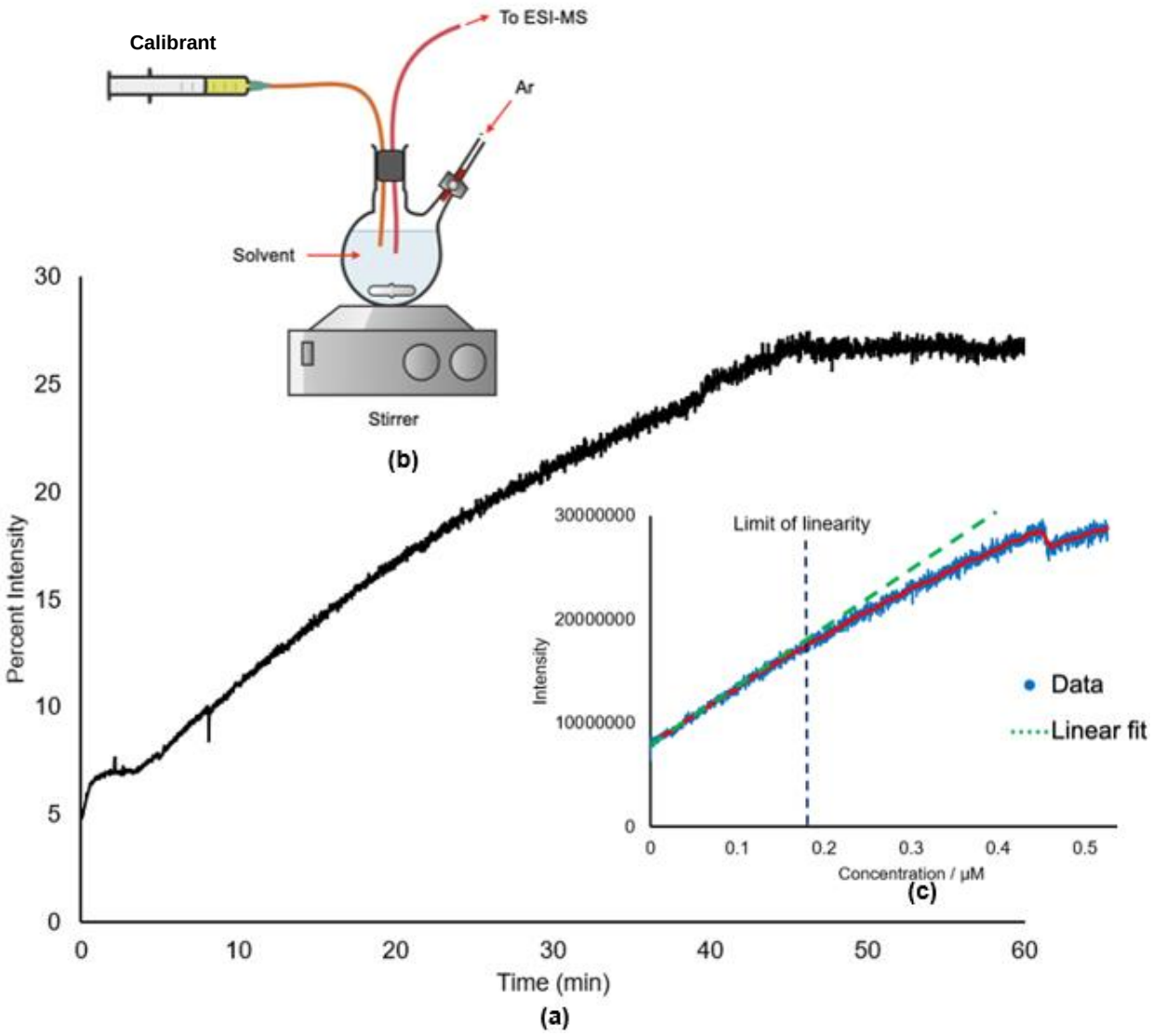

Figure 3.9. Intensity versus time graph (a) for original data (continuous addition of 12.5 µM $[N(n\text{-}C_6H_{13})_4]Cl$ solution to the solvent: 20 mL with the addition rate of 20 µL/min). Top inset (b) shows the MS experimental set up for continuous addition of calibrant and bottom inset (c) shows the intensity versus concentration graph for complete with limit of linearity.

This can be used to make real-time adjustments in MS for any changes or drifts, which makes the measurements more sensitive and precise. Furthermore, this method provides more reliable data, ensuring consistent calibration throughout the entire analysis, which leads to better quantification of the analyte. Continuous calibration in MS which is facilitated by the program and the webtool, increases the overall efficiency by minimizing the need for manual recalibration, and automation of the analyte addition reduces the probable human errors compared to the manual addition.

3.3.3 Attenuated Total Reflectance (ATR)

The success of these two experiments meant that I reached out to the Hore group, a spectroscopy research team here at the University of Victoria. They have constructed an ATR experimental setup that is compatible with continuous calibration, so they will be contributing to the final manuscript with infrared spectroscopic data.

3.4 Conclusions

A one-experiment approach to continuous calibration was applied to both UV-Vis and MS, along with traditional discrete calibration methods, for comparison. This one-experiment approach offers numerous advantages that significantly improve the quality and speed of analytical measurements. Continuous calibration provides a stable and reliable calibration state in UV-Vis spectroscopy. This stability reduces the possible errors and the chances of data inconsistencies compared to discrete methods, because most of the time, discrete calibration depends only on a few data points (typically about 5) in constructing calibration curves. Therefore, the measurements obtained from continuous calibration are more accurate and reliable compared to discrete calibration methods. Automation of the calibration process with a simple syringe pump saves time

as well as reduces the potential human errors, ensuring that the calibration process is both efficient and accurate. In mass spectrometry, continuous calibration ensures that the instrument remains accurately calibrated throughout the entire analysis. This capability minimizes interpolation errors, leading to more precise measurements. More importantly, continuous calibration significantly improves the reliability and accuracy of the data in quantitative analysis compared to discrete calibration, because continuous calibration covers the entire range of calibration more thoroughly than discrete calibration methods. By providing a smoother presentation of data in terms of 'calculated fit' which is facilitated by the webtool and the program, continuous calibration makes it easier to interpret and analyze results. This calculated fit presentation is especially important in complex analysis where small deviations can significantly impact the final outcome, as well as it reduces the need for manual recalibration. Overall, the higher accuracy and precision offered by a one-experiment approach: continuous calibration make it a superior approach for achieving high-quality analytical results in both mass spectrometry and UV-Vis spectroscopy.

3.5 Experimental

3.5.1 Materials and chemicals

All solvents were purchased from Fisher Scientific and used without further purification, unless otherwise specified. Tetra-*n*-hexylammonium chloride [N(n-$C_6H_{13})_4$]Cl (96%), Acetonitrile (99%), Potassium permanganate ($KMnO_4$) (99%) were purchased from Sigma-Aldrich. Gasses were purchased from Airgas (Calgary, Canada) and used without further purification. The stock solutions of $KMnO_4$ (0.008 M) and [N(n-$C_6H_{13})_4$]Cl (0.05 mM) were prepared initially.

3.5.2 UV/Vis instrumental setup and experimental conditions

The UV-Vis instrumental conditions were set up to: exposure 100, Boxcar 10, scans 10, path length 1 cm, wavelength range 420 - 610 nm, λ_{max} 525 nm. The standard 0.008 M $KMnO_4$ was added to the test tube containing 5 mL distilled water after 1 min of the starting of the data collection. Rate of addition was 20 µL/min for 20 minutes (using a syringe pump). Experimental conditions: stirring rate 200 rpm, solvent 5mL H_2O, magnet size - medium size).

3.5.3 MS instrumental setup and experimental conditions

Mass spectra were collected by a Waters (Milford, USA) Synapt G2-Si mass spectrometer and analyzed using Waters MassLynx V4.2. The Synapt G2-Si was operated in positive ion resolution mode. The capillary voltage was held at 2.5 kV, with the desolvation settings optimized with source temperature 80 °C, desolvation temperature 250 °C, desolvation gas flow rate 200 Lh^{-1} , and cone gas flow 50 Lh^{-1} . The mass range was set to *m/z* 250 - 450 with scan durations of 1 s. Intensity vs. time graph was collected for the continuous addition of 12.5 µM [N(n-$C_6H_{13})_4$]Cl solution

to the solvent (20 mL) in the PSI flask with the addition rate of 20 µL/min using a syringe pump. Ar gas flow (around 5 psi) was flushed through the PSI flask to facilitate the continuous injection of the analyte to the MS. The infusion of the analyte [N(n-$C_6H_{13})_4$]Cl was started at 2 minutes and infusion was stopped at 42 minutes allowing continuous infusion for 40 minutes.

3.5.4 Program and web application – Dr. Peter Williams

The Continuous Calibration method is facilitated by a program and web application. Data acquired during Continuous Calibration is entered into the program or web application, then calculated the analyte concentration for each data point, taking into account volume change; estimated a smoothed curved fit line using appropriate algorithms; estimated a linear fit region and a corresponding limit of linearity using appropriate algorithms; calculated relevant statistical tests, such as residuals; create figures, including analyte concentration vs. intensity and relevant statistical tests; and output key values and data. The code can estimate analyte concentrations based on intensity in non-calibration samples. This allows users to accurately convert instrument intensities into analyte concentrations.

Chapter 4

Future Work

The two projects in this thesis have highlighted the versatility of PSI-ESI-MS in studying the poisoning of homogeneous catalysts as well as in constructing calibration curves. Even though many potential poisons exists, we started with a subset of molecules used intentionally as poisons: a small selection containing sulfur donors, 1,2-benzenedithiol, thiourea, and *N*-acetylcysteine. Future experimental design can be catered to expand the fundamental understanding of catalyst poisoning using different classes of poisons, such as O-based, P-based, and N-based poisons. The main reason for using these different classes of poisons is, these different poisons have varying affinity for Pd complexes and, by studying different poisons we can select the most suitable poison which can target specific catalytic sites to allow more control over catalyst deactivation. Additionally, understanding the variation in the efficacy of different poisons may allow targeted purification procedures for solvents and reactants (e.g, emphasizing the removal of certain classes of a compound). Further, different poisons may require different strategies; therefore, investigating diverse sets of poisons can provide more comprehensive understanding, and chemists can use that knowledge to select and/or avoid particular poisons.

Multidentate ligands would be more effective when choosing poisons for study because they can offer several advantages when binding to a Pd metal center, such as versatility, stability, and control in a homogeneous catalysis. They provide increased stability compared to monodentate ligands and thereby, resistance to degradation and decomposition during the reaction. Multidentate ligands can also give the steric effect

in which some reaction pathways can be selectively blocked and hence, promote the poisoning of catalysts. The coordination environment can also be controlled by introducing multidentate ligands to the system. Furthermore, they provide multiple anchoring points for the metal center to bind, which allows for a more efficient and selective binding to the Pd metal center. **Figure 4.1** shows some of the potential O-based, P-based, and N-based poisons for future studies.

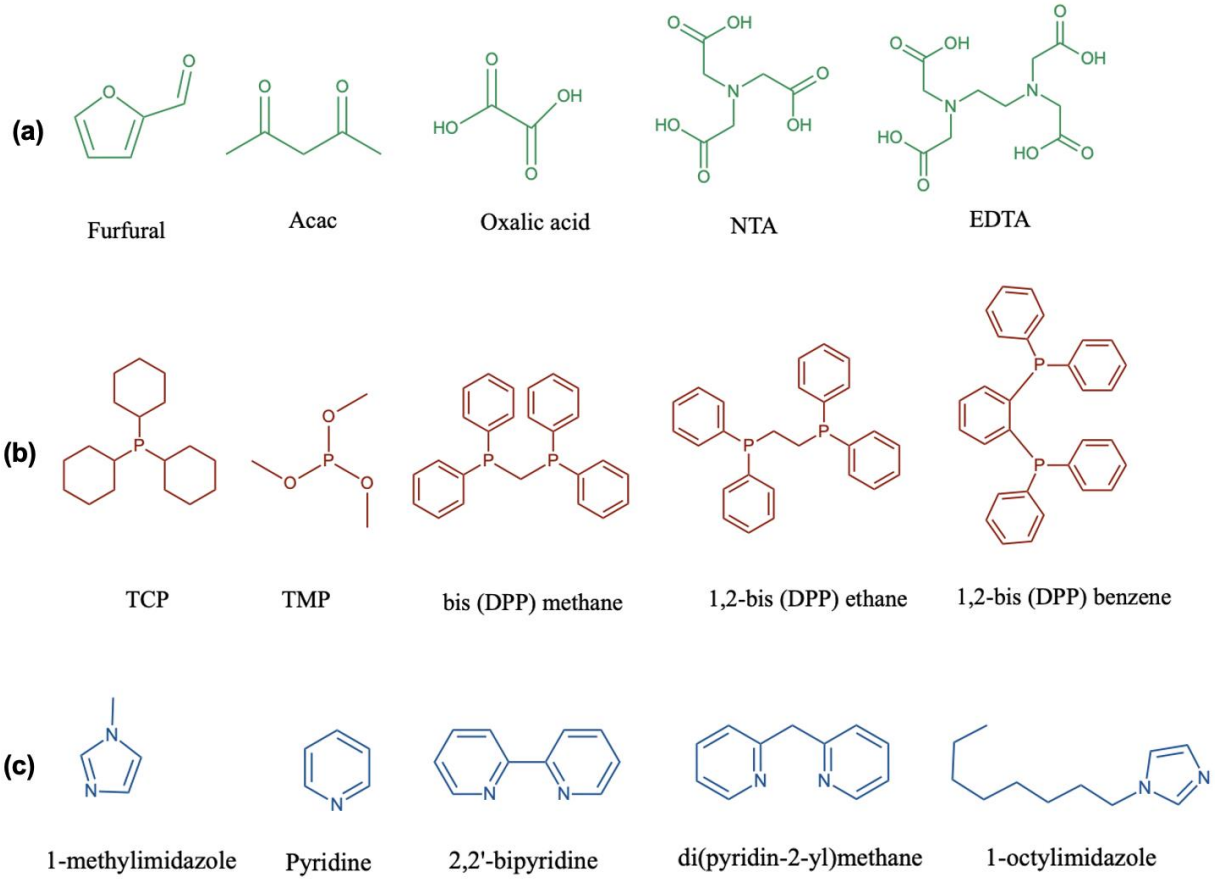

Figure 4.1. Some of the proposed **(a)** O-based, **(b)** P-based and **(c)** N-based poisons for future studies.

Multidentate ligands can chelate to the metal center, in a way that the ligand wraps around the metal atom to form a ring-like chelate structure. For example, 1,2-benzenedithiol (**2**) poison formed $[Pd(PPh_3)(\mathbf{1})(\mathbf{2}\text{-}2H)]^-$ and $[Pd_2(PPh_3)(\mathbf{1})(\mathbf{2}\text{-}2H)_2]^-$ complexes with Pd(0). These metal-chelate structures increase the rigidity of the metal-ligand complex and lead to the formation of strong Pd-poisoned species.
Real-time analysis of the poisoning effect on Pd catalyzed cross-coupling can be investigated for the aforementioned poisons.

In terms of quantitative analysis, the kinetic behavior of the poisons on Pd-catalyzed cross-coupling reactions can be investigated. Understanding the kinetics of catalyst poisons is important in designing a quenching strategy that halts a catalyst activity at a specific stage/time to prevent the further formation of products. It is equally important in the optimization of reaction conditions because reaction kinetics, such as reaction rates and equilibrium constants, allow a better understanding of how different poisons affect reaction rates. Therefore, kinetic studies can be investigated on catalyst poisons by facilitating the combined auto-sampling device and ^{1}H NMR.

One application of poisons is already under investigation. A cost-effective 3D printed auto-sampling device can be combined with ^{1}H NMR analysis to quantify the products in the reaction quantitatively. ^{1}H NMR spectroscopy provides insights into reaction mechanisms and reaction kinetics. Kinetic modeling should be combined with mathematical tools based on reaction mechanisms to describe the results. This aim can be achieved by comparing experimental data with predictions from kinetic models. The main focus here is to halt the reaction completely and immediately in order to run ^{1}H NMR. In this approach, the Pd(0) catalyst will be continuously introduced to the

reaction flask containing the charged ligand using the CAKE protocol.[101] Throughout the total reaction time, the exact amount of (1.0 mL) aliquots will be sequentially withdrawn from the flask and loaded to the vials containing the poisons using the autosampler at regular time intervals (**Figure 4.2**).

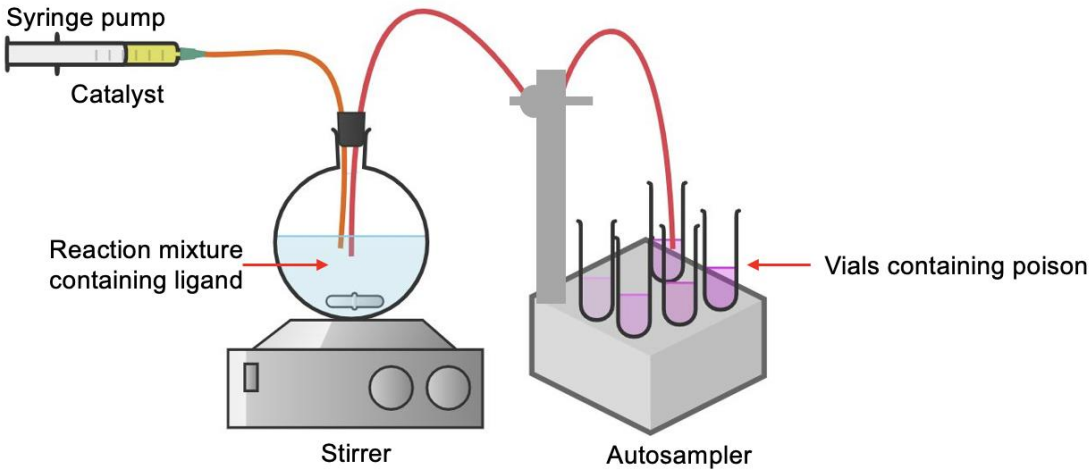

Figure 4.2. Experimental set-up for poisoning reactions analyzed by ^{1}H NMR.

The main concern in ^{1}H NMR study is selecting a suitable system with a ligand, internal standard, and poison that do not produce overlapping signals in the same range. Note that all the reactions will be performed according to the stoichiometric ratios. Since homogeneous poisons are used, variability between samples will be minimized. ^{1}H NMR data will be collected for the products, essentially the quantifications will be done by integrating the ^{1}H NMR signals corresponding to the product peaks.

These proposed studies will give molecular insight to the field of the poisoning of homogeneous catalysts as well as in-depth understanding of the kinetic profile of the studies. Further, the poisoning of homogeneous catalysts will be beneficial in

environmental science to understand the contaminants and their interaction with catalysts, catalysis research to explore the mechanism of catalytic reactions, and to understand the kinetic behavior of catalyst poisons.

References

(1) Andris, S.; Rüdt, M.; Rogalla, J.; Wendeler, M.; Hubbuch, J. Monitoring of Antibody-Drug Conjugation Reactions with UV/Vis Spectroscopy. J. Biotechnol. 2018, 288, 15–22.

(2) Antonov, L. Absorption UV-Vis Spectroscopy and Chemometrics: From Qualitative Conclusions to Quantitative Analysis. In Tautomerism: Methods and Theories; 2014; pp 25–48.

(3) Ben-Tal, Y.; Boaler, P. J.; Dale, H. J. A.; Dooley, R. E.; Fohn, N. A.; Gao, Y.; García-Domínguez, A.; Grant, K. M.; Hall, A. M. R.; Hayes, H. L. D.; Kucharski, M. M.; Wei, R.; Lloyd-Jones, G. C. Mechanistic Analysis by NMR Spectroscopy: A Users Guide. Prog. Nucl. Magn. Reson. Spectrosc. 2022, 129, 28–106.

(4) Massie, D. R.; Delwiche, S. R. Upgrading a High Performance Spectrophotometer. J. Infrared Spectrosc. 1996, 4 (1), 39–46. https://doi.org/10.1255/jnirs.74.

(5) Dutta, A. Chapter 4 - Fourier Transform Infrared Spectroscopy. In Spectroscopic Methods for Nanomaterials Characterization; Thomas, S., Thomas, R., Zachariah, A. K., Mishra, R. K., Eds.; Micro and Nano Technologies; Elsevier, 2017; pp 73–93. https://doi.org/10.1016/B978-0-323-46140-5.00004-2.

(6) Xu, L.; Schlup, J. R. Application of Near-Infrared Attenuated Total Reflectance Spectroscopy for Monitoring Epoxy Resin/Amine Cure Reactions. Appl. Spectrosc. 1996, 50 (1), 109–114. https://doi.org/10.1366/0003702963906654.

(7) Poole, C. F. Thin-Layer Chromatography: Challenges and Opportunities. J. Chromatogr. A 2003, 1000 (1), 963–984. https://doi.org/10.1016/S0021-9673(03)00435-7.

(8) Stroka, J.; Spangenberg, B.; Anklam, E. New Approaches in Tlc-Densitometry. J. Liq. Chromatogr. Relat. Technol. 2002, 25 (10–11), 1497–1513. https://doi.org/10.1081/JLC-120005700.

(9) Christensen, M.; Adedeji, F.; Grosser, S.; Zawatzky, K.; Ji, Y.; Liu, J.; Jurica, J. A.; Naber, J. R.; Hein, J. E. Development of an Automated Kinetic Profiling System with Online HPLC for Reaction Optimization. React. Chem. Eng. 2019, 4 (9), 1555–1558. https://doi.org/10.1039/C9RE00086K.

(10) Svensson, O.; Josefson, M.; Langkilde, F. W. Reaction Monitoring Using Raman Spectroscopy and Chemometrics. Chemom. Intell. Lab. Syst. 1999, 49 (1), 49–66. https://doi.org/10.1016/S0169-7439(99)00025-8.

(11) Fukuda, T.; Funaki, N.; Kurabayashi, T.; Suzuki, M.; Yoon, D. H.; Nakahara, A.; Sekiguchi, T.; Shoji, S. Real-Time Monitoring of Chemical Reaction in Microdroplet Using Fluorescence Spectroscopy. Sens. Actuators B Chem. 2014, 203, 536–542. https://doi.org/10.1016/j.snb.2014.06.045.

(12) Sadik, O. A.; Van Emon, J. M. Applications of Electrochemical Immunosensors to Environmental Monitoring. Biosens. Bioelectron. 1996, 11 (8), i–x. https://doi.org/10.1016/0956-5663(96)85936-7.

(13) Gross, J. H. Mass Spectrometry; Springer International Publishing: Cham, 2017. https://doi.org/10.1007/978-3-319-54398-7.

(14) Dempster, A. J. A New Method of Positive Ray Analysis. Phys. Rev. 1918, 11 (4), 316–325. https://doi.org/10.1103/PhysRev.11.316.

(15) Field, F. H. Chemical Ionization Mass Spectrometry. Acc. Chem. Res. 1968, 1 (2), 42–49. https://doi.org/10.1021/ar50002a002.

(16) Gross, J. H. Field Ionization and Field Desorption. In Mass Spectrometry: A Textbook; Gross, J. H., Ed.; Springer: Berlin, Heidelberg, 2004; pp 355–380. https://doi.org/10.1007/3-540-36756-X_8.

(17) Carroll, D. I.; Dzidic, I.; Stillwell, R. N.; Horning, M. G.; Horning, E. C. Subpicogram Detection System for Gas Phase Analysis Based upon Atmospheric Pressure Ionization (API) Mass Spectrometry. Anal. Chem. 1974, 46 (6), 706–710. https://doi.org/10.1021/ac60342a009.

(18) Ho, C. S.; Lam, C. W. K.; Chan, M. H. M.; Cheung, R. C. K.; Law, L. K.; Lit, L. C. W.; Ng, K. F.; Suen, M. W. M.; Tai, H. L. Electrospray Ionisation Mass Spectrometry: Principles and Clinical Applications. Clin. Biochem. Rev. 2003, 24 (1), 3–12.

(19) Hillenkamp, F.; Karas, M.; Beavis, R. C.; Chait, B. T. Matrix-Assisted Laser Desorption/Ionization Mass Spectrometry of Biopolymers. Anal. Chem. 1991, 63 (24), 1193A-1203A. https://doi.org/10.1021/ac00024a716.

(20) Woods, A. S.; Buchsbaum, J. C.; Worrall, T. A.; Berg, J. M.; Cotter, R. J. Matrix-Assisted Laser Desorption/Ionization of Noncovalently Bound Compounds. Anal. Chem. 1995, 67 (24), 4462–4465. https://doi.org/10.1021/ac00120a005.

(21) Avila, C. C.; Almeida, F. G.; Palmisano, G. Direct Identification of Trypanosomatids by Matrix-Assisted Laser Desorption Ionization–Time of Flight Mass Spectrometry (DIT MALDI-TOF MS). J. Mass Spectrom. 2016, 51 (8), 549–557. https://doi.org/10.1002/jms.3763.

(22) Characterization of polydisperse synthetic polymers by size-exclusion chromatography/matrix-assisted laser desorption/ionization time-of-flight mass spectrometry - Nielen - 1997 - Rapid Communications in Mass Spectrometry - Wiley Online Library. (SICI) 1097-0231(199707).

(23) Eelman, M. D.; Blacquiere, J. M.; Moriarty, M. M.; Fogg, D. E. Shining New Light on an Old Problem: Retooling MALDI Mass Spectrometry for Organotransition-Metal Catalysis. Angew. Chem. Int. Ed. 2008, 47 (2), 303–306. https://doi.org/10.1002/anie.200704489.

(24) Dole, M.; Mack, L. L.; Hines, R. L.; Mobley, R. C.; Ferguson, L. D.; Alice, M. B. Molecular Beams of Macroions. J. Chem. Phys. 1968, 49 (5), 2240–2249. https://doi.org/10.1063/1.1670391.

(25) Fenn, J. B.; Mann, M.; Meng, C. K.; Wong, S. F.; Whitehouse, C. M. Electrospray Ionization for Mass Spectrometry of Large Biomolecules. Science 1989, 246 (4926), 64–71. https://doi.org/10.1126/science.2675315.

(26) Vikse, K. L.; Scott McIndoe, J. Ionization Methods for the Mass Spectrometry of Organometallic Compounds. J. Mass Spectrom. 2018, 53 (10), 1026–1034. https://doi.org/10.1002/jms.4286.

(27) Theron, R.; Wu, Y.; Yunker, L. P. E.; Hesketh, A. V.; Pernik, I.; Weller, A. S.; McIndoe, J. S. Simultaneous Orthogonal Methods for the Real-Time Analysis of Catalytic Reactions. ACS Catal. 2016, 6 (10), 6911–6917. https://doi.org/10.1021/acscatal.6b01489.

(28) McIndoe, J. S.; Vikse, K. L. Assigning the ESI Mass Spectra of Organometallic and Coordination Compounds. J. Mass Spectrom. 2019, 54 (5), 466–479. https://doi.org/10.1002/jms.4359.

(29) Chagunda, I. C.; Williams, P. J. H.; Fisher, T.; Stock, N. L.; Beach, D. G.; Thomas, G. T.; Zhu, J.; McIndoe, J. S. Comparative Assessment of ESI-MS Softness for Inorganic Complexes: How Soft Is Your ESI-MS? Eur. J. Inorg. Chem. n/a (n/a), e202400077. https://doi.org/10.1002/ejic.202400077.

(30) Trefz, T. K.; Henderson, M. A.; Linnolahti, M.; Collins, S.; McIndoe, J. S. Mass Spectrometric Characterization of Methylaluminoxane-Activated Metallocene Complexes. Chem. – Eur. J. 2015, 21 (7), 2980–2991. https://doi.org/10.1002/chem.201405319.

(31) Beierlein, C. H.; Breit, B.; Paz Schmidt, R. A.; Plattner, D. A. Online Monitoring of Hydroformylation Intermediates by ESI-MS. Organometallics 2010, 29 (11), 2521–2532. https://doi.org/10.1021/om100131t.

(32) Vikse, K.; Khairallah, G. N.; McIndoe, J. S.; O'Hair, R. A. J. Fixed-Charge Phosphine Ligands to Explore Gas-Phase Coinage Metal-Mediated Decarboxylation Reactions. Dalton Trans. 2013, 42 (18), 6440–6449. https://doi.org/10.1039/C3DT32285H.

(33) Crawford, E.; Lohr, T.; Leitao, E. M.; Kwok, S.; McIndoe, J. S. Distannoxane Speciation during Esterification Catalysis: Revealing Insights Provided by Electrospray Ionization Mass Spectrometry. Dalton Trans. 2009, No. 42, 9110–9112. https://doi.org/10.1039/B913492A.

(34) Thomas, G. T.; Janusson, E.; Zijlstra, H. S.; McIndoe, J. S. Step-by-Step Real Time Monitoring of a Catalytic Amination Reaction. Chem. Commun. 2019, 55 (78), 11727–11730. https://doi.org/10.1039/C9CC05076K.

(35) Mass Analysers. In Mass Spectrometry of Inorganic, Coordination and Organometallic Compounds; John Wiley & Sons, Ltd, 2005; pp 23–46. https://doi.org/10.1002/0470014318.ch2.

(36) Tremsin, A. S.; McPhate, J. B.; Steuwer, A.; Kockelmann, W.; M Paradowska, A.; Kelleher, J. F.; Vallerga, J. V.; Siegmund, O. H. W.; Feller, W. B. High-Resolution Strain Mapping Through Time-of-Flight Neutron Transmission Diffraction with a

Microchannel Plate Neutron Counting Detector. Strain 2012, 48 (4), 296–305. https://doi.org/10.1111/j.1475-1305.2011.00823.x.

(37) Madeira, P. J. A.; Florêncio, M. H.; Madeira, P. J. A.; Florêncio, M. H. Applications of Tandem Mass Spectrometry: From Structural Analysis to Fundamental Studies. In Tandem Mass Spectrometry - Applications and Principles; IntechOpen, 2012. https://doi.org/10.5772/31736.

(38) J. Scott McIndoe, William Henderson, Mass Spectrometry of Inorganic and Organometallic Compounds: Tools - Techniques – Tips, Wiley, 2005, ISBN: 978-0-470 85016-9.

(39) Krista L. Vikse, Michael P. Woods, and J. Scott McIndoe, Pressurized Sample Infusion for the Continuous Analysis of Air- And Moisture-Sensitive Reactions Using Electrospray Ionization Mass Spectrometry, *Organometallics*, 2010, *29* (23), 6615-6618, DOI: 10.1021/om1008082

(40) Vikse, Krista & Ahmadi, Zohrab & Luo, Jingwei & Wal, Nicole & Daze, Kevin & Taylor, Nichole & McIndoe, J., Pressurized sample infusion: An easily calibrated, low volume pumping system for ESI-MS analysis of reactions. International Journal of Mass Spectrometry, 2012, 323–324. 8-13. 10.1016/j.ijms.2012.03.007.

(41) Amelia V. Hesketh, Steven Nowicki, Kristen Baxter, Rhonda L. Stoddard, and J. Scott McIndoe, Simplified Real-Time Mass Spectrometric Analysis of Reactions, *Organometallics*, 2015, *34* (15), 3816-3819, DOI: 10.1021/acs.organomet.5b00460

(42) Thomas, G. T.; Donnecke, S.; Chagunda, I. C.; McIndoe, J. S. Pressurized Sample Infusion. Chemistry–Methods 2022, 2 (1), e202100068. https://doi.org/10.1002/cmtd.202100068.

(43) Thomas, G. T.; Ronda, K.; McIndoe, J. S. A Mechanistic Investigation of the Pd-Catalyzed Cross-Coupling between N -Tosylhydrazones and Aryl Halides. Dalton Trans. 2021, 50 (43), 15533–15537. https://doi.org/10.1039/D1DT03161A.

(44) Yunker, L. P. E.; Ahmadi, Z.; Logan, J. R.; Wu, W.; Li, T.; Martindale, A.; Oliver, A. G.; McIndoe, J. S. Real-Time Mass Spectrometric Investigations into the Mechanism of the Suzuki–Miyaura Reaction. Organometallics 2018, 37 (22), 4297–4308. https://doi.org/10.1021/acs.organomet.8b00705.

(45) Eric J., Harmen S., Peter P. T. N., Landon M., Julio M., McIndoe J. S. Real-time analysis of Pd2(dba)3 activation by phosphine ligands, *Chem. Commun.*, 2017,53, 854-856

(46) Zijlstra, H. S.; Joshi, A.; Linnolahti, M.; Collins, S.; McIndoe, J. S. Modifying Methylalumoxane via Alkyl Exchange. Dalton Trans. 2018, 47 (48), 17291–17298. https://doi.org/10.1039/C8DT04242J.

(47) Killeen, C.; Liu, J.; Zijlstra, H.; Maass, F.; Piers, J.; Adams, R.; Oliver, A. G.; McIndoe, J. S. Competitive Isomerization and Catalyst Decomposition During Ring-Closing Metathesis. ChemRxiv January 24, 2023. https://doi.org/10.26434/chemrxiv-2023-lrg06.

(48) Ting, M. Y. C.; Yunker, L. P. E.; Chagunda, I. C.; Hatlelid, K.; Vieweg, M.; McIndoe, J. S. A Mechanistic Investigation of the Suzuki Polycondensation Reaction Using MS/MS Methods. Catal. Sci. Technol. 2021, 11 (13), 4406–4416. https://doi.org/10.1039/D1CY00743B.

(49) Mohamed Abdel Aaty Ahmed. Catalyst deactivation Common causes, Nitrogen and Syngas Conference, 5-8 March 2013, Berlin, Germany–

(50) Oudar, J. Deactivation and Poisoning of Catalysts; CRC Press, 1985.

(51) Tuttle, R. R.; Folkman, S. J.; Rubin, H. N.; Finke, R. G.; Reynolds, M. M. Copper Metal–Organic Framework Surface Catalysis: Catalyst Poisoning, IR Spectroscopic, and Kinetic Evidence Addressing the Nature and Number of the Catalytically Active Sites En Route to Improved Applications. ACS Appl. Mater. Interfaces 2020. https://doi.org/10.1021/acsami.0c08961.

(52) Gärtner, D.; Sandl, S.; Jacobi Von Wangelin, A. Homogeneous vs. Heterogeneous: Mechanistic Insights into Iron Group Metal-Catalyzed Reductions from Poisoning Experiments. Catal. Sci. Technol. 2020, 10 (11), 3502–3514. https://doi.org/10.1039/D0CY00644K.

(53) Schwartz, J. Alkane Activation by Oxide-Bound Organorhodium Complexes. Acc. Chem. Res. 1985, 18 (10), 302–308. https://doi.org/10.1021/ar00118a004.

(54) Crabtree, R. H. Resolving Heterogeneity Problems and Impurity Artifacts in Operationally Homogeneous Transition Metal Catalysts. ACS Publications. https://doi.org/10.1021/cr2002905.

(55) Artero, V.; Fontecave, M. Solar Fuels Generation and Molecular Systems: Is It Homogeneous or Heterogeneous Catalysis? Chem. Soc. Rev. 2013, 42 (6), 2338–2356. https://doi.org/10.1039/C2CS35334B.

(56) H, L. A New Catalyst for Selective Hydrogenation. Helv Chim Acta 1952, 35, 446–450.

(57) Zhao, X.; Zhou, L.; Zhang, W.; Hu, C.; Dai, L.; Ren, L.; Wu, B.; Fu, G.; Zheng, N. Thiol Treatment Creates Selective Palladium Catalysts for Semihydrogenation of Internal Alkynes. Chem 2018, 4 (5), 1080–1091. https://doi.org/10.1016/j.chempr.2018.02.011.

(58) Gui, B.; Yee, K.-K.; Wong, Y.-L.; Yiu, S.-M.; Zeller, M.; Wang, C.; Xu, Z. Tackling Poison and Leach: Catalysis by Dangling Thiol–Palladium Functions within a Porous Metal–Organic Solid. Chem. Commun. 2015, 51 (32), 6917–6920. https://doi.org/10.1039/C5CC00140D.

(59) Stumpf, A.; McClory, A.; Yajima, H.; Segraves, N.; Angelaud, R.; Gosselin, F. Development of an Efficient, Safe, and Environmentally Friendly Process for the Manufacture of GDC-0084. Org. Process Res. Dev. 2016, 20 (4), 751–759. https://doi.org/10.1021/acs.oprd.6b00011.

(60) Anton, D. R.; Crabtree, R. H. Dibenzo[a,e]cyclooctatetraene in a proposed test for heterogeneity in catalysts formed from soluble platinum-group metal complexes. ACS Publications. https://doi.org/10.1021/om50001a013.

(61) Cheng, F. Y.; Chen, J.; Gou, X. L. MoS2–Ni Nanocomposites as Catalysts for Hydrodesulfurization of Thiophene and Thiophene Derivatives. Adv. Mater. 2006, 18 (19), 2561–2564. https://doi.org/10.1002/adma.200600912.

(62) Kishan, G.; Coulier, L.; van Veen, J. A. R.; Niemantsverdriet, J. W. Promoting Synergy in CoW Sulfide Hydrotreating Catalysts by Chelating Agents. J. Catal. 2001, 200 (1), 194–196. https://doi.org/10.1006/jcat.2001.3203.

(63) Hurtado, P.; Ordóñez, S.; Sastre, H.; Díez, F. V. Combustion of Methane over Palladium Catalyst in the Presence of Inorganic Compounds: Inhibition and Deactivation Phenomena. Appl. Catal. B Environ. 2004, 47 (2), 85–93. https://doi.org/10.1016/S0926-3373(03)00328-X.

(64) Poly(4-vinylpyridine) and Quadrapure TU as Selective Poisons for Soluble Catalytic Species in Palladium-Catalyzed Coupling Reactions – Application to Leaching from Polymer-Entrapped Palladium - Richardson - 2006 - Advanced Synthesis & Catalysis - Wiley Online Library. https://onlinelibrary.wiley.com/doi/abs/10.1002/adsc.200606021 (accessed 2024-02-25).

(65) Huang, L.; Ang, T. P.; Wang, Z.; Tan, J.; Chen, J.; Wong, P. K. On the Roles of Solid-Bound Ligand Scavengers in the Removal of Palladium Residues and in the Distinction between Homogeneous and Heterogeneous Catalysis. ACS Publications. https://doi.org/10.1021/ic100824e.

(66) Elmekawy, A. Simultaneous Determination of Residual Palladium and Thiol Homogeneous Scavenger N-Acetylcysteine in Active Pharmaceutical Ingredients Using Inductive Coupled Plasma-Mass Spectrometry. Org. Process Res. Dev. 2021, 25 (6), 1352–1359. https://doi.org/10.1021/acs.oprd.0c00542.

(67) Garrett, C. E.; Prasad, K. The Art of Meeting Palladium Specifications in Active Pharmaceutical Ingredients Produced by Pd-Catalyzed Reactions. Adv. Synth. Catal. 2004, 346 (8), 889–900. https://doi.org/10.1002/adsc.200404071.

(68) Metwally, M. A.; Abdel-Wahab, B. F. Utility of Cyclohexanethiols in Organic Synthesis. 2009.

(69) Itoh, T.; Mase, T. Practical Thiol Surrogates and Protective Groups for Arylthiols for Suzuki−Miyaura Conditions. J. Org. Chem. 2006, 71 (5), 2203–2206. https://doi.org/10.1021/jo052624z.

(70) Migita, T.; Shimizu, T.; Asami, Y.; Shiobara, J.; Kato, Y.; Kosugi, M. The Palladium Catalyzed Nucleophilic Substitution of Aryl Halides by Thiolate Anions. Bull. Chem. Soc. Jpn. 1980, 53 (5), 1385–1389. https://doi.org/10.1246/bcsj.53.1385.

(71) Norris, T.; Leeman, K. Development of a New Variant of the Migita Reaction for Carbon−Sulfur Bond Formation Used in the Manufacture of Tetrahydro-4-[3-[4-

(2-Methyl-1H-Imidazol-1-Yl)Phenyl]Thio]Phenyl-2H-Pyran-4-Carboxamide. Org. Process Res. Dev. 2008, 12 (5), 869–876. https://doi.org/10.1021/op800098a.

(72) de Lambert de Boisjan, A.; Allemann, C.; Fadini, L. Impact of Solvent and Their Contaminants on Pd/C Catalyzed Suzuki-Miyaura Cross-Coupling Reactions. Helv. Chim. Acta 2021, 104 (6), e2100035. https://doi.org/10.1002/hlca.202100035.

(73) Diederich, F.; Stang, P. J. Metal-Catalyzed Cross-Coupling Reactions; John Wiley & Sons, 2008.

(74) Vikse, K. L.; Henderson, M. A.; Oliver, A. G.; McIndoe, J. S. Direct Observation of Key Intermediates by Negative-Ion Electrospray Ionisation Mass Spectrometry in Palladium-Catalysed Cross-Coupling. Chem. Commun. 2010, 46 (39), 7412–7414. https://doi.org/10.1039/C0CC02773A.

(75) Chagunda, I. C.; Williams, P. J. H.; Fisher, T.; Stock, N. L.; Beach, D. G.; Thomas, G. T.; Zhu, J.; McIndoe, J. S. How Soft Is Your ESI-MS Anyway? ChemRxiv January 30, 2024. https://doi.org/10.26434/chemrxiv-2024-tkrc5.

(76) Cao, R.; Hong, M.; Jiang, F.; Kang, B.; Xie, X.; Liu, H. Syntheses of Palladium (II) Complexes with Thiolate and Phosphine Ligands. X-Ray Crystal Structures of [Pd (Tdt)(PPh3) 2]· C2H4Cl2 and [Pd2 (Hmp) 2 (PPh3) Cl2]. Polyhedron 1996, 15 (16), 2661–2670.

(77) Omari, I.; Randhawa, P.; Randhawa, J.; Yu, J.; McIndoe, J. S. Structure, Anion, and Solvent Effects on Cation Response in ESI-MS. J. Am. Soc. Mass Spectrom. 2019, 30 (9), 1750–1757. https://doi.org/10.1007/s13361-019-02252-0.

(78) Henderson, W.; McIndoe, J. S.; Nicholson, B. K.; Dyson, P. J. Electrospray Mass Spectrometry of Metal Carbonyl Complexes †. J. Chem. Soc. Dalton Trans. 1998, No. 4, 519–526. https://doi.org/10.1039/a707868d.

(79) Vikse, K.; Naka, T.; McIndoe, J. S.; Besora, M.; Maseras, F. Oxidative Additions of Aryl Halides to Palladium Proceed through the Monoligated Complex. ChemCatChem 2013, 5 (12), 3604–3609. https://doi.org/10.1002/cctc.201300723.

(80) Baranano, D.; Hartwig, J. F. Carbon-Heteroatom Bond-Forming Reductive Elimination. Mechanism, Importance of Trapping Reagents, and Unusual Electronic Effects during Formation of Aryl Sulfides. J. Am. Chem. Soc. 1995, 117 (10), 2937–2938. https://doi.org/10.1021/ja00115a033.

(81) Rojas, A. J.; Wolfe, J. M.; Dhanjee, H. H.; Buslov, I.; Truex, N. L.; Liu, R. Y.; Massefski, W.; Pentelute, B. L.; Buchwald, S. L. Palladium–Peptide Oxidative Addition Complexes for Bioconjugation. Chem. Sci. 2022, 13 (40), 11891–11895. https://doi.org/10.1039/D2SC04074C.

(82) Vinogradova, E. V.; Zhang, C.; Spokoyny, A. M.; Pentelute, B. L.; Buchwald, S. L. Organometallic Palladium Reagents for Cysteine Bioconjugation. Nature 2015, 526 (7575), 687–691. https://doi.org/10.1038/nature15739.

(83) Kim, Y.-J.; Choi, K.-Y.; Lee, S. G.; Zheng, Z. N.; Lee, S. W. Oxidative Addition of Aryl Disulfides to Pd(0) Complexes: Synthesis and Structures of Bis(Thiolato)

Pd(II) Complexes. Bull. Korean Chem. Soc. 2014, 35 (4), 1205–1208. https://doi.org/10.5012/bkcs.2014.35.4.1205.

(84) Ananikov, V. P.; Zalesskiy, S. S.; Kachala, V. V.; Beletskaya, I. P. NMR Approach for the Identification of Dinuclear and Mononuclear Complexes: The First Detection of [Pd(SPh)2(PPh3)2] and [Pd2(SPh)4(PPh3)2] – The Intermediate Complexes in the Catalytic Carbon–Sulfur Bond Formation Reaction. J. Organomet. Chem. 2011, 696 (1), 400–405. https://doi.org/10.1016/j.jorganchem.2010.10.012.

(85) Guo J, Zha J, Zhang T, Ding CH, Tan Q, Xu B. $PdCl_2$/DMSO-Catalyzed Thiol-Disulfide Exchange: Synthesis of Unsymmetrical Disulfide. Org Lett. 2021, 23(8):3167-3172. doi: 10.1021/acs.orglett.1c00858.

(86) Königsberger, K.; Chen, G.-P.; Wu, R. R.; Girgis, M. J.; Prasad, K.; Repič, O.; Blacklock, T. J. A Practical Synthesis of 6-[2-(2,5-Dimethoxyphenyl)Ethyl]-4-Ethylquinazoline and the Art of Removing Palladium from the Products of Pd-Catalyzed Reactions. Org. Process Res. Dev. 2003, 7 (5), 733–742. https://doi.org/10.1021/op034072x.

(87) Sisombath NS, Jalilehvand F. Similarities between N-Acetylcysteine and Glutathione in Binding to Lead(II) Ions. Chem Res Toxicol. 2015, 28(12):2313-24. doi: 10.1021/acs.chemrestox.5b00323.

(88) Corbi, P. P.; Cagnin, F.; Massabni, A. C. Chemical and Spectroscopic Studies of a New Palladium(II) Complex with N -Acetyl-L-Cysteine. J. Coord. Chem. 2008, 61 (22), 3666–3673. https://doi.org/10.1080/00958970802108809.

(89) Hadi, S.; Appleton, T. G. Reactions of Cisplatin Hydrolytes, Cis-[Pt(15NH3)2(H2O) 2]2+, with N-Acetyl-L-Cysteine. Russ. J. Inorg. Chem. 2010, 55 (2), 223–228. https://doi.org/10.1134/S0036023610020142.

(90) Schwab, J. J.; Wilkinson, E. C.; Wilson, S. R.; Shapley, P. A. Nitridoosmium(VI) and Nitridoruthenium(VI) Complexes of Cysteine(2-) and Related Ligands. J. Am. Chem. Soc. 1991, 113 (16), 6124–6129. https://doi.org/10.1021/ja00016a031.

(91) Atencio, R.; Esteruelas, M. A.; Lahoz, F. J.; Oro, L. A.; Ruiz, N. Synthesis and X-Ray Structure of the Unusual Cysteine-Complex OsH2{OC(=O)CH[NHC(=O)CH3]CH2S}(PiPr3)2. Inorg. Chem. 1995, 34 (4), 1004–1006. https://doi.org/10.1021/ic00108a040.

(92) Mitchell, K. A.; Jensen, C. M. Synthesis, Characterization, and Reactivity of Platinum Cysteinato and Related Thiolato Complexes: Molecular Structure of Pt2(.Mu.-N-Acetyl-L-Cysteine-S)2(Bpy)2. Inorg. Chem. 1995, 34 (17), 4441–4446. https://doi.org/10.1021/ic00121a023.

(93) Corbi, P. P.; Cagnin, F.; Massabni, A. C. Synthesis and Characterization of a Platinum(II) Complex with N-Acetyl-L-Cysteine. J. Coord. Chem. 2009, 62 (17), 2764–2771. https://doi.org/10.1080/00958970902942974.

(94) Barton, M. R.; Zhang, Y.; Atwood, J. D. Mono-Sulfonated Derivatives of Triphenylphosphine, $[NH_4]$TPPMS and $M(TPPMS)_2$ (TPPMS = $P(Ph)_2(m\text{-}C_6H_4SO_3)$; M = Mn^{2+}, Fe^{2+}, Co^{2+} and Ni^{2+}). Crystal Structure Determinations for

[NH_4][TPPMS]·½H_2O, [Fe(H_2O)$_5$(TPPMS)]TPPMS, [Co(H_2O)5TPPMS]TPPMS and [Ni(H_2O)$_6$](TPPMS)$_4$·H_2O. J. Coord. Chem. 2002, 55 (8), 969–983. https://doi.org/10.1080/0095897022000002295.

(95) Douglas A. Skoog, Donald M. West, F. James Holler, Stanley R. Crouch Fundamentals of Analytical Chemistry, 2021, 10th Edition, ISBN-13: 9780357450536

(96) Franklin, A. Calibration. Perspect. Sci. 1997, 5 (1), 31–80. https://doi.org/10.1162/posc_a_00518.

(97) Prichard, Liz & Barwick, Vicki. Preparation of Calibration Curves A Guide to Best Practice. 2003, 10.13140/RG.2.2.36338.76488. 10.13140/RG.2.2.36338.76488.

(98) Stankov, L. Calibration Curves, Scatterplots and the Distinction between General Knowledge and Perceptual Tasks. Learn. Individ. Differ. 1998, 10 (1), 29–50. https://doi.org/10.1016/S1041-6080(99)80141-1.

(99) Harvey D., Analytical Chemistry 2.1. Open Textbook Library, 2016, https://open.umn.edu/opentextbooks/textbooks/486.

(100) Jurado, J. M.; Alcázar, A.; Muñiz-Valencia, R.; Ceballos-Magaña, S. G.; Raposo, F. Some Practical Considerations for Linearity Assessment of Calibration Curves as Function of Concentration Levels According to the Fitness-for-Purpose Approach. Talanta 2017, 172, 221–229. https://doi.org/10.1016/j.talanta.2017.05.049.

(101) Thompson, M. Amc Technical Brief. Royal Society of Chemistry, 2000.

(102) Skoog, D. A.; Holler, F. J.; Crouch, S. R. Principles of Instrumental Analysis, 7th edition.; Cengage Learning: Australia, 2017.

(103) Cuadros-Rodríguez, L.; Gámiz-Gracia, L.; Almansa-López, E.; Bosque-Sendra, J. Calibration in Chemical Measurement Processes. II. A Methodological Approach. TrAC Trends Anal. Chem. 2001, 20, 620–636. https://doi.org/10.1016/S0165-9936(01)00111-X.

(104) Williams, P. J. H.; Killeen, C.; Chagunda, I. C.; Henderson, B.; Donnecke, S.; Munro, W.; Sidhu, J.; Kraft, D.; Harrington, D. A.; McIndoe, J. S. Continuous Addition Kinetic Elucidation: Catalyst and Reactant Order, Rate Constant, and Poisoning from a Single Experiment. Chem. Sci. 2023, 14 (36), 9970–9977. https://doi.org/10.1039/D3SC02698A.

(105) Spitha, N.; Doolittle, P. S.; Buchberger, A. R.; Pazicni, S. Simulation-Based Guided Inquiry Activity for Deriving the Beer–Lambert Law. J. Chem. Educ. 2021, 98 (5), 1705–1711. https://doi.org/10.1021/acs.jchemed.0c01433.

(106) Mamouei, M.; Budidha, K.; Baishya, N.; Qassem, M.; Kyriacou, P. A. An Empirical Investigation of Deviations from the Beer–Lambert Law in Optical Estimation of Lactate. Sci. Rep. 2021, 11 (1), 13734. https://doi.org/10.1038/s41598-021-92850-4.

Appendix

Half-life determination of $[Pd(PPh_3)_n(1)]^-$ (n = 0-2) species

Half-life ($t_{½}$) is the time required for a quantity (of substance) to reduce to half of its initial value. For the calculation of the half-life of the species, the region where the intensity of the $[Pd(PPh_3)_n(1)]^-$ species drops upon addition of the poison was selected (4.42 min to 4.57 min). Then the ln[X] vs time graph was constructed (where, [x] = concentration or the intensity of the species). Since this follows the 1st order kinetics, the half-life of the 1st order reaction was calculated by using the $t_{½} = \ln 2 / k$ equation after obtaining the slope (where, slope = k)

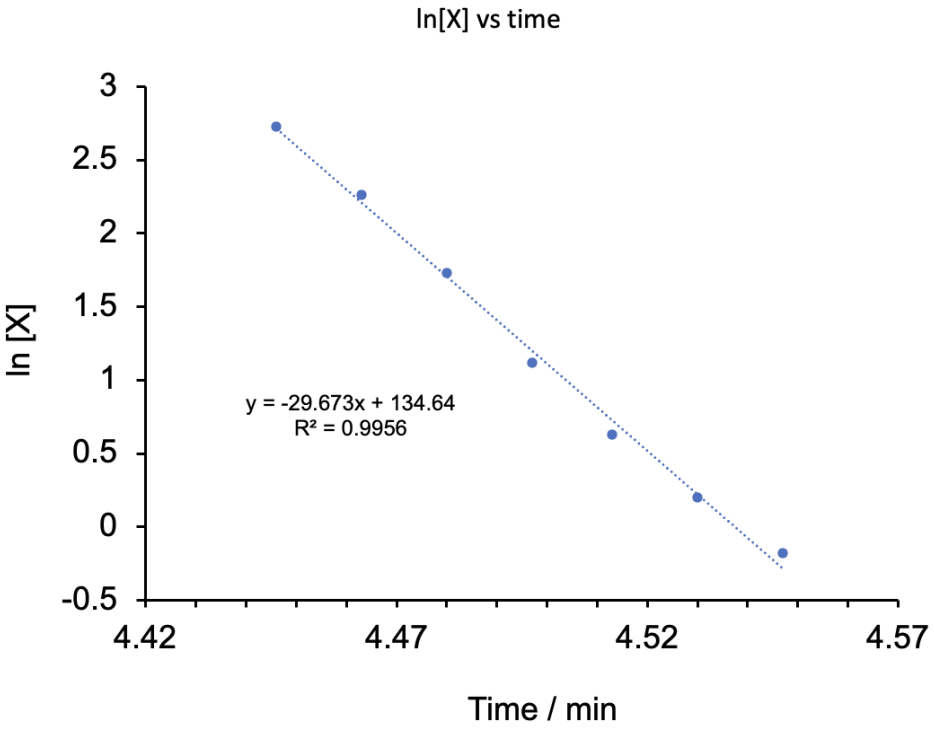

Figure A1. ln [X] vs time graph for half-life calculation where [X] is the concentration of $[Pd(PPh_3)_n(1)]^-$ species.

MS/MS reaction intermediates characterization

All MS/MS spectra were collected using PSI-ESI-MS technique with the same tuning parameters as in full scan conditions. In addition, the optimized CID collision energies for each identified species are listed in Table S1. The product ions detected in each CID experiment along with isotope pattern matching were diagnostic for identifying the catalytically relevant species in each experiment. All predicted isotope pattern calculations and experimental matching was done using PythoMS[5].

Table A1: CID scan specifications for relevant Pd reaction intermediates.

Precursor Ion, *m/z*		Product Ion(s), *m/z*		CE, *V*
$[Pd(PPh_3)(\mathbf{1})(C_6H_4S_2)]^-$	849.0	$[Pd(C_6H_4S_2)]^-$	586.9	15
		[**1**]–	341.0	05
$[Pd_2(PPh_3)(\mathbf{1})(C_6H_4S_2)_2]^-$	1096.8	$[Pd_2(\mathbf{1})(C_6H_4S_2)_2]^-$	834.8	23
		[**1**]$^-$	341.0	05
$[Pd(PPh_3)_2(Ph)(C_6H_4S_2)_2]^+$	987.0	$[Pd(PPh_3)(Ph)(C_6H_4S_2)_2]^+$	725.0	12
		$[Pd(PPh_3)(Ph)(C_6H_4S_2)]^+$	585.0	12
		$[Pd(Ph)(C_6H_4S_2)_2]^+$	462.8	12
		PPh_4^+	339.1	11
$[Pd(\mathbf{1})(CH_3N_2S)_2]^-$	596.8	[**1**]–	341.1	05
$[Pd(PPh_3)(CH_3N_2S)]^+$	443.0	$[Pd(PPh_3)]^+$	368.9	20
		PPh_3^+	261.0	11

$[Pd(PPh_3)_2(CH_3N_2S)]^+$	705.0	$[Pd(PPh_3)(CH_3N_2S)]^+$ PPh_4^+	443.0 339.1	20 12
$[Pd(PPh_3)(\mathbf{1})(C_5H_7NO_3S)]^-$	871.9	$[Pd(PPh_3)(\mathbf{1})]^-$ $[Pd(1)(C_5H_7NO_3S)]^-$ $[\mathbf{1}]^-$	708.9 607.8 341.0	12 10 05
$[Pd(PPh_3)_2(C_5H_8NO_3S)]^+$	792.0	$[Pd(PPh_3)(C_5H_8NO_3S)]^+$ PPh_3^+	664.9 262.0	12 10
$[Pd_2(PPh_3)_3(C_5H_8NO_3S)]^+$	1162.0	$[Pd_2(PPh_3)_2(C_5H_8NO_3S)]^+$	899.9	12

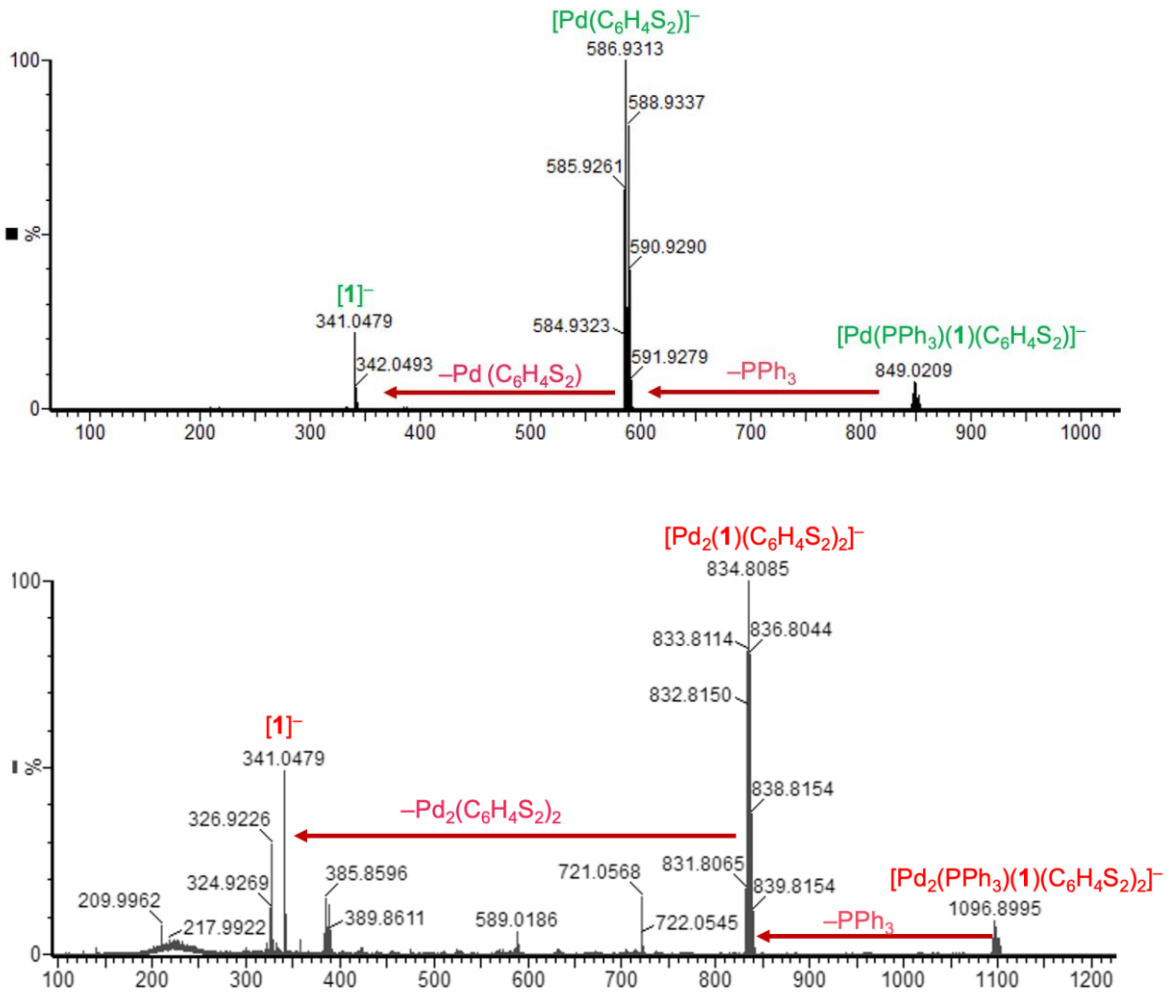

Figure A2. CID spectra of the $[Pd(PPh_3)(\mathbf{1})(C_6H_4S_2)]^-$ (top) and $[Pd_2(PPh_3)(\mathbf{1})(C_6H_4S_2)_2]^-$ (bottom) species in negative ion mode (poison: 1,2-benzenedithiol addition on catalyst activation). The major fragmented ions are shown in the spectra.

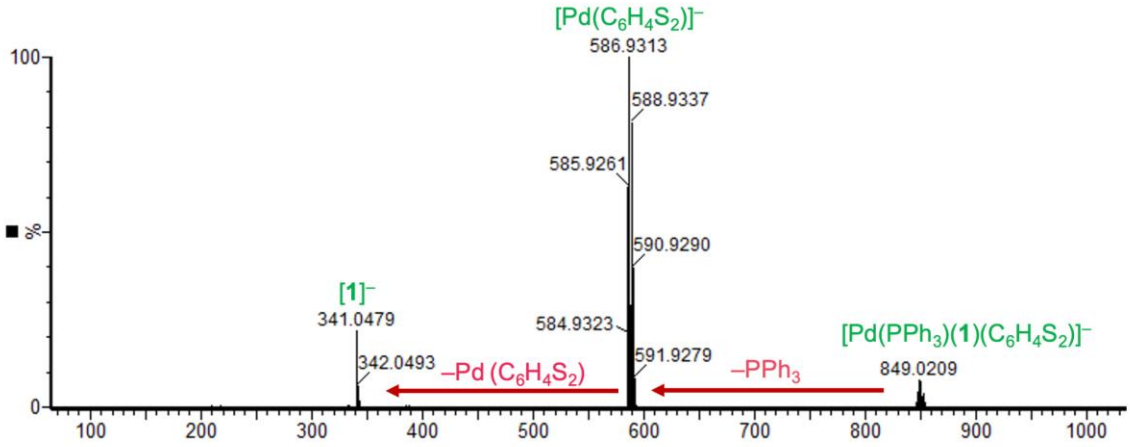

Figure A3. CID spectrum of the $[Pd(PPh_3)(\mathbf{1})(C_6H_4S_2)]^-$ in negative ion mode (poison: 1,2-benzenedithiol addition on oxidative addition). The major fragmented ions are shown in the spectrum.

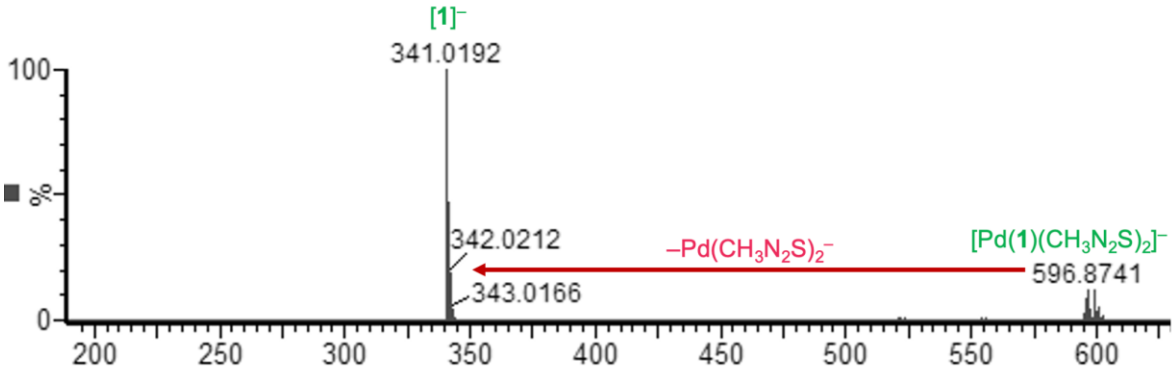

Figure A4. CID spectrum of the $[Pd(\mathbf{1})(CH_3N_2S)_2]^-$ in negative ion mode (poison: thiourea addition on catalyst activation). The major fragmented ions are shown in the spectrum.

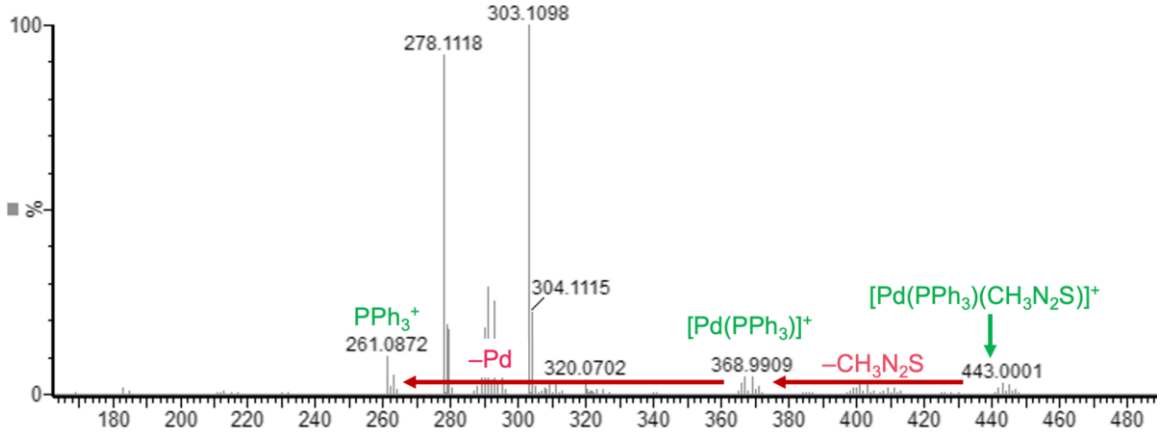

Figure A5. CID spectrum of the $[Pd(PPh_3)(CH_3N_2S)]^+$ in positive ion mode (poison: thiourea addition on catalyst activation). The major fragmented ions are shown in the spectrum.

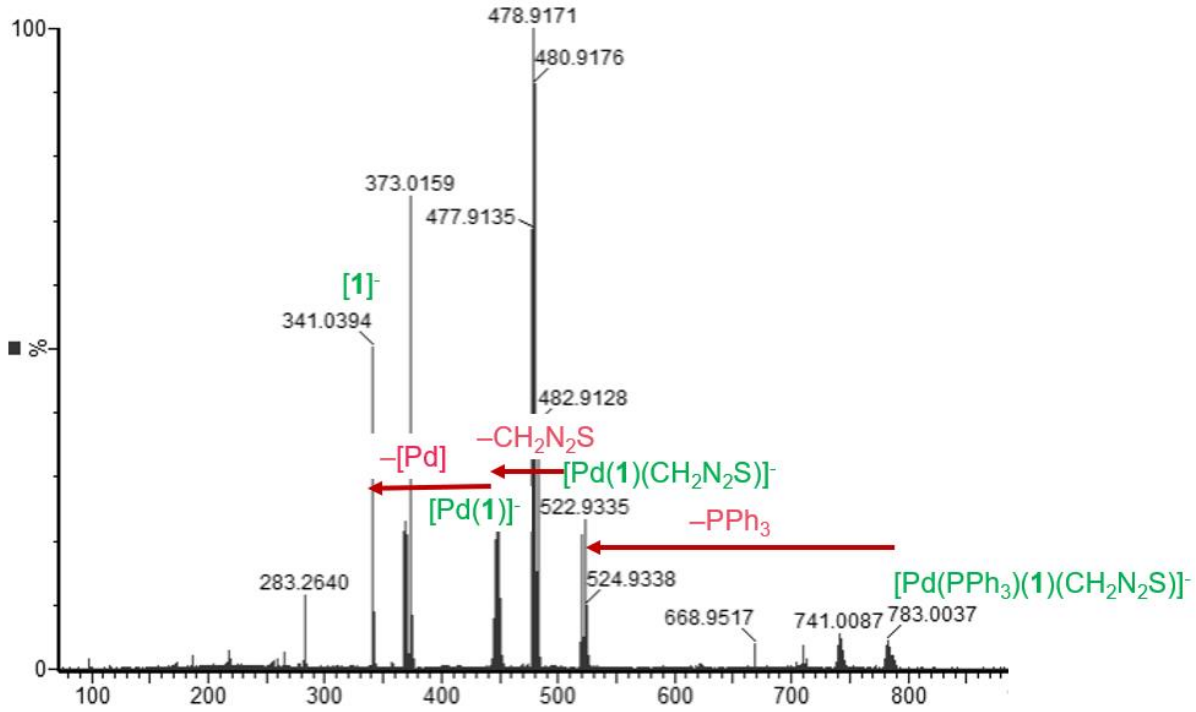

Figure A6. CID spectrum of the $[Pd(PPh_3)(1)(CH_2N_2S)]^-$ in negative ion mode (poison: thiourea addition on oxidative addition). The major fragmented ions are shown in the spectrum.

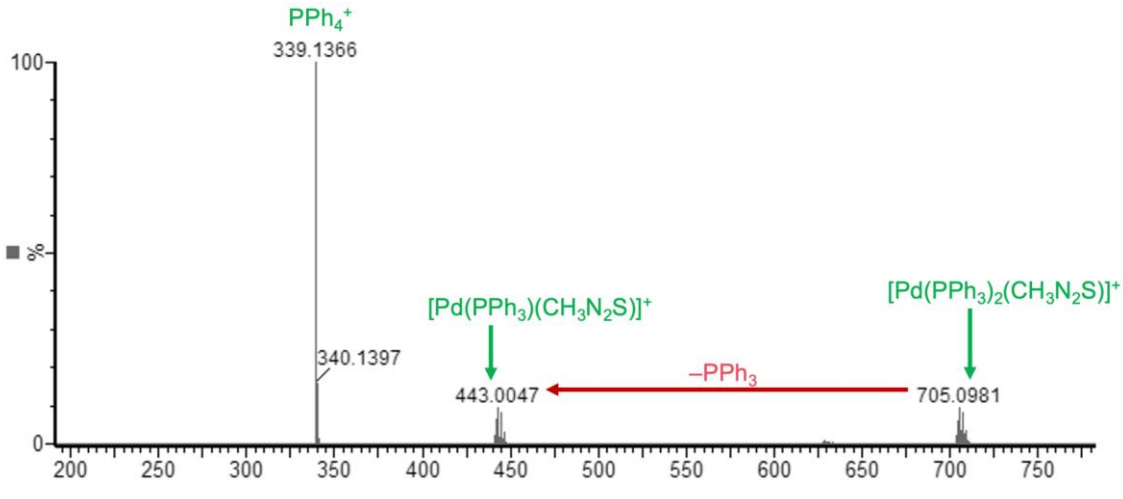

Figure A7. CID spectrum of the $[Pd(PPh_3)_2(CH_3N_2S)]^+$ in positive ion mode (poison: thiourea addition on oxidative addition). The major fragmented ions are shown in the spectrum.

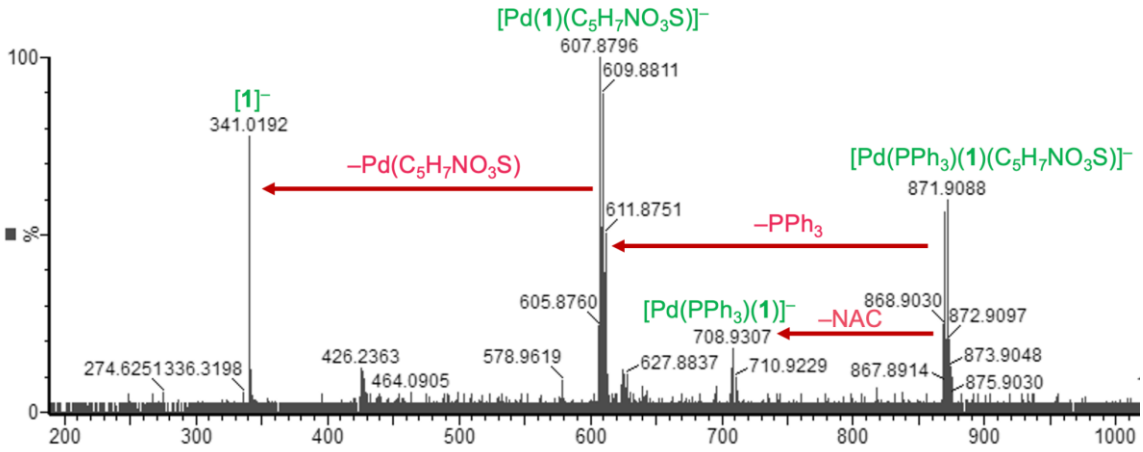

Figure A8. CID spectrrum of the $[Pd(PPh_3)(1)(C_5H_7NO_3S)]^-$ in negative ion mode (poison: *N*-acetylcysteine addition on catalyst activation). The major fragmented ions are shown in the spectrum.

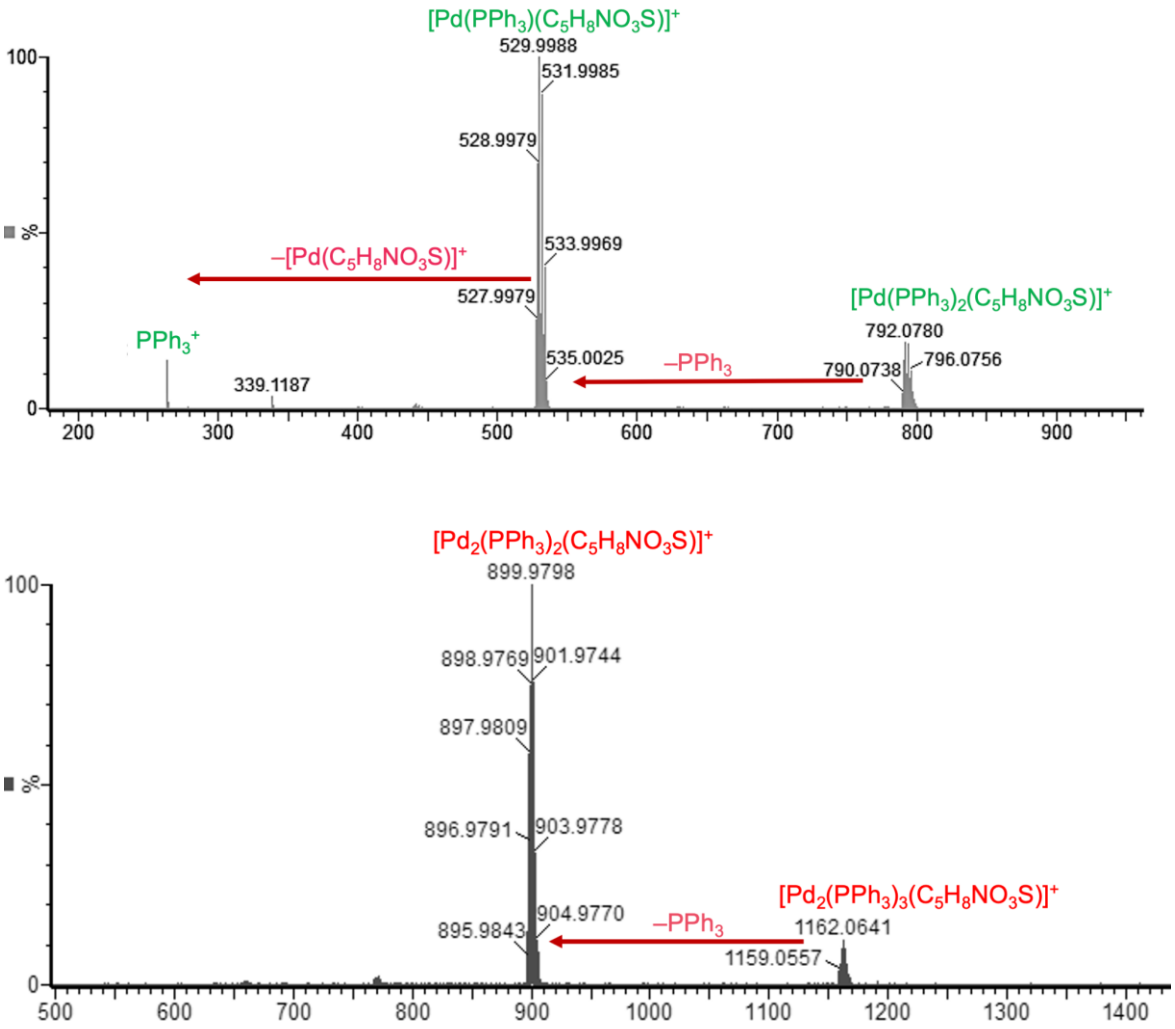

Figure A9. CID spectra of the $[Pd(PPh_3)_2(C_5H_7NO_3S)]^+$ (top) and $[Pd_2(PPh_3)_3(C_5H_7NO_3S)]^+$ (bottom) in positive ion mode (poison: *N*-acetylcysteine addition on catalyst activation). The major fragmented ions are shown in the spectrum.

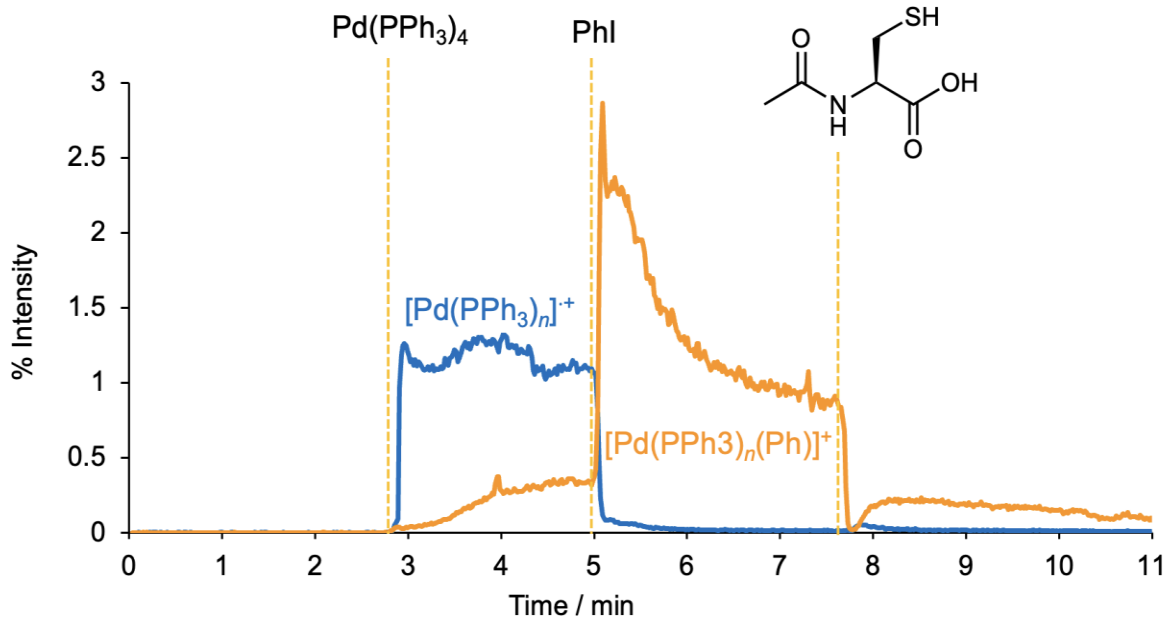

Figure A10. PSI-ESI-MS reaction monitoring in positive ion mode showing the effect of poison: *N*-acetylcysteine addition on oxidative addition. A drop in relative abundance of $[Pd(PPh_3)_n]^{\cdot+}$ (blue trace), where n = 1-2, is observed upon addition of the aryl halide: PhI and the resulting oxidatively added product: $[Pd(PPh_3)_n(Ph)]^{+}$ disappeared. No indication for the Pd poisoned products upon addition of *N*-acetylcysteine.

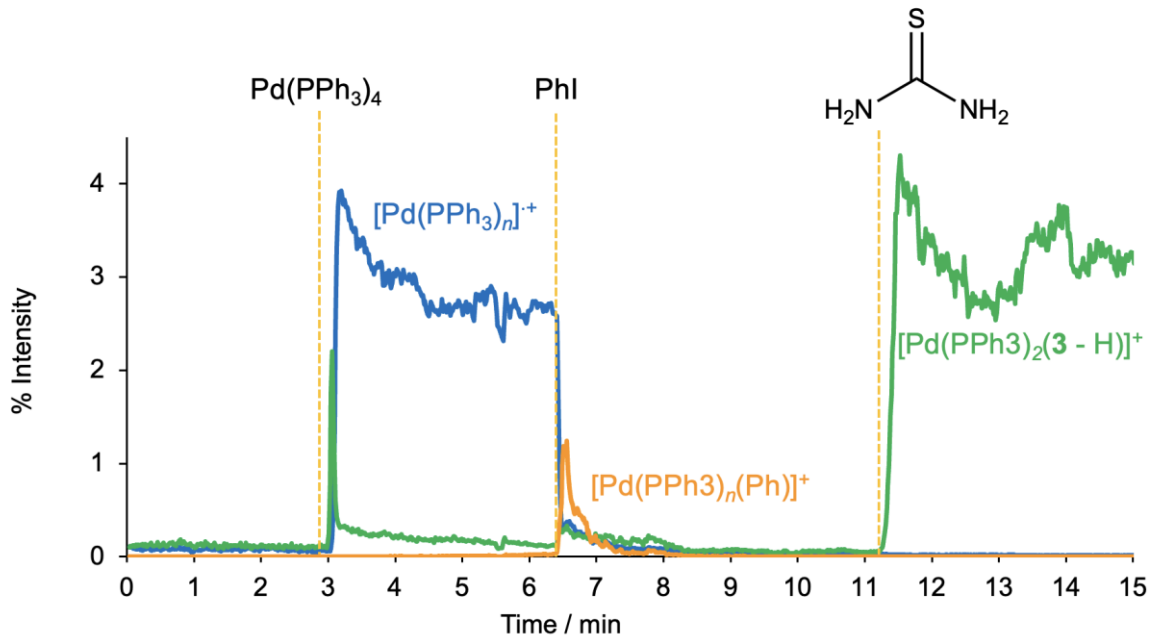

Figure A11. PSI-ESI-MS reaction monitoring in positive ion mode showing the effect of poison: thiourea addition on Pd(II) species. A drop in relative abundance of $[Pd(PPh_3)_n]^{\cdot+}$ (blue trace), where n = 1-2, is observed upon addition of the aryl halide: PhI and the resulting oxidatively added product: $[Pd(PPh_3)_n(Ph)]^+$ is disappeared and formation of Pd poisoned product: $[Pd(PPh_3)_2(CH_3N_2S)]^+$ is shown in green color trace.

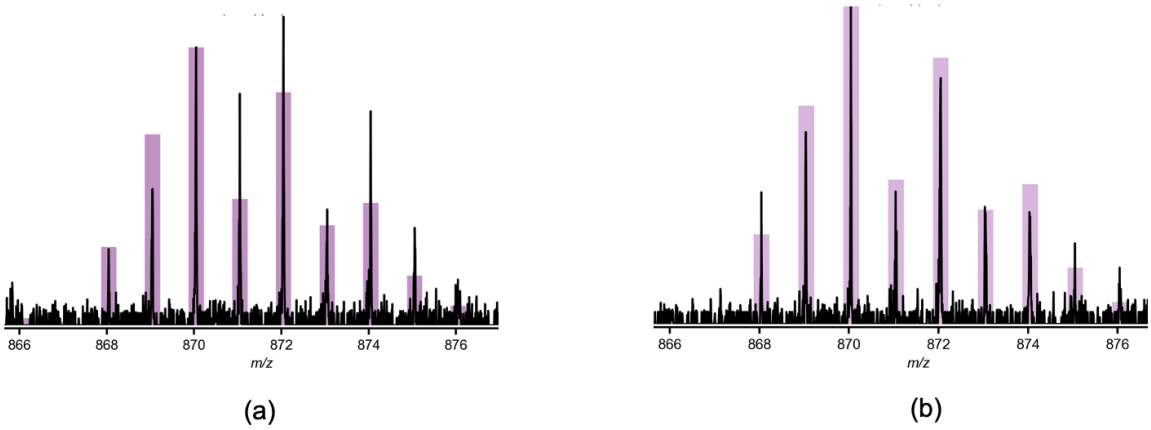

Figure A12. The predicted isotope pattern (bars) overlaid on the experimental mass spectrum (lines) for $[Pd(PPh_3)(\mathbf{1})(C_5H_7NO_3S)]^-$ after the addition of *N*-acetylcysteine at 7 mins (a) and 8.5 mins (b).

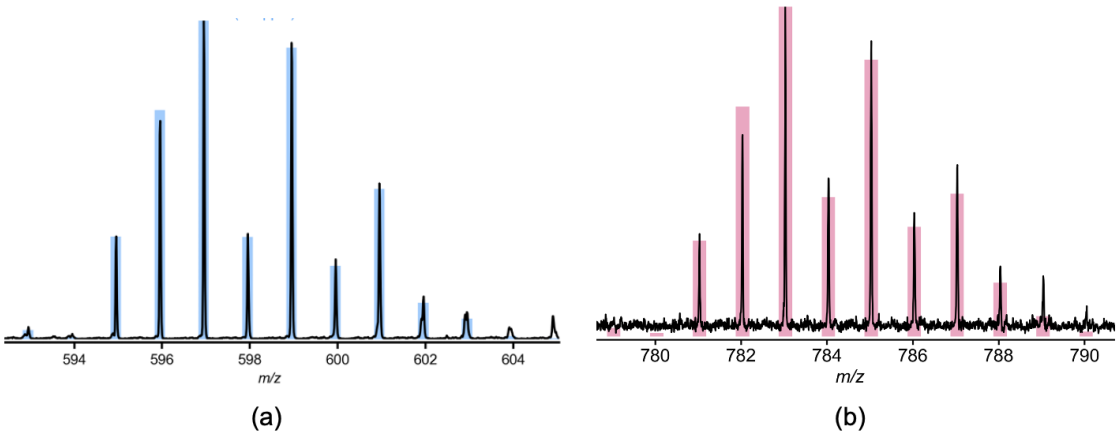

Figure A13. The predicted isotope pattern (bars) overlaid on the experimental mass spectrum (lines) for $[Pd(\mathbf{1})(\mathbf{3}\text{-}H)_2]^-$ (a) and $[Pd(PPh_3)(\mathbf{1})(\mathbf{3}\text{-}2H)]^-$ (b).

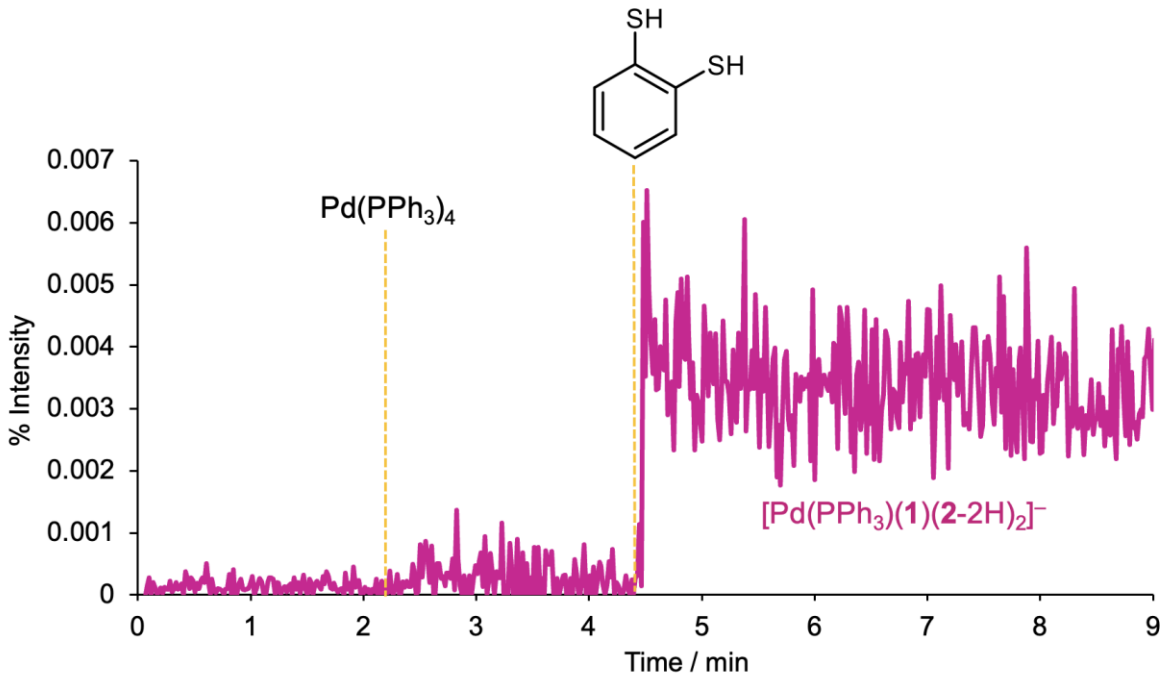

Figure A14. PSI-ESI-MS reaction monitoring in negative ion mode showing the poisoned product: $[Pd(PPh_3)(\mathbf{1})(\mathbf{2}\text{-}2H)_2]^-$ after adding 1,2-benzenedithiol.